

CLASSICAL AND QUANTUM MECHANICS OF A CHAOTIC HAMILTONIAN SYSTEM: THE WEDGE BILLIARD

THÈSE N° 1352 (1995)

PRÉSENTÉE AU DÉPARTEMENT DE PHYSIQUE

ÉCOLE POLYTECHNIQUE FÉDÉRALE DE LAUSANNE

POUR L'OBTENTION DU GRADE DE DOCTEUR ÈS SCIENCES

PAR

CHRISTOPHE ROUVINEZ

Physicien diplômé EPF
originaire de Grimentz et Vissoie (VS)

acceptée sur proposition du jury:

Prof. Ph. Choquard, rapporteur
Dr M. Cibils, corapporteur
Prof. R. Livi, corapporteur
Prof. U. Smilansky, corapporteur

Lausanne, EPFL
1995

Résumé

Nous étudions les relations entre un système quantique et son analogue classique à l'aide du billiard gravitationnel dans un dièdre. Ce modèle présente un large éventail de comportements allant de l'intégrabilité au chaos dur. Nous donnons l'expression des variables angles-actions pour le flot et pour l'application du bord dans le bord lorsque la dynamique est intégrable. Une attention particulière est portée sur les orbites spéciales, telles celles qui rebondissent dans le coin, ou celles qui glissent le long du bord. Nous analysons leur influence sur le comportement statistique classique. Au niveau quantique, nous étendons le formalisme de quantification par la théorie des collisions à des systèmes Hamiltoniens plus généraux en 2 dimensions, et l'illustrons sur le dièdre. Les énergies propres sont alors données par les zéros d'une équation séculaire. Les fonctions d'onde correspondantes peuvent aussi être construites. Nous vérifions analytiquement que cette condition de quantification est exacte pour les cas intégrables. La méthode s'est révélée fructueuse au niveau numérique et a permis la détermination de quelques milliers de niveaux propres. A l'aide de ces données, nous avons pu tester la formule de trace de Gutzwiller ainsi que d'autres relations semiclassiques mettant en liaison la matrice de diffusion et les orbites périodiques du système. Nous présentons encore une analyse statistique détaillée de plusieurs distributions de vitesses et de courbures.

Mots clefs: Billards, systèmes dynamiques, chaos, mécanique classique et quantique, théories semiclassiques et applications

Abstract

We examine the correspondence between a quantum system and its classical analogue. We consider the wedge billiard which shows a wide variety of behaviors ranging from integrable to strongly chaotic. Angle-action coordinates are provided for the flow and for the bouncing map when the dynamics is integrable. Special sets of orbits, such as orbits bouncing in the corner and orbits sliding along the boundary are investigated. Their influence on the classical statistical properties is also discussed. At the quantum level, we extend the scattering approach to quantize general Hamiltonian systems in 2 dimensions and demonstrate it for the wedge. The resulting energy levels are given by the zeros of a secular equation. The corresponding wave functions may also be constructed. We verify analytically that this quantization condition is exact in the case of the integrable wedges. This method has been applied successfully to compute numerically a few thousand levels. Using this data, we can check the Gutzwiller trace formula and other semiclassical relations involving the scattering matrix and periodic orbits. Finally we perform a detailed statistical analysis of several velocity and curvature distributions.

Keywords: Billiards, dynamical systems, chaos, classical and quantum mechanics, semiclassical theories and applications

Acknowledgments

I am grateful to my advisor, Prof. Ph. Choquard, for giving to me the opportunity of working on this fascinating subject, and for encouraging me all along the writing of the thesis.

The second part of this work is the result of a friendly collaboration with Prof. U. Smilansky, and I am particularly indebted to him for valuable ideas and discussions on the quantum approach.

I am also grateful to Dr. O. Maggioni who provided fruitful help in the understanding of the theory of dynamical systems.

I would like to thank Dr. M. Cibils for careful reading of the manuscript.

Many thanks to Dr. A. Testa for useful advice concerning computer implementation.

I wish to thank Prof. K. Kern, Prof. R. Livi, Prof. U. Smilansky and Dr. M. Cibils for accepting to be members of the examination board.

I am obliged to the Institut de Physique Théorique for its welcome and for the cheerful atmosphere during my stay.

Last but not least, it is a pleasure to thank all my friends, relatives and fellow colleagues for extra-scientific activities which also contributed to the successful completion of the thesis.

Contents

Introduction	3
1 Classical Mechanics	5
1.1 Preliminary	5
1.2 Billiard System and Scattering System	6
1.3 Origin of the Model	8
1.4 Integrable Cases	12
1.4.1 One Dimensional Bouncer	13
1.4.2 Wedge Billiards	14
1.4.3 Open Wedges	16
1.5 Bouncing Maps	17
1.6 Invariant Measures and Conservative Maps	22
1.7 Special Orbits	24
2 Numerical Results on Classical Mechanics	27
2.1 Preliminary	27
2.2 Lyapunov Exponents	28
2.3 Correlation Functions	30
2.4 Role of Singularities	33
3 Quantum Mechanics	37
3.1 Preliminary	37
3.2 Quantum Billiard System	38
3.2.1 One Dimensional Quantum Bouncer	38
3.2.2 EBK Quantization	39
3.2.3 Integrable Wedges	40
3.3 Scattering Approach to Quantization	41
3.4 Exact Quantization of the Wedge Billiard	45
3.4.1 General Wedge	45
3.4.2 Integrable Symmetric Wedge	47
3.4.3 Integrable Square Wedge	48

3.5	Semiclassical Propagators	49
3.6	Semiclassical Analysis	53
4	Numerical Results on Quantum Mechanics	59
4.1	Preliminary	59
4.2	Checks of the Quantum Formalism	60
4.3	Checks of the Semiclassical Analysis	65
4.4	Semiclassical Evolution of a Wave Packet	76
4.5	Statistical Analysis	79
4.5.1	Statistics of Eigenenergies	80
4.5.2	Statistics of Eigenphases	85
4.5.3	Statistics of Level Velocities and Curvatures	88
4.5.4	Statistics of Phase Velocities and Curvatures	91
4.5.5	Statistics of Eigenvalues of the time delay matrix	93
	Discussion	95
	Appendices	99
A.1	Local Properties of the Bouncing Map near Corners	99
A.1.1	Continuity of P^σ for Euclidean Billiards	99
A.1.2	Differentiability of P^σ for Euclidean Billiards	105
A.1.3	Generalization to the Wedge Billiard	108
A.2	Symmetries of the S Matrix	110
A.2.1	Time Reversal Invariance	110
A.2.2	Conservation of flux	112
A.2.3	Summary and Reformulation	113
	References	115

Introduction

In this work we are concerned with the study of the correspondence between a quantum system and its classical analogue. The Einstein-Brillouin-Keller quantization scheme – also known as the torus quantization method – may be used to connect classical and quantum systems when the classical dynamics is integrable. The problem of quantizing non-integrable systems has already been mentioned by Einstein [Ei] as early as 1917, and the relation to classical concepts for such models is still far from obvious today. As quantum mechanics is the most fundamental theory, the limit $\hbar \rightarrow 0$ should reproduce the features of classical mechanics. However, this limit is singular for most physical quantities. Hence the semiclassical region with \hbar small but non-zero is the most attractive domain to develop the quantum mechanics of classically chaotic systems.

Time independent Hamiltonian systems of the billiard type are used to model the ballistic regime of two dimensional electronic gas, in order to characterize the quantum transport properties of mesoscopic semiconductor heterojunctions [BH]. Moreover, this class of models provides an easier framework for the search of the quantum mechanical fingerprints of chaos. First, two dimensional classical billiards possess the minimum number of freedoms allowing chaotic behavior. They yield a wide variety of dynamical behaviors ranging from integrable to strongly chaotic. The classical dynamics can be reduced to a lower dimensional map from the boundary into itself. Since the potential is homogeneous, the classical dynamics of the system scales trivially with energy. As a consequence, the dynamics is kept unaltered when going to the semiclassical limit. Second, the quantum mechanics of billiard systems can also be mainly reduced to a boundary problem. We shall make use of this property to investigate the connections between classical and quantum systems, generalizing the scattering approach to quantization derived by Doron and Smilansky [DoS].

We shall focus on the wedge billiard which consists of two hard walls meeting at the origin. The motion is bounded by a linear gravitational field so that trajectories are

parabola¹. The introduction of a potential is a first step toward more general conservative systems. Moreover, the wedge billiard has a few important advantages. It is known that the classical dynamics is integrable, mixed or hyperbolic depending on the choice of the angle between the hard walls. In the chaotic regime, the dynamics can be represented symbolically in terms of a binary code. This is of great help in identifying periodic orbits. The quantization of the wedge billiard was previously discussed by Wittek *et al.* [RSW, Wi] and later by Szeredi *et al.* [SG1, SG2, SG3, SLG]. This will enable us to compare the more familiar approach which was previously followed, with the new approach we pursue here. Last but not least, the Hamiltonian is sufficiently simple so that a large quantum data base can be calculated. Notice that in the context of semiconductors, the linear potential that we introduce here finds an easy interpretation as an electric field.

The origin of the model as a one dimensional system of three ordered and charged particles is shown in the first chapter, where the classical system is described. We also provide an extensive investigation of the integrable cases, and discuss the peculiarities of the classical dynamics. The second chapter is devoted to the numerical analysis of the classical model. We compare the statistical properties of the systems with discrete and continuous time and examine the influence of the singularity at the vertex when the dynamics is mixed. The quantum mechanics of the wedge is investigated in chapter 3, which starts with the solutions of the integrable cases. We then describe the exact quantization procedure for a general Hamiltonian with bounding potential, apply it to the wedge, and check the accuracy on the integrable solutions. We derive a semiclassical approximation to the energy density, and test it on the integrable wedges. Chapter 4 contains the numerical quantum results. First we evaluate the accuracy of the scattering method and the applicability of the semiclassical approximation. Once this is done, we perform a detailed statistical analysis of several spectral velocity and curvature distributions. Finally, we summarize our results and discuss the open problems in the last chapter.

¹The integrability of the billiard in a linear field with a parabolic boundary has been first proven by Chaplygin [Cha] and rediscovered later on by Korsch *et al.* [KL].

1. Classical Mechanics

1.1 Preliminary

We start this chapter with a description of the wedge billiard. We remind the reader of the various behaviors of the system as a function of the angle, which is the only parameter of the system. We show that a scattering process may be defined when one side of the wedge is horizontal.

In the original study of Wright and Miller [WM], the wedge billiard originates from a mechanical system describing the collisions of planar galaxies. Here we show that the billiard is isomorphic to a one dimensional system of ordered particles with Coulombian and Newtonian interactions. The introduction of masses and charges allows the isomorphism between both systems to be valid for a wider range of the parameters.

In the following section we investigate the integrable wedges. As one dimensional Hamiltonian systems are integrable, we start our analysis with a one dimensional particle in a linear field bouncing against a hard wall. We compute explicitly angle-action variables that are useful for the discussion of the two dimensional cases. We also analyze the structure of the invariant manifolds of all different integrable wedges.

Instead of studying the flow of the system on the three dimensional energy shell, one usually considers cross sections with a lower dimensional submanifold. The evolution is then given in terms of a discrete map. We give an adequate set of coordinates which reflects the simplicity of the dynamics when the wedge is integrable. Special attention is drawn on the role played by the singularity in this case. In the subsequent section we explain how to determine invariant ergodic measures. This computation provides an easy proof that the map in the above coordinates is area preserving.

The chapter ends with a description the sets of orbits characteristic of this model. The singular trajectories bouncing exactly in the corner are important because they may be at the origin of semiclassical contributions, as we will see in the last chapter.

We show that a definition by continuity makes sense for a given set of wedge angles (the proof is given in the first appendix). The other set of special orbits consists in the orbits sliding along the inclined side with velocity almost tangent to the boundary which will be shown to exert some influence on statistical measures.

1.2 Billiard System and Scattering System

One calls *billiard* a dynamical system corresponding to the motion of a pointlike particle in a compact Riemannian manifold with a piecewise smooth boundary. The particle is reflecting from the boundary according to the law of elastic reflection and the motion between reflections corresponds to the geodesic flow.

The *wedge billiard* consists of two walls (infinite potential barrier) along the lines $y = -\cot(\beta_L)x$ and $y = \cot(\beta_R)x$ (see Fig. 1.1). The motion is bounded by a gravitational potential and the Hamiltonian of the system reads (using units where $m = g = 1$)

$$H = \frac{p_x^2}{2} + \frac{p_y^2}{2} + y. \quad (1.1)$$

As the potential is homogeneous [LL1] the trajectories at energy E' are in correspondence with the ones at energy E by rescaling coordinates and time

$$\begin{aligned} x' &= \alpha_1 x & t' &= \alpha_2 t. \\ y' &= \alpha_1 y \end{aligned} \quad (1.2)$$

Requiring both the kinetic energy and potential energy to be scaled by the same factor, we get $\alpha_2 = \sqrt{\alpha_1}$ and

$$\begin{aligned} x' &= \frac{E'}{E} x & p'_x &= \sqrt{\frac{E'}{E}} p_x & t' &= \sqrt{\frac{E'}{E}} t. \\ y' &= \frac{E'}{E} y & p'_y &= \sqrt{\frac{E'}{E}} p_y \end{aligned} \quad (1.3)$$

Hence phase spaces at different energies are in one to one correspondence. Once quantities of the system (such as action or stability of periodic orbits ...) are known at a reference energy E (say $E=1$), the corresponding quantities of the system at energy E' are easily determined using the above rescaling. This property common to billiards makes them particularly convenient for testing semiclassical conjectures which necessitate the knowledge of the periodic orbits at all energies.

Thus, the only parameters determining the behavior of the system are the angles β_L and β_R of the sides of the wedge. We require that $\beta_{R,L} \leq \pi/2$, so that the velocity of the particle remains bounded.

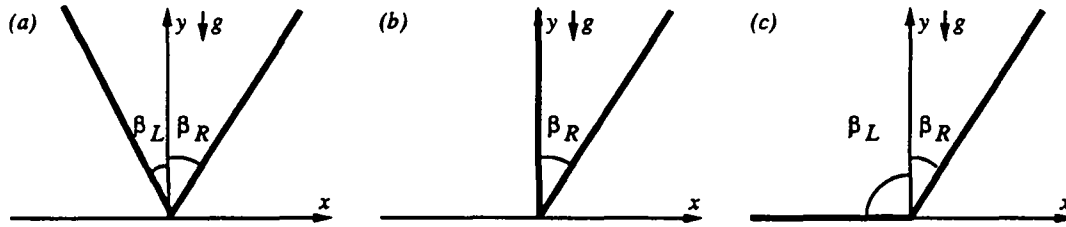


Fig. 1.1. (a) Wedge, (b) half wedge ($\beta_L = 0$) and (c) open wedge ($\beta_L = \pi/2$).

Most of the time we will restrict our analysis to the *half wedge* (wedge billiard with $\beta_L = 0$), since it already presents a wide range of behaviors:

- For $\beta_R > \pi/4$, the system is ergodic and all trajectories are unstable. Wojtkowski [Wo] has shown analytically that the system possesses an almost everywhere non-vanishing Lyapunov exponent. Such a system is said to be strongly chaotic.
- At $\beta_R = \pi/4$ all trajectories are regular and the system is integrable.
- When $\beta_R < \pi/4$, the phase space is composed of islands of regular motion surrounded by stochastic components and the system is said to exhibit weak chaos.

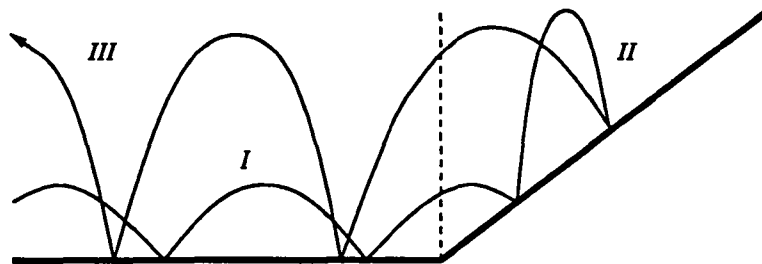


Fig. 1.2. Three stages of scattering in open wedge billiards.

The wedges with $\beta_L = \pi/2$ (or $\beta_R = \pi/2$) will be called *open wedges*. For symmetry reasons we will consider only the case $\beta_L = \pi/2$. Since the phase space is not bounded, particles may escape to infinity. One can also characterize the properties of such systems looking at the associated scattering process. Scattering on an open wedge decomposes into the three usual stages (see Fig. 1.2):

- I* A particle coming from minus infinity with positive horizontal velocity moves to the right while bouncing against the horizontal side of the boundary. The Hamiltonian (1.1) with the horizontal side on the domain on the left of the origin yields integrable motion (the system is separable) and plays the role of the free Hamiltonian.

II Then the particle scatters against the inclined side, where it may bounce not only once but several times. The Hamiltonian (1.1) with the inclined side on the domain on the right of the origin is the interaction Hamiltonian.

III Finally the particle leaves the interaction region $x \geq 0$ and evolves backwards with constant negative horizontal velocity in the asymptotic domain $x \leq 0$.

Looking at the geometry of this system it is clear that no orbits may remain trapped in the interaction region $x > 0$. Since the unstable trapped orbits are the source of homoclinic chaos in scattering, it follows that the open wedges do not display chaotic scattering¹. The Poincaré Scattering Map (PSM) which maps ingoing states onto outgoing states is not smooth because of the singularity in the corner. Nevertheless, such scattering processes without trapped orbits are called regular [BDJS]. The above decomposition of the process simplifies the analysis of the dynamics. It should be noted that all three stages yield integrable motion when considered separately in the appropriate coordinates. It is the passage from one system to the other which may induce instability in the dynamics. The stability of the orbits depends on the bouncing map from the vertical side back into it during the second stage and hence may be deduced from the above analysis of the half wedge:

- For $\beta_R > \pi/4$ the dynamics is hyperbolic and hence the PSM is also hyperbolic.
- At $\beta_R = \pi/4$ there is an additional constant of motion in the interaction region. However this constant is not preserved under the dynamics of the free Hamiltonian so that the system is not integrable. Because of its regularity this case will be discussed in more details in the next section.
- When $\beta_R < \pi/4$ the underlying dynamics may be either stable or unstable.

This approach will be of major interest when considering the quantum mechanics of the wedge.

1.3 Origin of the Model

In this section we show that the wedge billiard is isomorphic to a one dimensional system of three ordered particles with Coulombian and Newtonian interactions, which Hamiltonian reads

$$H = \sum_{k=1}^3 \frac{p_k^2}{2m_k} + \frac{1}{2} \sum_{i,j=1}^3 (m_i m_j G - e_i e_j) |q_i - q_j|. \quad (1.4)$$

¹Connecting a wave guide to the inclined side of a half wedge, one obtains a scattering system which may present homoclinic chaos [Du].

The particles may have different masses m_k and charges e_k . To reduce the number of parameters, we require charge neutrality of the system, i.e. $\sum_{k=1}^3 e_k = 0$.

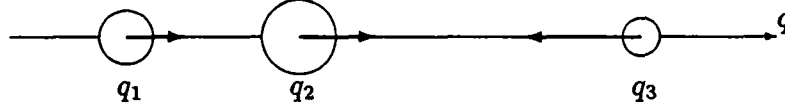


Fig. 1.3. Three particles on a line

First we perform a transformation which renders the kinetic energy isotropic. Setting $M = \sum_{k=1}^3 m_k$ and $\mu_k = m_k/M$, we trivially get $\sum_{k=1}^3 \mu_k = 1$. We define the new coordinates $\tilde{q}_k = \sqrt{\mu_k} q_k$ and velocities $\dot{\tilde{q}}_k = \sqrt{\mu_k} \dot{q}_k$. The kinetic energy then reads

$$T = \sum_{k=1}^3 \frac{m_k \dot{q}_k^2}{2} = \sum_{k=1}^3 \frac{M \dot{\tilde{q}}_k^2}{2}. \quad (1.5)$$

One can write this transformation $\dot{\tilde{\mathbf{q}}} = D\dot{\mathbf{q}}$, where the matrix D is diagonal

$$D = \begin{pmatrix} \sqrt{\mu_1} & 0 & 0 \\ 0 & \sqrt{\mu_2} & 0 \\ 0 & 0 & \sqrt{\mu_3} \end{pmatrix}. \quad (1.6)$$

Note that this transformation on coordinates and velocities is equivalent to the canonical transformation $\tilde{\mathbf{q}} = D\mathbf{q}$ and $\tilde{\mathbf{p}} = D^{-1}\mathbf{p}$ on the conjugate variables (\mathbf{p}, \mathbf{q}) .

Next we perform an orthogonal transformation $\dot{\tilde{\mathbf{q}}} = O\dot{\tilde{\mathbf{q}}}$, in order to separate the degree of freedom corresponding to the center of mass

$$\dot{\tilde{q}}_3 = \sum_{k=1}^3 m_k \dot{q}_k = M \sum_{k=1}^3 \sqrt{\mu_k} \dot{\tilde{q}}_k = 0 \quad (1.7)$$

which we set equal zero. This does not entirely determine the transformation. A convenient choice for O is

$$O = \begin{pmatrix} -\sqrt{\frac{\mu_1 \mu_2}{\mu_1 + \mu_3}} & \sqrt{\mu_1 + \mu_3} & -\sqrt{\frac{\mu_2 \mu_3}{\mu_1 + \mu_3}} \\ -\sqrt{\frac{\mu_3}{\mu_1 + \mu_3}} & 0 & \sqrt{\frac{\mu_1}{\mu_1 + \mu_3}} \\ \sqrt{\mu_1} & \sqrt{\mu_2} & \sqrt{\mu_3} \end{pmatrix}, \quad (1.8)$$

where the first two lines were chosen so that the matrix is orthogonal. Here again, the transformation is equivalent to the rotation of axes $\bar{\mathbf{q}} = O\tilde{\mathbf{q}}$ and $\bar{\mathbf{p}} = O\tilde{\mathbf{p}}$, which is also a canonical transformation.

As the particles are ordered, one can remove the absolute values in the expression of the potential. Choosing $q_1 \leq q_2 \leq q_3$, we get

$$V = \sum_{k=1}^3 A_k q_k \quad (1.9)$$

with

$$\begin{aligned} A_1 &= e_1(e_2 + e_3) - M^2 G \mu_1(\mu_2 + \mu_3) \\ A_2 &= e_2(e_3 - e_1) + M^2 G \mu_2(\mu_1 - \mu_3) \\ A_3 &= -e_3(e_1 + e_2) + M^2 G \mu_3(\mu_1 + \mu_2). \end{aligned} \quad (1.10)$$

Inverting the transformations, we obtain $V = \sum_{k=1}^3 B_k \bar{q}_k$ with $B = A \cdot O^{-1} \cdot D^{-1}$. As we set $\bar{q}_3 = 0$, only B_1 and B_2 are worth being evaluated and give

$$\begin{aligned} B_1 &= \left[e_2(e_3 - e_1) + M^2 G \mu_2(\mu_1 - \mu_3) \right] \left(\sqrt{\frac{\mu_2}{\mu_1 + \mu_3}} + \sqrt{\frac{\mu_1 + \mu_3}{\mu_2}} \right) \\ B_2 &= \frac{\mu_3 e_1^2 + \mu_1 e_3^2 + M^2 G \mu_1 \mu_3 (1 + \mu_2)}{\sqrt{\mu_1 \mu_3 (\mu_1 + \mu_3)}}. \end{aligned} \quad (1.11)$$

We want the potential to be directed along one of the axes. As $B_2 > 0$, we set $B_1 = 0$ and obtain the following condition on the charges

$$e_1^2 - e_3^2 + M^2 G \mu_2(\mu_1 - \mu_3) = 0 \quad (1.12)$$

after use of the charge neutrality of the system. One could now rescale coordinates and time, setting

$$x = \frac{mg}{B_2} \bar{q}_1, \quad y = \frac{mg}{B_2} \bar{q}_2 \quad \text{and} \quad t' = \frac{m^2 g}{M B_2} t \quad (1.13)$$

to obtain the new Hamiltonian

$$H' = \frac{p_x^2}{2m} + \frac{p_y^2}{2m} + mgy \quad (1.14)$$

of a two dimensional quasi-particle of mass m in a gravitational field g . Thus, the motion of the true particles reduces to the fall of the quasi-particle in a gravitational field.

We required that the original particles had to remain ordered. The resulting relations in q space may be translated in xy space. They will induce restrictions on the two dimensional domain of the quasi-particle. In \bar{q} space, order of the particles reads

$$\begin{aligned} q_2 - q_1 &= \sqrt{\frac{\mu_3}{\mu_1(\mu_1 + \mu_3)}} \bar{q}_2 + \left(\sqrt{\frac{\mu_1 + \mu_3}{\mu_2}} + \sqrt{\frac{\mu_2}{\mu_1 + \mu_3}} \right) \bar{q}_1 \geq 0 \\ q_3 - q_2 &= \sqrt{\frac{\mu_1}{\mu_3(\mu_1 + \mu_3)}} \bar{q}_2 - \left(\sqrt{\frac{\mu_1 + \mu_3}{\mu_2}} + \sqrt{\frac{\mu_2}{\mu_1 + \mu_3}} \right) \bar{q}_1 \geq 0, \end{aligned} \quad (1.15)$$

since $\bar{q}_3 = 0$. Thus, collisions of particles 1-2 and 2-3 map onto the straight lines $\bar{q}_2 = -\sqrt{\frac{\mu_1}{\mu_2\mu_3}}\bar{q}_1$ and $\bar{q}_2 = \sqrt{\frac{\mu_3}{\mu_1\mu_2}}\bar{q}_1$. As the rescaling (1.13) is homogeneous in coordinates, we obtain straight lines with the same slopes in xy space. They define a wedge which is the domain of the quasi-particle (see Fig. 1.1). The corresponding angles β_R and β_L verify

$$\tan \beta_R = \sqrt{\frac{\mu_1\mu_2}{\mu_3}} \quad \text{and} \quad \tan \beta_L = \sqrt{\frac{\mu_2\mu_3}{\mu_1}}. \quad (1.16)$$

These angles only depend on the value of the masses and hence must be positive. The wedge is symmetrical for $\mu_1 = \mu_3$. As

$$\tan(\beta_R + \beta_L) = \sqrt{\frac{\mu_2}{\mu_1\mu_3}} \quad (1.17)$$

the total angle of the wedge $\beta = \beta_R + \beta_L$ must be smaller than $\pi/2$ for the isomorphism to be valid. As we have seen above, the dynamics of the system is quite different for $\beta \gtrsim \pi/2$. The breaking of this isomorphism may be seen as an indication of the fundamental change in the nature of the system when β reaches $\pi/2$. The shape of the domain does not seem to depend on the charges of the particles, but the Coulombian interaction was necessary to set the direction of the potential parallel to the \bar{q}_2 axis.

So we have verified that the motion of the original particles is isomorphic to the fall of a quasi-particle in a wedge. The last step is to check that a collision between two particles is represented by an elastic reflection of the quasi-particle with one side of the wedge.

Elastic collision of two particles in one dimension is determined by conservation of momentum and energy. For the sake of simplicity, we will consider a collision between particles 1 and 2. Calling \dot{q}_\pm the velocities just before and after the collision, one can describe the change of the velocities by a linear transformation $\dot{q}_+ = C \dot{q}_-$, where

$$C = \begin{pmatrix} \frac{m_1 - m_2}{m_1 + m_2} & \frac{2m_2}{m_1 + m_2} & 0 \\ \frac{2m_1}{m_1 + m_2} & -\frac{m_1 - m_2}{m_1 + m_2} & 0 \\ 0 & 0 & 1 \end{pmatrix}. \quad (1.18)$$

Denoting $\bar{\dot{q}}_+ = \bar{C} \bar{\dot{q}}_-$ the corresponding law of reflection in \bar{q} space and using the transformation rule $\bar{\dot{q}} = O D \dot{q}$, we obtain

$$\bar{C} = O \cdot D \cdot C \cdot D^{-1} \cdot O^{-1} = \begin{pmatrix} \frac{\mu_2\mu_3 - \mu_1}{\mu_2\mu_3 + \mu_1} & \frac{-2\sqrt{\mu_1\mu_2\mu_3}}{\mu_2\mu_3 + \mu_1} & \dots \\ \frac{-2\sqrt{\mu_1\mu_2\mu_3}}{\mu_2\mu_3 + \mu_1} & \frac{\mu_2\mu_3 - \mu_1}{\mu_2\mu_3 + \mu_1} & \dots \\ \dots & \dots & \dots \end{pmatrix} \quad (1.19)$$

where the elements represented with “...” need not be evaluated for $\dot{\bar{q}}_3 = 0$.

On another hand, an elastic reflection against one side making an angle α with the \bar{q}_1 axis may be decomposed as the product of a rotation of angle $-\alpha$, an inversion of the coordinate \bar{q}_2 , and a backwards rotation of angle α . For $\tan \alpha = \sqrt{\frac{\mu_2\mu_3}{\mu_1}}$, the composition of these three operations gives

$$R(\alpha) \cdot I \cdot R(-\alpha) = \begin{pmatrix} \frac{\mu_2\mu_3 - \mu_1}{\mu_2\mu_3 + \mu_1} & \frac{-2\sqrt{\mu_1\mu_2\mu_3}}{\mu_2\mu_3 + \mu_1} \\ \frac{-2\sqrt{\mu_1\mu_2\mu_3}}{\mu_2\mu_3 + \mu_1} & \frac{\mu_2\mu_3 - \mu_1}{\mu_2\mu_3 + \mu_1} \end{pmatrix} \quad (1.20)$$

which corresponds exactly to the submatrix of \bar{C} involving \bar{q}_1 and \bar{q}_2 . Thus, the elastic collision of the particles 1–2 leads to the elastic reflection of the quasi-particle against the left side of the wedge. Similarly, the collision of particles 2–3 translates into a elastic reflection against the right side of the wedge.

An elastic reflection with both sides of the wedge at the same time (i.e. at the vertex) is not defined, since the normal to the boundary is not unique. Such a situation is interpreted as the triple collision of the true particles which is also undetermined in \mathbf{q} space, for the number of equation is not sufficient to determine the issue. So the singularities of both models are in one to one correspondence ².

From now on we will forget about this physical origin and focus on the wedge billiard.

1.4 Integrable Cases

We investigate the wedge billiards for which the dynamics is integrable. We give constants of motion in involution and with linear independent gradients which can be used for quadrature. We also determine the topology of the invariant manifolds given by the level sets of the constants of motion. Because of the collisions against the walls, the flow is discontinuous in phase space. Reflection at a boundary corresponds to jumping between two sheets of the same level set. Hence some boundaries have to be identified to obtain a smooth manifold where the flow may be given in a simple form.

²It can be shown that the wedge billiard is also isomorphic to a one dimensional system of two ordered balls embedded in an external gravitational field, where the motion of the balls is bounded by a hard wall [Wo]. Such a system presents the same kind of singularities when both balls collide with the wall at the same time.

1.4.1 One Dimensional Bouncer

First we consider a one dimensional particle confined between a hard wall at $y = 0$ and a gravitational potential. Setting $m = g = 1$ the Hamiltonian of this system reads

$$H = \frac{p_y^2}{2} + y \quad (1.21)$$

and the energy E_y is a constant of motion. Thus it may be integrated by quadrature.

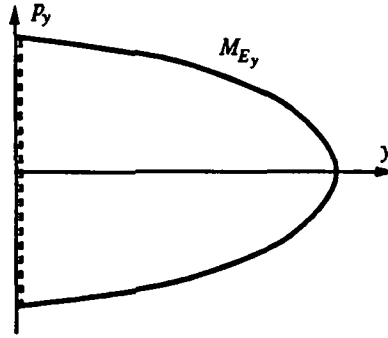


Fig. 1.4. Manifold of constant energy M_{E_y} .

Identifying the points $(0, \pm\sqrt{2E_y})$, the manifold of constant energy M_{E_y} is topologically equivalent to the circle \mathbf{S}^1 with one irreducible circuit γ . Following Arnold [Ar], we can construct explicitly action-angle variables (I, φ) for this system. The action I is defined as

$$I = \frac{1}{2\pi} \oint_{\gamma} p_y(E, y) dy = \frac{2\sqrt{2}}{3\pi} E_y^{3/2} \quad (1.22)$$

and the period reads

$$T = \frac{\partial I}{\partial E_y} = \frac{1}{\pi} \sqrt{2E_y}. \quad (1.23)$$

We may invert equation (1.22) to get the Hamiltonian as a function of the action

$$H = \left(\frac{3\pi}{2\sqrt{2}} I \right)^{2/3}. \quad (1.24)$$

From the generating function $W(I, y) = \int_{y_0}^y p_y(I, y') dy'$, which is the generator of the canonical transformation from (p_y, y) to (I, φ) , we obtain the angle variable as

$$\begin{aligned} \varphi &= \frac{\partial W(I, y)}{\partial I} \\ &= \pi \left[\left(2 - \sqrt{1 - 2y(3I)^{-2/3}} \right) \theta(p_y) + \sqrt{1 - 2y(3I)^{-2/3}} \theta(-p_y) \right] \end{aligned} \quad (1.25)$$

where θ is the unit step function. The time evolution of conjugate variables is given by Hamilton's equations of motion, so that

$$\begin{aligned}\frac{d}{dt}I &= -\frac{\partial H}{\partial \varphi} = 0 \\ \frac{d}{dt}\varphi &= \frac{\partial H}{\partial I} = \omega = \text{const.}\end{aligned}\quad (1.26)$$

The phase flow takes the especially simple form

$$\begin{aligned}I(t) &= I \\ \varphi(t) &= \varphi_0 + \omega t\end{aligned}\quad (1.27)$$

where the evolution is now completely smooth when the particle collides with the boundary.

1.4.2 Wedge Billiards

From the one dimensional integrable case, we deduce the solutions of the integrable wedges. To take advantage of the geometry of the system, it may be useful to introduce the rotated coordinate system $O\tilde{x}\tilde{y}$, such that the x axis is parallel to the right side of the wedge.

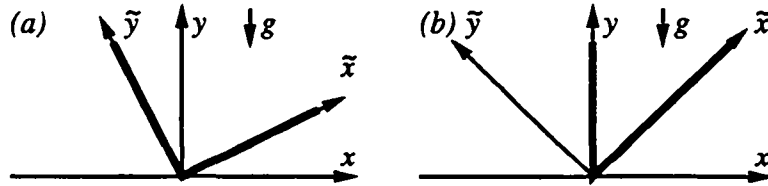


Fig. 1.5. Integrable wedges : (a) square wedge (b) half symmetric square wedge

a) Square wedge ($\beta_R + \beta_L = \pi/2, \beta_{R,L} \neq 0$): The system is separable in the rotated coordinates $O\tilde{x}\tilde{y}$, so that $E_{\tilde{x}}$ and $E_{\tilde{y}}$ are constants of motion appropriate for quadrature. In both directions, the flow reduces to a rotation on the circle. After identification of $(0, \pm\sqrt{2E_{\tilde{x}}}, y, p_y)$ and $(x, p_x, 0, \pm\sqrt{2E_{\tilde{y}}})$, $M_{\{E_{\tilde{x}}, E_{\tilde{y}}\}}$ has the topology of a torus $\mathbb{S}^1 \otimes \mathbb{S}^1 = \mathbb{T}^2$. Introducing the above action-angle variables for both directions, we obtain

$$H = \left(\frac{3\pi}{2\sqrt{2}}I_{\tilde{x}}\right)^{2/3} + \left(\frac{3\pi}{2\sqrt{2}}I_{\tilde{y}}\right)^{2/3}. \quad (1.28)$$

Because of the separability the quasiperiodic trajectories fill rectangles with sides parallel to the sides of the wedge in configuration space.

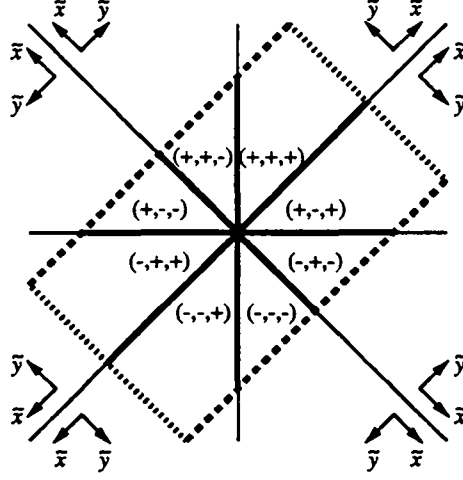


Fig. 1.6. Projection of the unfolded manifold $M_{\{E,D^2\}}$.

b) **Half symmetric square wedge** ($\beta_R = \pi/4, \beta_L = 0$): The system is non-separable, since bouncing against the vertical side exchanges the values of the energies $E_{\bar{x}}$ and $E_{\bar{y}}$. When $E_{\bar{x}} \neq E_{\bar{y}}$, the sum $E = E_{\bar{x}} + E_{\bar{y}}$ and the square of the difference $D = E_{\bar{x}} - E_{\bar{y}}$ are two constants of motion in involution and functionally independent (the case $E_{\bar{x}} = E_{\bar{y}}$ will be treated separately). Determination of the irreducible circuits is not obvious. We consider the projection of $M_{\{E,D^2\}}$ on configuration space. This projection consists of eight sheets labeled by the signs of the quantities $p_{\bar{x}}$, $p_{\bar{y}}$ and D . This latter accounts for the exchange of the energies $E_{\bar{x}}$ and $E_{\bar{y}}$. The eight sheets (\pm, \pm, \pm) may be sewn together to form a rectangle (see Fig. 1.6) with edges and vertices identified (dashed and dotted lines). Thus $M_{\{E,D^2\}}$ has the same topology as the torus \mathbb{T}^2 [RB]. The irreducible cycles γ_{\pm} may be chosen parallel to the sides of the rectangle. This clearly shows that both path of integration for the action variables I_{\pm} are identical in configuration space. They yield the actions

$$I_{\pm} = \frac{2\sqrt{2}}{3\pi} \left(\frac{E \pm \sqrt{D^2}}{2} \right)^{3/2} \quad (1.29)$$

and the Hamiltonian in the smooth variables reads,

$$H = \left(\frac{3\pi}{2\sqrt{2}} I_+ \right)^{2/3} + \left(\frac{3\pi}{2\sqrt{2}} I_- \right)^{2/3} \quad (1.30)$$

where $I_- < I_+$, so that the volume of phase space is half the one of the square wedge with $\beta_R = \beta_L = \pi/4$.

When $E_{\bar{x}} = E_{\bar{y}}$, one considers D as constant of motion, since the symplectic gradient of D^2 vanishes. The level sets $M_{\{E,0\}}$ are composed of only four sheets of equal size, labeled by the signs of the momenta. After identification, the manifold has the same topology as the product of an interval I times the circle S^1 . The symplectic

gradient of E is parallel to the boundaries of the truncated cylinder $\mathbb{I} \otimes \mathbb{S}^1$, so that all trajectories are periodic orbits.

The origin of this peculiarity becomes obvious when considering the phase space of this system as half the one of the square wedge with $\beta_R = \beta_L = \pi/4$. To each torus $M_{\{E_{\tilde{x}}, E_{\tilde{y}}\}}$ of the latter system corresponds a symmetrical one $M_{\{E_{\tilde{y}}, E_{\tilde{x}}\}}$, except when $E_{\tilde{x}} = E_{\tilde{y}}$. In this case there is only one torus, which rotation number is 1 (both frequencies are the same). Thus, when we consider half this system, we obtain only one half of the periodic tori $E_{\tilde{x}} = E_{\tilde{y}}$ which give the above truncated cylinders.

1.4.3 Open Wedges

We briefly discuss the integrable open wedges, which level sets have a different topology since phase space is not bounded.

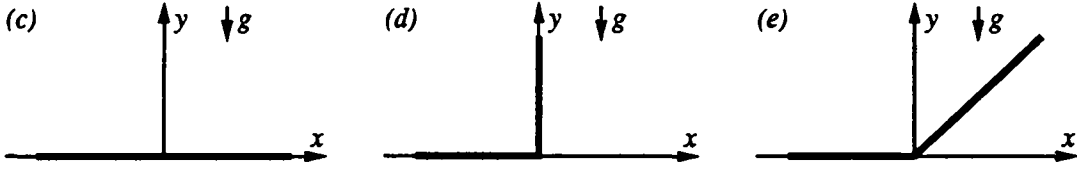


Fig. 1.7. Open wedges: (c) open flat wedge (d) open square wedge (e) open wedge with $\beta_R = \pi/4$

c) Open flat wedge ($\beta_R = \beta_L = \pi/2$): The system is separable in the coordinates Oxy . Thus the constants of motion p_x and E_y are suitable for quadrature. As motion is free in x direction, the coordinate $x \in \mathbb{R}$ varies uniformly with time. According to the previous subsection, motion in the y direction reduces to a rotation on the circle. We define $M_{\{p_x, E_y\}}$ as a level set of the constants of motion p_x and E_y . This is a two dimensional surface in the four dimensional phase space (x, p_x, y, p_y) . After the identification of the boundaries $(x, p_x, 0, \pm\sqrt{2E_y})$, $M_{\{p_x, E_y\}}$ is topologically equivalent to $\mathbb{R} \otimes \mathbb{S}^1$. Introducing the above action-angle variables for the y direction, the Hamiltonian in the smooth variables reads

$$H = \frac{p_x^2}{2} + \left(\frac{3\pi}{2\sqrt{2}} I_y \right)^{2/3}. \quad (1.31)$$

d) Open square wedge ($\beta_L = \pi/2, \beta_R = 0$): The system is also separable in the coordinates Oxy . As $|p_x|$ is constant, we consider the invariant manifold $M_{\{|p_x|, E_y\}}$, composed of the two semi-infinite stripes corresponding to $\pm p_x$. After the identification of the boundaries $(x, p_x, 0, \pm\sqrt{2E_y})$ [collisions with horizontal wall] and

$(0, \pm|p_x|, y(E_v, p_y), p_y)$ [collisions with vertical wall], $M_{\{p_x, E_y\}}$ is also topologically equivalent to $\mathbb{R} \otimes \mathbb{S}^1$. Performing the substitution

$$\bar{p}_x = |p_x| \quad \text{and} \quad \bar{x} = \begin{cases} -x & \text{when } p_x \leq 0 \\ x & \text{when } p_x \geq 0 \end{cases} \quad (1.32)$$

in the x direction, we obtain the smooth Hamiltonian

$$H = \frac{\bar{p}_x^2}{2} + \left(\frac{3\pi}{2\sqrt{2}} I_y \right)^{2/3}. \quad (1.33)$$

e) **Open wedge with $\beta_{\mathbf{R}} = \pi/4$:** Although not integrable, this system presents regularity properties close to integrability. We have seen that motion in the asymptotic domain $x \leq 0$ is integrable. Hence the corresponding part of phase space is foliated in invariant cylinders $\mathbb{R} \otimes \mathbb{S}^1$. For this value of the angle, motion in the interaction domain is also integrable, so that the rest of phase space is foliated in invariant tori $\mathbb{S}^1 \otimes \mathbb{S}^1$. Thus, a particle coming from minus infinity winds on a cylinder $M_{\{E, (E_x - E_y)^2\}}$. At $x = 0$, it enters the interaction domain, and passes from a cylinder to a section of a torus $M_{\{E, (E_x - E_y)^2\}}$ which belongs to the other foliation. Finally, it leaves the interaction domain at $x = 0$ and turns back to the previous foliation, but on another level set $M_{\{E, (E'_x - E'_y)^2\}}$. As there is no common constant of motion for both domains, it is impossible to prolongate one foliation into the other, and the system is not integrable. However, these two passages are smooth and do not induce any instability in the process.

1.5 Bouncing Maps

One of the main advantages of billiards is the piecewise integrability of the dynamics between the collisions. One may use this property in order to reduce the dimension of the phase space of the system. Instead of studying the flow on the three dimensional energy shell, it may be easier to describe a trajectory by its intersections with a given submanifold in phase space. Such a representation is called a *Poincaré section*. Notice that to be well defined, the intersections have to be transverse, and one has to consider only intersections with a positive (or negative) sign of the perpendicular (with respect to the section) component of momentum. For billiards it is natural to take the section on the two dimensional manifold corresponding to the boundary. One may then choose momentum either immediately before or immediately after the collision. With this procedure, the dynamics is reduced to a two dimensional map that we will call a *Poincaré map* or a *bouncing map*.

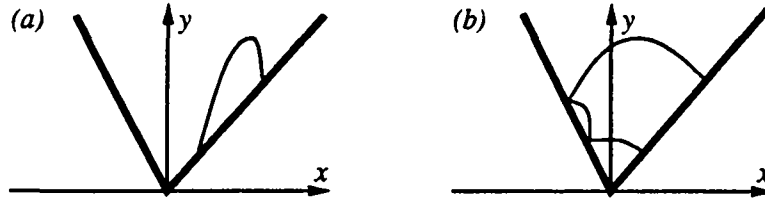


Fig. 1.8. Sketch of trajectories bouncing directly back on the same side (a) and bouncing against the other side in-between (b).

As each trajectory has to meet both the right and the left sides, it turns out to be advantageous to consider the restriction of the Poincaré section to one side only, say the right one. A trajectory may either turn back directly on the right side, or hit the left side several times first (see Fig.1.8). Coordinates corresponding to the tangential and perpendicular (with respect to the boundary) parts of the momentum p have been shown to be particularly convenient for the wedge [RSW, SG2], so that we set

$$\begin{aligned} X &= p_{\parallel} / \cos \beta_R \\ Y &= -p_{\perp} / \sin \beta_R. \end{aligned} \quad (1.34)$$

From now on, we will focus on the half wedge and consider only the Poincaré map

$$P : (X, Y) \mapsto (X', Y') \quad (1.35)$$

from the right side onto it. This considerably simplifies the analysis, since a particle may only bounce once against the left (vertical) side between two collisions with the right side. The domain of P with the coordinates (X, Y) is determined by energy conservation. Considering the momentum after the collision, we have $p_{\perp} > 0$, and hence obtain the half ellipse

$$Y \leq 0 \quad \text{and} \quad \left(\frac{X}{\sqrt{2E}/\cos \beta_R} \right)^2 + \left(\frac{Y}{\sqrt{2E}/\sin \beta_R} \right)^2 \leq 1. \quad (1.36)$$

The kinetic energy is maximal in the corner of the wedge. Hence it is represented by the boundary of this domain without the segment $Y = 0$ (see dashed line on Fig.1.9). According to whether the particle does meet or not the vertical side, the algebraic expression of the map will be different. Thus we will decompose P into two submaps T and V . When the particle comes back on the inclined boundary without bouncing against the other one we will say that it makes a T bounce [SG2]. It is straightforward to compute the algebraic form of this submap

$$T : \begin{cases} X' = X + 2Y \\ Y' = Y \end{cases} \quad (1.37)$$

which reduces to a shift in X direction in this case. When the particle hits the vertical side in between, it will be said that it makes a V bounce and the corresponding submap reads (see [RSW] or [SG2])

$$V : \begin{cases} X' = Y' - (X + Y) \\ Y' = -\sqrt{4E - 2\xi(X + Y)^2 - Y^2} \end{cases} \quad (1.38)$$

with $\xi = c^2(c^2 - s^2)$, $c = \cos \beta_R$ and $s = \sin \beta_R$. The regions where T and V apply are separated by the one dimensional submanifold

$$X = -2Y - \frac{1}{c}\sqrt{2E - s^2Y^2} \quad (1.39)$$

of the trajectories meeting the intersection of the sides. These coordinates are useful for numerous numerical and analytical purposes, since they provide the simplest algebraic form for the map P . Furthermore, it is believed that coding the periodic trajectories by their sequence of T and V leads to a different word for each periodic orbit of the half wedge with $\beta_R > \pi/4$ [SG2].

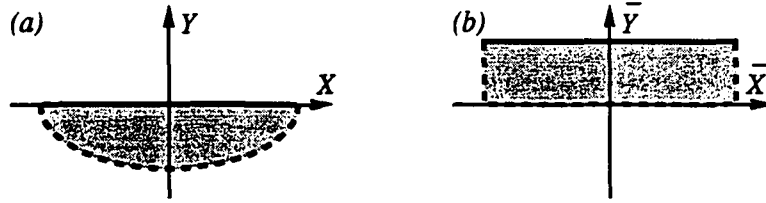


Fig. 1.9. Domains of the map P (a) and \bar{P} (b). The dashed line represents the vertex of the wedge, where kinetic energy is maximal.

However, these coordinates suffer from several drawbacks: the shape of domain is not very convenient, the map is not conservative and the integrable structure in the case $\beta_R = \pi/4$ is not obvious. This is why we introduce for the first time the coordinates

$$\begin{aligned} \bar{X} &= cX(2E - s^2Y^2)^{-1/2} \\ \bar{Y} &= (2E)^{-3/2}(2E - s^2Y^2)^{3/2} \end{aligned} \quad (1.40)$$

which solve all these problems. The associated map $\bar{P} : (\bar{X}, \bar{Y}) \mapsto (\bar{X}', \bar{Y}')$ is defined on the rectangle $[-1, 1] \times [0, 1]$ onto itself. Moreover, transformation (1.40) renders the map conservative (see next section). The submap \bar{T} expresses now as the shift

$$\bar{T} : \begin{cases} \bar{X}' = \bar{X} - 2\frac{c}{s}\sqrt{\bar{Y}^{-2/3} - 1} \\ \bar{Y}' = \bar{Y} \end{cases} \quad (1.41)$$

and the separation between the domains of \bar{T} and \bar{V} is given by the submanifold

$$\bar{X} = 2\frac{c}{s}\sqrt{\bar{Y}^{-2/3} - 1} - 1. \quad (1.42)$$

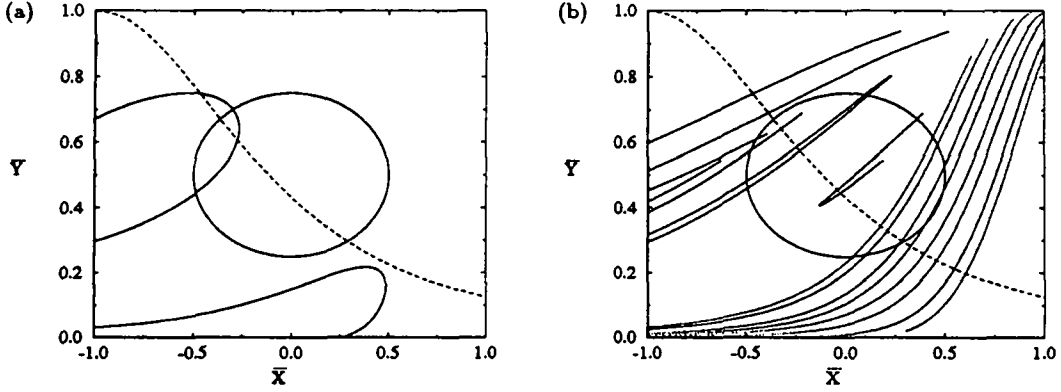


Fig. 1.10. Image of the circle centered in the middle of the rectangle after one (a) and four (b) iterations of \bar{P} for $\beta_R = \pi/3$. The dashed line represents the separation between the domain of \bar{T} (upper right part) and \bar{V} (lower left part).

In Fig. 1.10 we have plotted the first and fourth iterations of the map \bar{P} on the circle chosen in the middle of the domain. On the left plot, one can see that the part of the circle in the \bar{T} domain is shifted to the left, whereas the other part is deformed by the action of \bar{V} . The plot on the right puts into evidence the hyperbolic directions of the map.

When $\beta_R = \pi/4$, the system with continuous time is integrable. Replacing $c = s = 2^{-1/2}$ in the above expressions, we obtain

$$\bar{T}|_{\beta_R=\pi/4} : \begin{cases} \bar{X}' = \bar{X} - 2\sqrt{\bar{Y}^{-2/3} - 1} \\ \bar{Y}' = \bar{Y} \end{cases} \quad (1.43)$$

$$\bar{V}|_{\beta_R=\pi/4} : \begin{cases} \bar{X}' = (\bar{X} - 1)/\sqrt{\bar{Y}^{-2/3} - 1} - 1 \\ \bar{Y}' = (1 - \bar{Y}^{2/3})^{3/2} \end{cases} \quad (1.44)$$

but the map \bar{P} still does not reflect integrability. Looking back at Fig. 1.6 one realizes that the section $\bar{y} = 0$ appears four times on the unfolded torus. Thus, taking all points of a trajectory on the section mixes both angle variables. To observe the integrable structure, we must consider only the section with a fixed direction on the unfolded torus. Another way to understand this is to notice that a \bar{V} bounce exchanges the values of the energies $E_{\bar{x}}$ and $E_{\bar{y}}$. Until the next \bar{V} bounce, where the initial setting of energy will be recovered, the coordinates (\bar{X}, \bar{Y}) describe motion perpendicular to the initial direction on the torus. Thus we must forget the collisions between two consecutive \bar{V} bounces. This prescription yields the new map \bar{P}^* : $(\bar{X}, \bar{Y}) \mapsto (\bar{X}', \bar{Y}')$ composed of the submaps \bar{T} and $\bar{W}(m) = \bar{V} \circ \bar{T}^m \circ \bar{V}$, where m denotes the number of \bar{T} bounces between the consecutive \bar{V} bounces, and \bar{T}^m the m th iterate of \bar{T} . The algebraic expression of $\bar{W}(m)$ reads

$$\overline{W}(m) : \begin{cases} \overline{X}' &= \overline{X} - 2\sqrt{\overline{Y}^{-2/3} - 1} + 2(m+1) \\ \overline{Y}' &= \overline{Y} \end{cases} \quad (1.45)$$

so that \overline{P}^* reduces to a rotation (up to a factor π which may be added in transformation 1.40) on the periodic coordinate $\overline{X} \bmod 2$. As a direct consequence, the trajectories are periodic or quasiperiodic according to whether $\sqrt{\overline{Y}^{-2/3} - 1}$ is rational or not.

Treating \overline{X} as a circular coordinate necessitates identification of the boundaries $\overline{X} = \pm 1$. As these boundaries correspond to collisions with the vertex, we have to investigate what happens near to the corner. As already stated, bouncing in the corner is generally not defined since the normal to the boundary is not uniquely defined. It may be shown (see appendix A.1 and [DR]) that close to corners, the behavior of the trajectory depends on the first side hit, except when the angle β of the corner is of the type $\beta = \pi/n$ with $n \in \mathbb{N}$. In this latter case, it is possible to define collisions in the corner by continuity, since both limit trajectories leave the corner in the same direction after bouncing n times alternately against both sides of the vertex. We have seen that the points which will be mapped on the corner are laying on the separation (1.42) of the domains of \overline{T} and \overline{V} . Initial conditions close to this curve in the \overline{T} domain make a sequence of $\overline{V}^4 \circ \overline{T}$ bounces, whereas the ones in the \overline{V} domain are mapped according to $\overline{T} \circ \overline{V}^4$. Because of the simplicity of the map for $\beta_R = \pi/4$, one may evaluate explicitly both expressions and finds

$$\overline{V}^4 \circ \overline{T} \Big|_{\substack{\beta_R = \pi/4 \\ \overline{X} = 2\sqrt{\overline{Y}^{-2/3} - 1} - 1}} = \overline{T} \circ \overline{V}^4 \Big|_{\substack{\beta_R = \pi/4 \\ \overline{X} = 2\sqrt{\overline{Y}^{-2/3} - 1} - 1}} \quad (1.46)$$

so that the map does not contain any singularity. Moreover, the identification of the boundaries $\overline{X} = \pm 1$ follows from the special rule of reflection in the corner.

As the shift on the \overline{X} variable in (1.44) is a monotonous function of \overline{Y} , the map \overline{P}^* defines a twist map on a cylinder. Changing the value of β_R is a strong perturbation of this twist map, since reflections in the corner are no more defined. The integrable structure is ruined by the effect of the singularity, as we will see below. One way of obtaining a smoother perturbation of this system is to consider a wedge with $\beta_L \neq 0$ such that $\beta_R = \pi/4 - \beta_L$, where bouncing in the corner is well defined. Choosing $\beta_L < 0$ introduces a new set of singularities corresponding to trajectories tangent to the boundary, so that the perturbed system is also discontinuous. Setting $\beta_L > 0$ yields a C^0 perturbed system, which unfortunately loses the twist property playing a central role in the case of a twist map.

Another object of interest is the Poincaré Scattering Map, usually given as a function of the action I corresponding here to the asymptotic action in y direction, and the reduced angle variable

$$\tilde{\varphi} = \varphi - \left(\frac{3\pi I}{2\sqrt{2}} \right)^{-1/3} \frac{\pi x}{\sqrt{2} p_x}. \quad (1.47)$$

The quantity $\tilde{\varphi}$ may be checked to be constant in the asymptotic domain. It corresponds to the angle φ at $x = 0$. One can imagine a mechanism of re-injection of the particle in the scattering system which would be described by iterations of the PSM. Although the PSM is not chaotic, iterations of the map will yield a chaotic system. Such a system is in fact completely equivalent to the half wedge with the same angle β_R , and the PSM is nothing else but the bouncing map defined from the vertical side onto itself (up to a change of coordinates).

1.6 Invariant Measures and Conservative Maps

When giving a probabilistic description of a system, exceptional orbits (which are not representative of the system) have to be neglected in favor of typical ones. Then one says that a property is valid for almost all orbits of the system. To render clear the meaning of this concept, we introduce the notion of measure which is the basics of ergodic theory (see [ER]). For a probability density $\rho(\mathbf{x}) \geq 0$ on the Euclidean space \mathbb{R}^d , we define the probability measure μ in a region A as

$$\mu(A) = \int_A d\mu = \int_A dx \rho(\mathbf{x}). \quad (1.48)$$

The N dimensional volume in \mathbb{R}^N is known as *Lebesgue measure*. An *invariant measure* for a map P is a measure with the property

$$\mu(A) = \mu(P^{-1}(A)) \quad \forall A \subset \mathbb{R}^d. \quad (1.49)$$

An invariant probability measure μ which can not be written as the sum $\frac{1}{2}\mu_1 + \frac{1}{2}\mu_2$ of two invariant probability measures $\mu_1 \neq \mu_2$ is called *indecomposable* or *ergodic*. When μ is ergodic (and normalized to one), Birkhoff's ergodic theorem asserts that for almost all initial condition $\mathbf{x}(0)$ with respect to the measure μ and for every continuous function $g(\mathbf{x})$,

$$\lim_{n \rightarrow \infty} \frac{1}{n} \sum_{k=0}^{n-1} g(P^k \mathbf{x}(0)) = \int dx \mu(\mathbf{x}) g(\mathbf{x}) \quad (1.50)$$

so that a time average equals a space average.

Similarly, one may define invariant and ergodic measures associated to a flow. For a Hamiltonian system with d freedoms, we know from Liouville's theorem that the volume is preserved by the Hamiltonian flows. Thus, the invariant measure is the Lebesgue measure

$$d\mu = dq_1 \dots dq_d dp_1 \dots dp_d. \quad (1.51)$$

When focusing on a single energy shell $H = E$, preservation of volume in the whole phase space yields the Liouville measure

$$d\mu = \frac{d\sigma}{|\nabla H|} \quad (1.52)$$

for an element of area $d\sigma$ in the shell.

The flow between two collisions of the billiard may be seen as the geodesic flow on a Riemannian manifold with metric $g_{ij} = (E - V(\mathbf{q})) \delta_{ij}$ induced by the potential $V(\mathbf{q})$. Setting $d\rho(\mathbf{q})$ the element of volume generated by the Riemannian metric in configuration space and $d\omega(\mathbf{q})$ the Lebesgue measure into the sphere of codimension 1 in momentum space, it may be shown that the measure

$$d\mu = d\rho(\mathbf{q}) d\omega(\mathbf{q}) \quad (1.53)$$

is invariant with respect to the flow (see [CFS]). For the map, one may also deduce the invariance of the corresponding measure “into the boundary”

$$d\mu = \sin \theta d\rho(\ell) d\omega(\ell) \quad (1.54)$$

where θ is the angle that the momentum p makes with the tangent to the boundary, ℓ the Euclidean arc length on the boundary, $d\rho(\ell)$ the element of volume generated by the metric into the boundary and $d\omega(\ell)$ the Lebesgue measure on the circle.

Birkhoff introduced the coordinates $(\cos \theta, \tilde{\ell})$, with $\tilde{\ell}$ the arc length in the metric induced by the potential. They are such that the invariant measure equals the area

$$d\mu = d(\cos \theta) d\tilde{\ell} \quad (1.55)$$

since $d\tilde{\ell} = \sqrt{E - V} d\ell$. Thus, the bouncing map expressed as a function of these coordinates verifies

$$\left| \frac{\partial(\cos \theta', \tilde{\ell}')}{\partial(\cos \theta, \tilde{\ell})} \right| = 1 \quad (1.56)$$

and is said to be *area preserving*. It may be more convenient to associate the volume element generated by the metric to the angle and use the coordinates $(p_{\parallel} = |p| \cos \theta, \ell)$. As

$$dp_{\parallel} d\ell \propto \sqrt{E - V} d(\cos \theta) d\ell \quad (1.57)$$

these coordinates also yield a conservative map.

Such coordinates may be of great help when discussing the mechanisms of expansion in the dynamics, or computing ensemble properties of the system invoking Birkhoff's theorem. Moreover, they can be used to determine the associated invariant measure

to a given set of coordinates. Evaluating the Jacobian of the transformation $(p_{\parallel}, \ell) \mapsto (X, Y)$, we get

$$dp_{\parallel} d\ell = \left| \frac{\partial(p_{\parallel}, \ell)}{\partial(X, Y)} \right| dX dY = s^2 |Y| dX dY \quad (1.58)$$

so that the density $\rho(X, Y) = |Y|$ yields an invariant measure. The Jacobian of the bouncing map $(X, Y) \mapsto (X', Y')$ (for any values of the angles β_R and β_L) may be computed from the composition of the transformations and reads

$$\left| \frac{\partial(X', Y')}{\partial(X, Y)} \right| = \left| \frac{\partial(X', Y')}{\partial(p'_{\parallel}, \ell')} \right| \left| \frac{\partial(p'_{\parallel}, \ell')}{\partial(p_{\parallel}, \ell)} \right| \left| \frac{\partial(p_{\parallel}, \ell)}{\partial(X, Y)} \right| = \frac{|Y|}{|Y'|}. \quad (1.59)$$

It is then straightforward to check that the maps $(X, Y^2) \mapsto (X', Y'^2)$ and $(\bar{X}, \bar{Y}) \mapsto (\bar{X}', \bar{Y}')$ are area preserving. This characteristic will be reflected in the homogeneity of the dots in the Poincaré sections corresponding to stochastic components.

1.7 Special Orbits

We have seen in the previous section that the vertex is not a singularity of the half wedge with $\beta_R = \pi/4$. We prove in appendix A.1 that trajectories bouncing in the corner of a Euclidean billiard are well defined for angles $\beta = \pi/n$ with $n \in \mathbb{N}$. We also show how this result may be extended to the wedge billiard. To understand what happens in the corner, it is easier to look at the trajectories in the unfolded space, where the $2n$ copies of the original angle tile the plane (see Fig.1.11). In the Euclidean case, it is clear that two trajectories starting in the same direction, but colliding with both sides in a different order, will leave the corner with the same velocity.

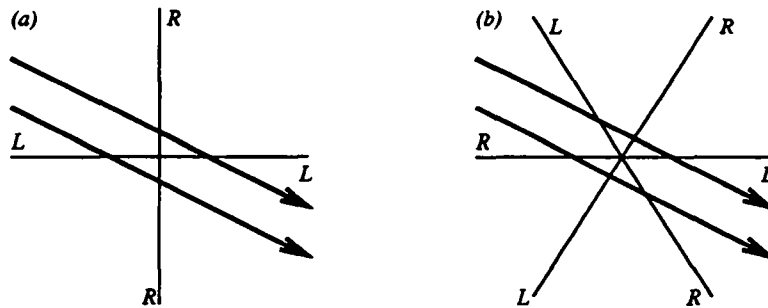


Fig. 1.11. Unfolded corners with angle $\beta = \pi/2$ (a) and $\beta = \pi/3$ (b).

Thus, when taking the limit of a trajectory bouncing exactly in the vertex, the final direction of the velocity does not depend on the first side met by the particle. Since

both limits yield the same issue, definition of such a collision by continuity makes sense³. A very simple reflection law may be deduced from this procedure:

- i) If n is even, the reflected velocity is the opposite of the incident velocity (the particle makes a half turn).
- ii) If n is odd, the incident and reflected velocities are symmetric with respect to the bisector of the angle.

The symmetries are different in the case n odd and n even, as one can check on Fig. 1.11. Moreover, one can prove for even n that not only the trajectory but its linearization is well defined around the corner (see appendix A.1).

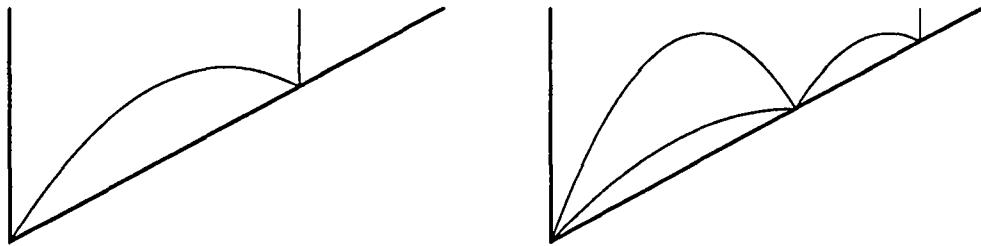


Fig. 1.12. Examples of well defined periodic orbits bouncing in the vertex of a half wedge with $\beta_R = \pi/3$.

These trajectories form a zero-measure set in phase space [CFS, St] and hence are often neglected. The wedge billiard provides a good example of a system where such orbits have to be considered, especially when using semiclassical theories based on periodic orbits.

We mentioned previously that \bar{T} bounces reduce to a shift in \bar{X} direction while \bar{Y} remains constant. When \bar{Y} tends to one, the value of the shift goes to zero, so that the particle tends to make more and more \bar{T} bounces before entering the \bar{V} domain. The number $N_{\bar{T}}$ of successive \bar{T} bounces as a function of \bar{X} and \bar{Y} reads

$$N_{\bar{T}}(\bar{X}, \bar{Y}) = \text{Ent} \left[\frac{s}{2c} (\bar{X} + 1) \left(\bar{Y}^{-2/3} - 1 \right)^{-1/2} \right] \quad (1.60)$$

where $\text{Ent}[\cdot]$ denotes here the integer part of a number. Thus trajectories with $\bar{Y} \approx 1$ are making a lot of successive close bounces on the right side. This is why we will

³Notice that this property finds an interpretation in terms of the original model of three particles on a line treated in the first section. Generally the triple collision may not be considered as the limit of two simple collisions, because they do not permute. For given ratios of the masses (recall that β only depends on the masses) both issues are the same, regardless of the order of the collisions. This is obviously the case when $m_1 = m_2 = m_3$ where $\beta = \pi/3$.

call them *grazing orbits*. The function $N_{\bar{T}}$ admits a singularity at $\bar{Y} = 1$ which corresponds to a trajectory sliding along the inclined side. Such a trajectory is not described by the bouncing map, since it is not transverse to the section. Furthermore, it is going straight into the corner and hence is well defined only when $\beta = \pi/n$.

The time that the particle spends in the wedge between two successive \bar{T} bounces, or *flying time*, reads

$$\Delta t_{\bar{T}}(\bar{X}, \bar{Y}) = \frac{1}{s} \sqrt{2E \left(1 - \bar{Y}^{2/3}\right)} \quad (1.61)$$

and clearly tends to zero when $\bar{Y} \rightarrow 1$, so that the total time for for the $N_{\bar{T}}$ bounces

$$N_{\bar{T}} \Delta t_{\bar{T}} = \sqrt{\frac{E}{2}} \bar{Y}^{1/3} (\bar{X} + 1) \quad (1.62)$$

becomes finite. Hence in the limit $\bar{Y} \rightarrow 1$, the grazing orbits are making an infinite number of bounces in a finite time. These kinds of orbits appear whenever there is a part of the boundary along which motion is integrable, such as the arcs of a circle in the stadium [SSCL]. We will see that they may have some influence on the statistical behavior of the discrete system.

2. Numerical Results on Classical Mechanics

2.1 Preliminary

In this second chapter we analyze the instability of the dynamics with the help of quantities evaluated numerically (see [PC]). The accent is rather set on the physical implications than on the numerical methods.

First we investigate the rate of exponential divergence of pairs of orbits measured by the Lyapunov exponent. Richter Scholz and Wittek computed its behavior as a function of the angle. They discovered an oscillation with decreasing amplitude that they called “breathing” [RSW]. Because of the decay of the amplitude with the angle, Wittek conjectured that the model is probably integrable in the limit of very small angles [Wi]. We show that this decay is an artifact of the discrete exponent, which disappears if one considers the exponent related to the flow.

Then we analyze the decay rate of the correlation functions at a fixed angle. We show with semi-analytical methods that the correlations do not decrease exponentially, as one would expect for a system with a positive Lyapunov exponent. Long tails in the correlations arise because of the inclined boundary along which motion is integrable [VCG].

We close this chapter with some comments about the partitioning of phase space by the pre-images of the singularity. These considerations may find applications for systems presenting mixed behavior, since for completely chaotic systems the expansion mechanism prevails on the partitioning. We show that most of the time the set of pre-images of the singularities forms a network that invariant tori can not cross. This is a first step in the study of systems with mixed phase space, which turn out to be harder to characterize than completely chaotic systems.

2.2 Lyapunov Exponents

A measure of the instability of a chaotic system is given by the Lyapunov exponents, which account for the sensitive dependence on initial conditions. We consider the trajectory (\bar{X}_n, \bar{Y}_n) corresponding to the n th iterate of the Poincaré map \bar{P} on the initial condition (\bar{X}_0, \bar{Y}_0) . Suppose that we add an infinitesimal perturbation $(\delta\bar{X}_0, \delta\bar{Y}_0)$ to the initial condition, which becomes $(\bar{X}_0 + \delta\bar{X}_0, \bar{Y}_0 + \delta\bar{Y}_0)$. After n iterations of the map, both trajectories differ from

$$\begin{pmatrix} \delta\bar{X}_n \\ \delta\bar{Y}_n \end{pmatrix} = D\bar{P}^n|_{(\bar{X}_0, \bar{Y}_0)} \begin{pmatrix} \delta\bar{X}_0 \\ \delta\bar{Y}_0 \end{pmatrix} \quad (2.1)$$

where

$$D\bar{P}^n|_{(\bar{X}_0, \bar{Y}_0)} = D\bar{P}|_{(\bar{X}_{n-1}, \bar{Y}_{n-1})} \cdots D\bar{P}|_{(\bar{X}_0, \bar{Y}_0)} \quad (2.2)$$

and the length of the vector $(\delta\bar{X}_n, \delta\bar{Y}_n)$ reads

$$|(\delta\bar{X}_n, \delta\bar{Y}_n)|^2 = (\delta\bar{X}_0, \delta\bar{Y}_0) (D\bar{P}^n)^T D\bar{P}^n \begin{pmatrix} \delta\bar{X}_0 \\ \delta\bar{Y}_0 \end{pmatrix}. \quad (2.3)$$

It is not hard to check¹ that the map $(\bar{X}, \bar{Y}) \mapsto D\bar{P}|_{(\bar{X}_0, \bar{Y}_0)}$ verifies the assumptions of Oseledec's theorem [Os] on each ergodic component. This theorem asserts that the limit

$$\Lambda = \lim_{n \rightarrow \infty} \frac{1}{2n} \ln \left[(D\bar{P}^n)^T D\bar{P}^n \right] \quad (2.4)$$

exists. The eigenvalues of the symmetric matrix Λ are called *Lyapunov exponents* of the system. Because of the area preserving character of \bar{P} , both exponents are opposite, and may be written as the pair $(\lambda, -\lambda)$ with $\lambda \geq 0$. When $\lambda > 0$, we have

$$|(\delta\bar{X}_n, \delta\bar{Y}_n)| \propto e^{n\lambda} |(\delta\bar{X}_0, \delta\bar{Y}_0)| \quad (2.5)$$

so that the error on the initial condition grows exponentially, pointing out the instability of the system. For an initial condition pointing on a quasiperiodic trajectory, the length of the vector increases only linearly with n and the Lyapunov exponent is zero.

For the flow of the continuous system, Lyapunov exponents are defined in a similar way. The phase space being three dimensional, there is one more exponent which vanishes, since it corresponds to the time direction. Hence we will write them $(\tilde{\lambda}, 0, -\tilde{\lambda})$ with $\tilde{\lambda} \geq 0$. The Lyapunov exponents of the flow are related to the one of the discrete system (see [ER]) by

¹Oseledec's theorem requires $\int d\mathbf{x} \rho(\mathbf{x}) \ln^+ \|DP_{(\mathbf{x})}\| < \infty$, with ρ the invariant probability density. Here, using the sup norm in the coordinates (X, Y) and the density $\rho(X, Y) = |Y|$, one can even show that $\int dX dY \rho(X, Y) \|DP_{(X, Y)}\| < \infty$, so that the theorem applies.

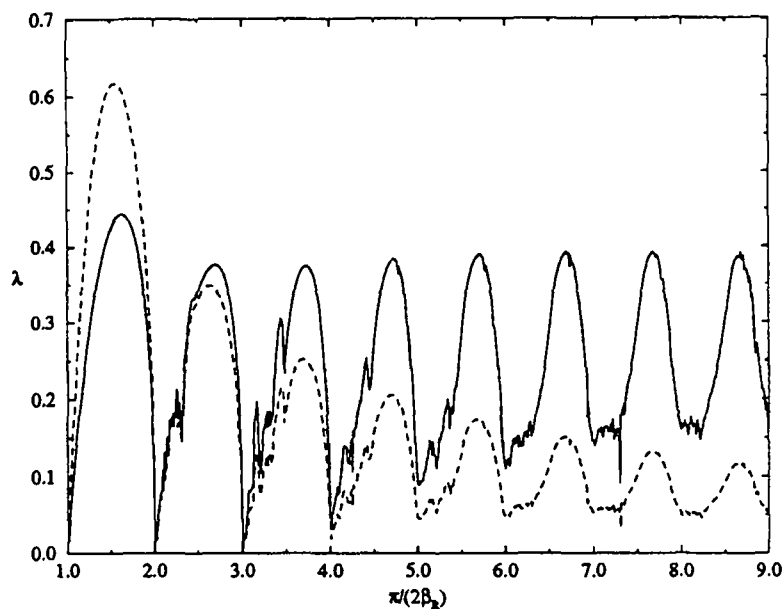


Fig. 2.1. Lyapunov exponent of the map (dashed line) and the flow (solid line) of the half wedge as a function of the ratio $\frac{\pi}{2\beta_R}$. The exponent is measured along a single trajectory making 10 million bounces on the inclined side of the wedge. The initial condition belongs to the largest stochastic component.

$$\tilde{\lambda} = \frac{\lambda}{\langle \Delta t_{\bar{P}} \rangle} \quad (2.6)$$

where $\langle \Delta t_{\bar{P}} \rangle$ denotes the averaged time between two crossing of the Poincaré section (computed with respect to a probability measure). Wojtkowski has shown that the flow of the wedge with $\beta > \pi/2$ and the half wedges with $\beta_R > \pi/4$ have an almost everywhere non-vanishing Lyapunov exponent [Wo]. As both the return time and the phase space are bounded, the above time average is well defined. Hence one may deduce the existence of an almost everywhere non-vanishing Lyapunov exponent for the discrete system within the same range of parameters.

The Lyapunov exponent of the bouncing map corresponding to the half wedge with $0 < \beta_R < \pi/2$ has been the object of several numerical studies [MR, RSW, Wi]. It turns out that λ shows local minima around the angles $\beta_R = \frac{\pi}{2n}$ with $n \in \mathbb{N}$ (see dashed curve in Fig. 2.1), indicating less chaotic dynamics. As the envelope of λ decreases when $\pi/(2\beta_R) \rightarrow \infty$, one may think that the wedge becomes integrable in the limit $\beta_R \rightarrow 0$. In Fig. 2.1 we have reproduced the Lyapunov exponent λ of the map and computed $\tilde{\lambda}$ corresponding to the flow. As the quantity $\langle \Delta t_{\bar{P}} \rangle$ is a monotonous function of β_R , the oscillatory behavior of λ is reflected in $\tilde{\lambda}$, which also shows local minima around the values $\beta_R = \frac{\pi}{2n}$. The envelope of $\tilde{\lambda}$ does not seem to decrease when β tends to zero. This difference arises from the fact that

$$\lim_{\beta_R \rightarrow 0} \langle \Delta t_{\bar{P}} \rangle \rightarrow 0. \quad (2.7)$$

In both cases, the particle may not move far away in one bounce, but the exponent of the continuous time system takes into account the fact that collisions happen closer to each other, whereas the exponent of the discrete system indicates slower expansion.

Hence we conjecture that the system is *not* integrable in the limit of very small angles.

2.3 Correlation Functions

The existence of positive Lyapunov exponents is pointing out the exponential instability of motion, which implies that the memory of the initial state is lost exponentially fast. However, we shall see that this does not lead to exponential decay of the correlations.

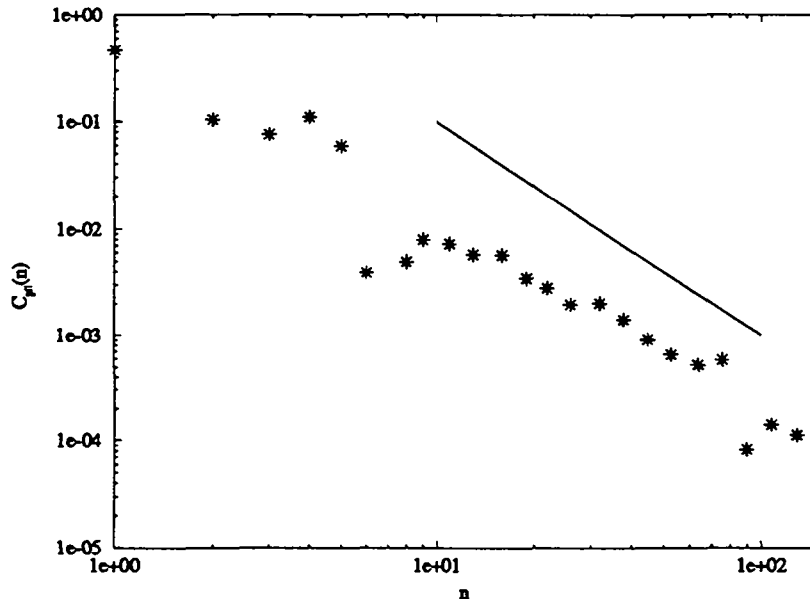


Fig. 2.2. Log-log plot of the correlation function $C_{p_{\parallel}}(n)$ for the half wedge with $\beta_R = \pi/3$. The correlation function is measured along a single trajectory bouncing $1e8$ times against the inclined side of the wedge. The solid line has slope -2.

Here we investigate the long time behavior of the correlation functions

$$C_f(n) = \lim_{m \rightarrow \infty} \frac{1}{m} \sum_{k=0}^{m-1} f(P^k \mathbf{x}(0)) f(P^{k+n} \mathbf{x}(0)) - \left[\lim_{m \rightarrow \infty} \frac{1}{m} \sum_{k=0}^{m-1} f(P^k \mathbf{x}(0)) \right]^2 \quad (2.8)$$

for smooth phase space functions f . Figure 2.2 represents the momentum-momentum correlation function $C_{p_{\parallel}}(n)$ for the half wedge with $\beta_R = \pi/3$. The value of the

function for a given n is obtained following a trajectory for 10^8 bounces. For large n we observe that $C_{p_{\parallel}}(n) \propto n^{-2}$, so that trajectories remain correlated for a long time. This clearly shows that correlation functions characterize the system in a different way than Lyapunov exponents.

Existence of long tails in billiards is due to integrable segments of motion [VCG]. As a successive sequence of T bounces is isomorphic to a rotation, grazing orbits which may bounce arbitrarily many times against the inclined side may also be correlated for arbitrarily long time. Because of ergodicity, almost all orbits must spend some time in the region where the dynamics is locally integrable. Invoking the ergodic theorem, one may replace the integral over time by an integral over space for large n , leading to

$$C_f(n) = \frac{1}{2} \int_{\text{Dom}(\bar{P})} d\bar{X} d\bar{Y} f(\bar{X}, \bar{Y}) f(\bar{P}^n(\bar{X}, \bar{Y})) - \left[\frac{1}{2} \int_{\text{Dom}(\bar{P})} d\bar{X} d\bar{Y} f(\bar{X}, \bar{Y}) \right]^2 \quad (2.9)$$

where $\text{Dom}(\bar{P})$ denotes the whole phase space. Similarly, we will write $\text{Dom}(\bar{V})$ and $\text{Dom}(\bar{T})$ for the domains where \bar{V} and \bar{T} apply respectively. As we are discussing the asymptotic behavior of $C_f(n)$ we can forget about the constant term, which in particular vanishes for $f = p_{\parallel}$.

Due to the simple geometry of phase space in coordinates (\bar{X}, \bar{Y}) , the domain where the particle does n successive \bar{T} bounces reads

$$\text{Dom}(\bar{T}^n) = \left\{ (\bar{X}, \bar{Y}) \in [-1, 1] \times [0, 1] \mid \bar{X} + 1 \geq 2n \frac{c}{s} \sqrt{\bar{Y}^{-2/3} - 1} \right\}. \quad (2.10)$$

The ratio

$$\frac{\mu(\text{Dom}(\bar{T}^n))}{\mu(\text{Dom}(\bar{P}))} = \frac{1}{2} \int_{\text{Dom}(\bar{T}^n)} d\bar{X} d\bar{Y} \propto \frac{1}{n^2} \quad (2.11)$$

gives the fraction of the total time spent in sequences of consecutive \bar{T} bounces longer than n . The decaying rate of $C_f(n)$ coincides with the behavior of $\mu(\text{Dom}(\bar{T}^n))$ for large n , provided that the function f does not vanish on $\text{Dom}(\bar{T}^n)$ when $n \rightarrow \infty$. In this latter case, as for instance for $f = p_{\perp}$, one can still compute the estimate

$$C_f(n)|_{\text{Dom}(\bar{T}^n)} = \frac{1}{2} \int_{\text{Dom}(\bar{T}^n)} d\bar{X} d\bar{Y} f(\bar{X}, \bar{Y}) f(\bar{P}^n(\bar{X}, \bar{Y})) \quad (2.12)$$

which gives the dominant contribution to $C_f(n)$. Evaluating this estimate for $f = p_{\parallel}$ and $f = p_{\perp}$, we obtain the asymptotic behaviors

$$C_{p_{\parallel}}(n)|_{\text{Dom}(\bar{T}^n)} \propto \frac{1}{n^2} \quad \text{and} \quad C_{p_{\perp}}(n)|_{\text{Dom}(\bar{T}^n)} \propto \frac{1}{n^4}. \quad (2.13)$$

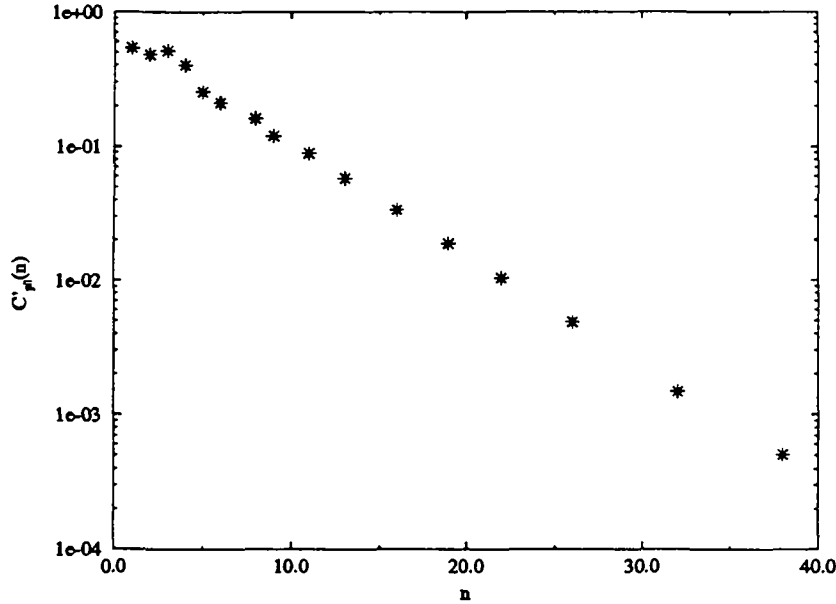


Fig. 2.3. Lin-log plot of the modified correlation function $C'_{p_{\parallel}}(n)$ for the half wedge with $\beta_R = \pi/3$. The correlation function is measured along a single trajectory bouncing $1e8$ times against the inclined side of the wedge.

This computation only shows that the contribution of the region $\text{Dom}(\overline{T}^n)$ decreases at a given rate, but nothing is said about the behavior of the contribution of $\text{Dom}(\overline{P}) \setminus \text{Dom}(\overline{T}^n)$. One way of suppressing the effect of integrable segments of trajectories is to neglect all points except one for any integrable segment occurring in the orbit [VCG]. In Fig. 2.3 we represent the modified correlation function $C'_{p_{\parallel}}(n)$ computed with the above prescription along the same trajectory as before. The decaying rate of $C'_{p_{\parallel}}(n)$ looks like exponential, comforting the hypothesis that integrable segments are responsible for long tails.

Very interesting is the fact that for the system with continuous time, arbitrarily long sequences of T bounces happen in a finite time. Thus, the correlation function for the flow will not present a long tail, and its asymptotic behavior will look like the one of $C'_{p_{\parallel}}(n)$. This provides a second example where the statistical properties of a system may change when going from continuous time to discrete time (see [CFS]).

However, one should not deduce from the above simulations that correlation functions of the continuous time system are decaying exponentially. It has been shown that singularities, such as orbits in phase space coming tangent to the boundary, are responsible for a slowing down of the decaying rate, which turns out to be quasiexponential despite the presence of exponential instability (see [Bu]). Thus the exact asymptotic behavior of the correlation functions depends on very fine properties of the system and is very hard to tackle numerically. However, computers are useful to

give an approximation of the decay, or to determine the value of the constant, once the system has been investigated analytically.

2.4 Role of Singularities

Billiards are defined on Riemannian manifolds with a piecewise smooth boundary. If the boundary is a C^n function, the normal is C^{n-1} and the bouncing map will generally be C^{n-1} . In the corners the boundary is C^0 . Thus the normal is not defined and the map is not defined either. We have seen that when the angle is of the type π/n with $n \in \mathbb{N}^*$, it is possible to define a collision in the corner as the limit of the composition of n iterations of the map. As both limits (obtained when hitting the left of the right side first) give the same result, P^n is locally continuous around the corner.

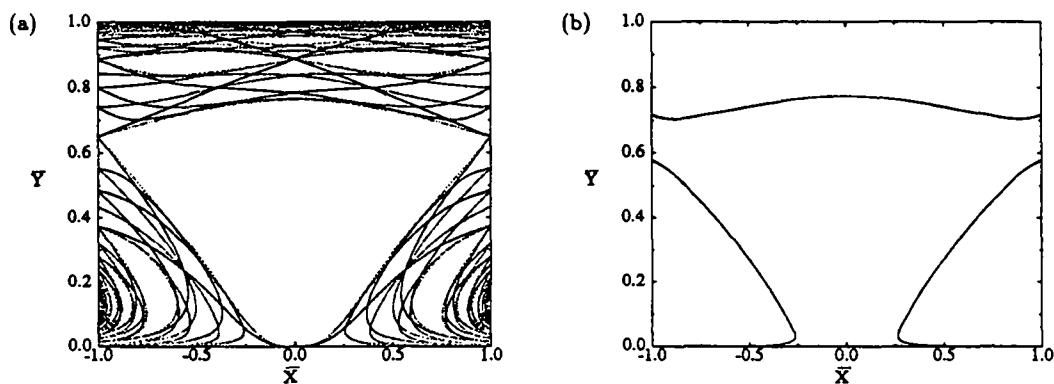


Fig. 2.4. (a) First 10 pre-images of the singularity for the half wedge with $\beta_R = \pi/6$. (b) Invariant set which seems to cross the set of pre-images.

When the angle is not of the type π/n , both limits are different and it is not possible to define the map locally in a continuous way. We will denote $\mathcal{S}_0 \subset \text{Dom}(P)$ the set of points in phase space belonging to the top of the corner ². This set is composed of pieces of submanifolds of codimension one. Denoting P^{-1} the inverse of the map P , the map P is discontinuous on the set $\mathcal{S}_1 = P^{-1}\mathcal{S}_0$.

Suppose that an invariant torus \mathcal{T} is crossing the set \mathcal{S}_1 corresponding to an angle $\beta \neq \pi/n$. The dynamics on the torus is a smooth rotation, whereas P is discontinuous at $\mathcal{T} \cap \mathcal{S}_1$. In order that \mathcal{T} remains smooth under the evolution, there must be another singularity which cancels the effect of the first one. This cutting and pasting

²This reasoning is also valid for other singularities of the system, such as points of the boundary where the geodesic curvature is negative. Exact definitions of the sets of singularities and of the inverse bouncing map may be found in [DR].

of the dynamics is quite unusual, but not unreal (see [DR] for an example on a Euclidean billiard). In this case the continuity of a power of P is not a consequence of the local, but of the global shape of the billiard. Thus, except in very special cases, tori may cross the set of pre-images \mathcal{S}_1 only if the angle is of the type π/n . Iterating the map P backwards and using the invariance $P^{-1}\mathcal{T} = \mathcal{T}$, it is clear that if $\mathcal{T} \cap \mathcal{S}_1 = \emptyset$, \mathcal{T} will not cross the sets $\mathcal{S}_k = P^{-k}\mathcal{S}_0$ of the k th pre-images either.

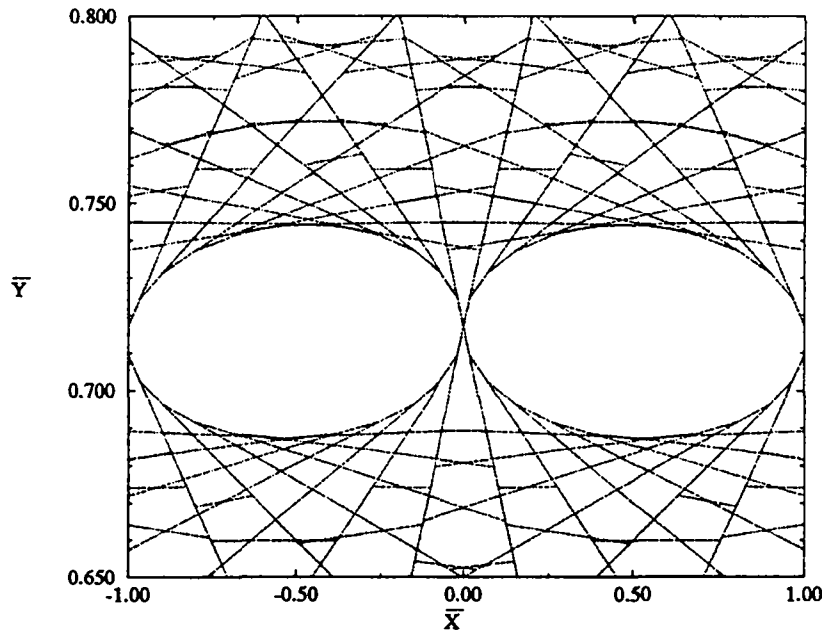


Fig. 2.5. Network of the first 20 pre-images of the singularity for the half wedge with $\beta_R = 44.9^\circ$.

Let's consider the set $\mathcal{S} = \bigcup_{k=0}^{\infty} \mathcal{S}_k$ of all the pre-images of the singularity. By the action of P , \mathcal{S}_k is mapped continuously onto \mathcal{S}_{k-1} , except at the points belonging to $\mathcal{S}_k \cap \mathcal{S}_1$. Thus the image of the discontinuities will lay on \mathcal{S}_0 , and the whole union is organized in a huge network which partitions phase space (see Fig. 2.5). The set \mathcal{S}_1 separates phase space into two regions where T and V apply. The set $\mathcal{S}_1 \cup \mathcal{S}_2$ defines partitions (not necessarily connected) where the four compositions $T \circ T$, $T \circ V$, $V \circ T$ and $V \circ V$ apply. Similarly, the union $\bigcup_{k=1}^m \mathcal{S}_k$ partitions phase space with respect to the 2^m different compositions of the submaps T and V . The region corresponding to one or more given compositions may be empty. Thus the associated sequence of T and V will never be encountered when coding an orbit, and one says that the sequence (or *word*) is *pruned*. In each open set which has no intersection with \mathcal{S} , the dynamics reduces to the iteration of a finite fixed sequence of the submaps. The stochasticity which may appear in such a region is then due to the nonlinearity of the resulting map, and has nothing to do with singularities.

Although \mathcal{S} has zero measure, it may be dense in some region. When $\beta \neq \pi/n$, these regions may not be crossed by tori. This is not enough to create chaos, in the sense of exponential instability. This mechanism may connect several stochastic regions so

that the unstable manifold of any unstable orbit may extend over a greater region of phase space. When $\beta \neq \pi/n$ and \mathcal{S} is dense in the whole phase space, there is no region foliated in tori. Nevertheless, this does not mean that each point of phase space is uniquely coded by the semi-infinite sequence of the submaps, since the partition corresponding to a given word is not necessarily connected. Hence the same sequence may be also associated to another region of phase space.

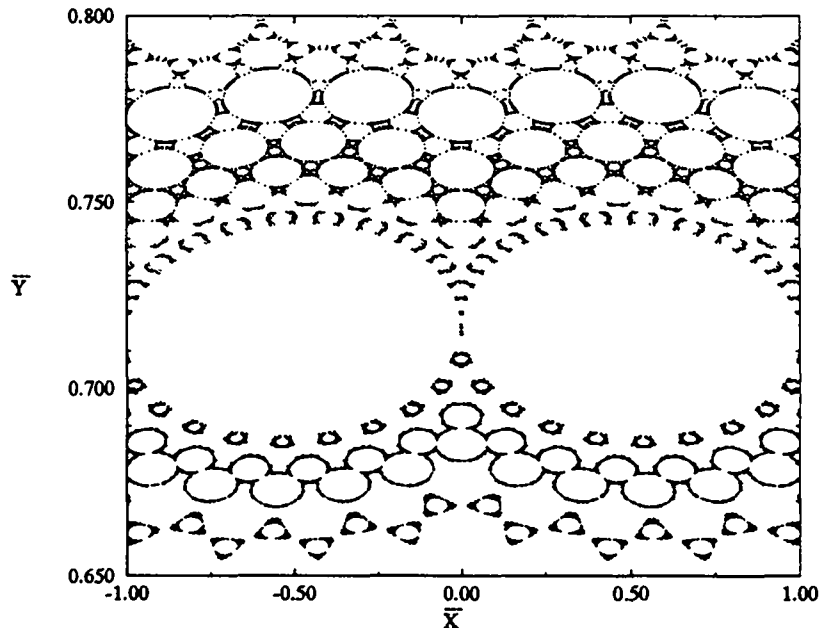


Fig. 2.6. Stochastic trajectory of the half wedge with $\beta_R = 44.9^\circ$. The stochastic zone is well represented by the set of the first pre-images of the singularity. The regions avoided by the trajectory are foliated in invariant tori. The organization of tori looks like fractal, but there is no mathematical evidence for it.

As an example, it is straightforward to verify that \mathcal{S} is dense in the whole phase space of the half wedge with $\beta_R = \pi/4$. This only means that every quasiperiodic orbit comes arbitrary close to the vertex. However, as the angle is of the type π/n , the dynamics is not singular and the tori may cross \mathcal{S} . Varying slightly β_R , the pre-images become true singularities that can not be crossed anymore. If we increase β_R , the system becomes ergodic and \mathcal{S} still fills densely the whole phase space. In this case, there is nothing to learn from \mathcal{S} , since the mechanism of expansion prevails on the partitioning. If we decrease β_R , the pre-images of \mathcal{S}_0 are not dense anymore (see Fig. 2.5). They leave small regions where the tori seem to be confined. In Fig. 2.6 we represent a stochastic trajectory wandering around regions foliated in tori. The region of phase space occupied by the stochastic component corresponds to the set of pre-images. The integrable structure (orbits of the integrable half wedge are horizontal lines in this representation) is completely lost, and the global organization of phase space seems to be partially ruled by the singularities.

When $\beta = \pi/n$ with $n > 4$, the dynamics around the corner is C^0 or C^1 depending on the oddity of n . Thus the invariant sets which may cross S are then also C^0 or C^1 . Considering this low degree of differentiability one may wonder whether the sets do really have an intersection (see Fig. 2.4). Moreover, it is difficult on a Poincaré section to distinguish true tori from chains of very flat tori or from very thin bands of stochastic motion (see Fig. 2.4). Thus the existence and the exact nature of these sets remains very unclear.

3. Quantum Mechanics

3.1 Preliminary

This chapter concerns the quantum mechanics of the wedge billiard. As in the classical case, we start our analysis with a description of the one dimensional bouncer, from which we deduce the solutions of the integrable wedges. This is the only case for which we can write down explicitly the eigenenergies and eigenfunctions.

For the other values of the parameter, the system is not separable and may not be reduced to the one dimensional case. In the next section we adapt the scattering approach to quantization developed by Doron and Smilansky for Euclidean billiards to Hamiltonian systems in two dimensions with binding potential. Recently, Eckmann and Pillet [EP1, EP2] have proven a theorem that puts one of the versions of the scattering approach on a rigorous foundation. Moreover, it proved to be a very convenient starting point for both analytical [Sm, DS1, Gu1] and numerical [DS2, ScS] investigations. We show that our system admits a solution whenever the associated scattering matrix has an eigenvalue one, and we explain how the eigenfunction may be determined.

In the subsequent section, we apply the scattering method to the wedge billiard. This model may be considered as intermediate between Hamiltonian systems of the above type and Euclidean billiards. Moreover, we can check explicitly that this method yields the correct solutions on the integrable cases.

Next we present a short review of some semiclassical techniques, in order to obtain a semiclassical approximation to the scattering matrix. This latter will play a major role in the investigation of the correspondences between classical and quantum systems.

The expression of semiclassical scattering matrix associated to the integrable wedge billiard is derived in the following section. It yields a semiclassical expression for the energy density which is in complete agreement with the one derived by Berry and Tabor starting from EBK quantization [BT2].

3.2 Quantum Billiard System

It is well known that there is no unique rule for ascribing a quantum Hamiltonian to a known classical system, mainly because of the commutation relation of the operators \hat{p} and \hat{q} . However, the inverse problem is perfectly well defined: to a given Hamiltonian $\hat{H}(\hat{p}, \hat{q})$, function of the operators \hat{p} and \hat{q} , simply corresponds the classical Hamiltonian $H(\mathbf{p}, \mathbf{q})$, function of the variables \mathbf{p} and \mathbf{q} .

Here we will consider the simplest quantum Hamiltonian admitting (1.1) as a classical limit, namely

$$\hat{H} = \frac{\hat{p}_x^2}{2m} + \frac{\hat{p}_y^2}{2m} + mg\hat{y}. \quad (3.1)$$

We are looking for the square integrable solutions $\Psi(x, y)$ of the stationary Schrödinger equation $\hat{H}\Psi = E\Psi$ in configuration representation

$$\left[-\frac{\hbar^2}{2m}\Delta + mgy - E \right] \Psi(x, y) = 0 \quad (3.2)$$

with Dirichlet boundary condition on the sides $y = -\cot(\beta_L)x$ and $y = \cot(\beta_R)x$ of the wedge (see Fig. 1.1). As this problem may only be solved analytically for the integrable cases, we start our investigations with the quantum version of the one dimensional bouncer from which we will derive the two dimensional integrable solutions.

3.2.1 One Dimensional Quantum Bouncer

We consider the quantum Hamiltonian $\hat{H} = \frac{\hat{p}_y^2}{2m} + mg\hat{y}$ of a one dimensional quantum particle confined between a hard wall and a gravitational potential. Here we keep the original units, since we will have to take various values of the gravitation constant when considering the projections of the two dimensional system. The associated differential equation and boundary condition for the wave function $\eta(y)$ in configuration representation reads

$$\begin{aligned} \frac{d^2\eta}{dy^2} + \frac{2m^2g}{\hbar^2} \left(\frac{E}{mg} - y \right) \eta &= 0 & \text{if } y > 0 \\ \eta &= 0 & \text{if } y \leq 0. \end{aligned} \quad (3.3)$$

Using the variable substitution $z = \left(\frac{2m^2g}{\hbar^2} \right)^{1/3} \left(y - \frac{E}{mg} \right)$, the differential equation transforms into (see [LL2])

$$\frac{d^2\eta}{dz^2} - z\eta = 0. \quad (3.4)$$

As a second order differential equation, this latter admits two linear independent solutions $\text{Ai}(z)$ and $\text{Bi}(z)$ which are called *Airy Functions*. The wave function must be bounded for $y \rightarrow +\infty$, thus $\text{Bi}(z)$ has to be excluded. The solutions take then the form

$$\eta(y) = K \text{Ai} \left[\left(\frac{2m^2g}{\hbar^2} \right)^{1/3} \left(y - \frac{E}{mg} \right) \right], \quad (3.5)$$

with K the normalization constant. Setting $\eta(0) = 0$ quantizes the energy, which then takes the values

$$E_n = - \left(\frac{2m^2g}{\hbar^2} \right)^{-1/3} mgz_n \quad \text{for } n \in \mathbb{N}^* \quad (3.6)$$

where z_n is the n th zero of $\text{Ai}(z)$. Using the property $\text{Ai}''(z) = z\text{Ai}(z)$, we can compute the normalization constant K_n

$$\begin{aligned} \|\eta_n\|^2 &= K_n^2 \left(\frac{2m^2g}{\hbar^2} \right)^{-1/3} \int_{z_n}^{\infty} \text{Ai}^2(z) dz \\ &= K_n^2 \left(\frac{2m^2g}{\hbar^2} \right)^{-1/3} \left[z\text{Ai}^2(z) - \text{Ai}'^2(z) \right]_{z_n}^{\infty} \\ &= K_n^2 \left(\frac{2m^2g}{\hbar^2} \right)^{-1/3} \text{Ai}'^2(z_n). \end{aligned} \quad (3.7)$$

Thus, the orthonormal set of eigenfunctions reads

$$\eta_n(y) = \left(\frac{2m^2g}{\hbar^2} \right)^{1/6} \frac{1}{\text{Ai}'(z_n)} \text{Ai} \left[\left(\frac{2m^2g}{\hbar^2} \right)^{1/3} \left(x - \frac{E_n}{mg} \right) \right] \quad \text{for } n \in \mathbb{N}^*. \quad (3.8)$$

3.2.2 EBK Quantization

The Einstein-Brillouin-Keller (EBK) theory concerns the quantization of integrable systems. In a first step, one quantizes the actions of a d dimensional system, setting

$$\mathbf{I} = \frac{1}{2\pi} \oint \mathbf{p} d\mathbf{q} = \hbar(\mathbf{n} + \boldsymbol{\nu}/4) \quad (3.9)$$

where the integrals have to be taken on irreducible circuits γ and the vectors $\mathbf{n}, \boldsymbol{\nu} \in \mathbb{N}^d$. It was Einstein who extended the Bohr-Sommerfeld quantization condition to integrable but non-separable systems. Brillouin showed that this condition was a consequence of the single-valuedness of the wave function. The correction $\boldsymbol{\nu}$, which originates from the caustics, is Keller's contribution to the theory.

The energy spectrum of the system is then given explicitly by the equation

$$E_{\mathbf{n}} = H[\mathbf{I}] = H[\hbar(\mathbf{n} + \nu/4)] \quad (3.10)$$

so that the quantized energies correspond to the level surfaces of the Hamiltonian which touch some point of the lattice of the quantized actions (3.9). Each energy level is not associated to a single orbit, but to a family of orbits with irreducible action \mathbf{I} . This quantization condition clearly relies on the possibility of writing the Hamiltonian as a function of the actions only, i.e. on the existence of invariant tori.

As one dimensional Hamiltonian systems are integrable, one can always apply the above scheme to determine the quantized energy levels in the semiclassical limit, where (3.10) is expected to give the best results. For the one dimensional bouncer, we obtain

$$E_n = \left[\frac{3\pi\hbar\sqrt{mg}}{2\sqrt{2}} \left(n + \frac{3}{4} \right) \right]^{2/3}. \quad (3.11)$$

The number ν corresponds to the sum of the phase shifts that one has to add to the semiclassical wave function for each fold ($\nu_{\text{fold}} = 1$) and each hard wall ($\nu_{\text{wall}} = 2$) encountered on the circuit γ [CRL], so that $\nu = 3$ for the one dimensional bouncer (see Fig. 1.4). We can check the precision of this approximation, using an asymptotic series for the zeroes of the Airy function [AS]. For large n , we obtain

$$E_n = - \left(\frac{2m^2g}{\hbar^2} \right)^{-1/3} mgz_n \approx \left[\frac{3\pi\hbar\sqrt{mg}}{2\sqrt{2}} \left(n - \frac{1}{4} \right) \right]^{2/3} \left[1 + O(n^{-2}) \right]. \quad (3.12)$$

which is in complete agreement with the EBK result, since the index ν is determined modulo 4.

3.2.3 Integrable Wedges

As in classical mechanics, it is straightforward to compute the solutions of the square wedge ($\beta_R + \beta_L = \pi/2$ and $\beta_{R,L} \neq 0$) from the solutions of the one dimensional bouncer. Since the system is separable in the rotated coordinates $\tilde{x}\tilde{y}$ (see Fig. 1.5), the eigenfunctions are simply products of the one dimensional eigenfunctions with the corresponding gravitation constants $g_{\tilde{x}} = gc$ and $g_{\tilde{y}} = gs$ (recall $c = \cos \beta_R$ and $s = \sin \beta_R$). Using units¹ where $m = g = \hbar = 1$, we get

$$\begin{aligned} \Psi_{nl}(\tilde{x}, \tilde{y}) &= \eta_n(\tilde{x})|_{g_{\tilde{x}}=c} \eta_l(\tilde{y})|_{g_{\tilde{y}}=s} \\ &= K_{nl} \text{Ai} \left[(2c)^{1/3} \tilde{x} + z_n \right] \text{Ai} \left[(2s)^{1/3} \tilde{y} + z_l \right] \quad \forall n, l \in \mathbb{N}^* \end{aligned} \quad (3.13)$$

where $K_{nl} = (4cs)^{1/6} (\text{Ai}'[z_n] \text{Ai}'[z_l])^{-1}$ is the normalization constant. The related eigenenergies read

¹Setting $\hbar = 1$ corresponds to measuring the actions in units of the fundamental action $m_e a_0^2 \omega$ of the electron in the ground state of the Hydrogen atom.

$$E_{nl} = -2^{-1/3}(c^{2/3}z_n + s^{2/3}z_l). \quad (3.14)$$

When $\beta_R = \beta_L = \pi/4$, the eigenenergies simplify into

$$E_{nl} = -2^{-2/3}(z_n + z_l). \quad (3.15)$$

As this expression is symmetric in n and l , the energies are degenerated for $n \neq l$. We can make use of this symmetry to construct the solutions of the integrable half wedge ($\beta_R = \pi/4, \beta_L = 0$) which are the antisymmetric combinations of the degenerated eigenfunctions. They read

$$\begin{aligned} \Psi_{nl}(\tilde{x}, \tilde{y}) &= [\eta_n(\tilde{x})\eta_l(\tilde{y}) - \eta_n(\tilde{x})\eta_l(\tilde{y})]_{g=2^{-1/2}} \\ &= K_{nl} \text{Ai} [2^{1/6}\tilde{x} + z_n] \text{Ai} [2^{1/6}\tilde{y} + z_l] \quad \forall n > l \in \mathbb{N}^* \end{aligned} \quad (3.16)$$

with $K_{nl} = 2^{1/6}(\text{Ai}'[z_n]\text{Ai}'[z_l])^{-1}$, and clearly vanish on the vertical side, whereas the symmetric ones do not. Considering $n > l$ corresponds to taking half the space of the quantized actions of the symmetric wedge.

The integrable open wedges have continuous spectrum, since their phase space is not bounded. We will not treat them here. However, this property will be useful later in determining the eigenvalues and eigenfunctions of the wedges with bounded phase space.

3.3 Scattering Approach to Quantization

The purpose of this section is to show that the scattering approach for quantization [DoS], which has been used exclusively to quantize Euclidean billiards till now, can be extended quite easily to other systems with Hamiltonians of the form

$$H(\mathbf{p}, \mathbf{q}) = \frac{\mathbf{p}^2}{2m} + V(\mathbf{q}), \quad (3.17)$$

where it is assumed that $V(\mathbf{q}) \rightarrow \infty$ for $|\mathbf{q}| \rightarrow \infty$, so that motion is bounded by the potential.

Here we want to determine the square integrable solutions $\Psi(x, y)$ of the stationary Schrödinger equation (setting $m = \hbar = 1$)

$$\left[-\frac{1}{2}\Delta + V(x, y) - E \right] \Psi(x, y) = 0 \quad (3.18)$$

on \mathbb{R}^2 . To solve this problem, we shall show how one can construct two auxiliary scattering systems, in terms of which quantization is achieved.

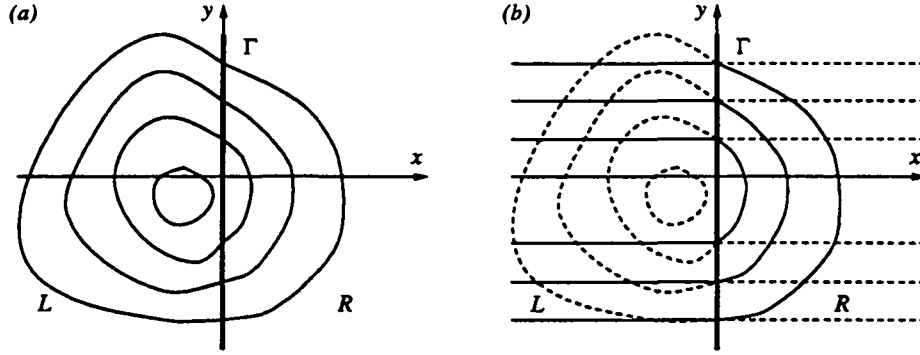


Fig. 3.1. (a) Equipotential lines of the original Hamiltonian system. The section Γ is taken on the vertical axis. (b) Equipotential lines of the right (solid lines) and left (dashed lines) scattering systems.

First, we take a straight line Γ in the xy plane. The method applies for an arbitrary Γ , but a sensible choice of the section will reduce the error of the semiclassical approximation. Performing an appropriate rotation of the coordinate system, we can always assume that Γ lies on the y axis. Thus, it separates the original system into two independent left (L) and right (R) scattering systems. The R system is formed by the potential on the right side of Γ , and its constant continuation on the left side (see Fig. 3.1):

$$V_R(x, y) = \begin{cases} V(x, y) & \text{for } x \geq 0 \\ V(0, y) & \text{for } x \leq 0. \end{cases} \quad (3.19)$$

Hence motion in the y direction is bounded by the potential, whereas motion in the x direction is free for $x \leq 0$. The constant potential along the negative x axis forms a “waveguide” in which the scattering process is defined. Similarly, we define the L system using the left part of the original system. The corresponding waveguide runs along the positive x axis. The solutions of the R (L) scattering system are solutions of the stationary Schrödinger equation restricted to the left (right) side of the origin and the right (left) waveguide. In the asymptotic region $x \leq 0$ ($x \geq 0$), such solutions may be written

$$\psi_m^{R(L)}(x, y) = \sum_{l=1}^{\infty} \frac{1}{\sqrt{k_l}} \left[\delta_{ml} e^{\pm i k_l x} + S_{ml}^{R(L)} e^{\mp i k_l x} \right] \eta_l(y) \quad \forall m \in \mathbb{N}^*, \quad (3.20)$$

where the functions $\eta_l(y)$ are channel or mode eigenfunctions with eigenenergies E_l , and

$$k_l = \begin{cases} \sqrt{2(E - E_l)} & \text{for } E \geq E_l \\ i\sqrt{2(E_l - E)} & \text{for } E \leq E_l \end{cases} \quad \text{so that} \quad \frac{k_l^2}{2} + E_l = E. \quad (3.21)$$

The factor $1/\sqrt{k_l}$ is a standard normalization yielding unit flux (see appendix A.2). The channel eigenfunctions η_l verify the 1 dimensional Schrödinger equation on Γ :

$$\left[-\frac{1}{2} \frac{\partial^2}{\partial y^2} + V(0, y) - E_l \right] \eta_l(y) = 0. \quad (3.22)$$

As the potential is binding, the energy spectrum is discrete. The η_l 's provide an orthonormal basis of the Hilbert space of the 1 dimensional problem. The waveguides are the same for the R and L problems. Note that when the exact solutions of (3.22) are not known analytically, one can still solve it in the WKB approximation, in order to get a quantization condition which holds in the semiclassical regime.

A channel l for which $k_l \in \mathbb{R}^+$ is called *open* and the corresponding modes *traveling*, since $e^{\pm ik_l x}$ represents propagating wave functions. When $k_l \in i\mathbb{R}^+$, $e^{\pm ik_l x}$ is an increasing or decreasing exponential function. In that case, one says that the channel l is *closed* and the mode *evanescent*. For potentials bounded from below, the number $\Lambda(E)$ of open channels at fixed energy E is finite, whereas the number of closed channels is infinite. The functions $e^{ik_l x} \eta_l(y)$ stand for wave functions traveling from $x = -\infty$ into the scattering system. We will call them *incoming modes*. Similarly, the functions $e^{-ik_l x} \eta_l(y)$ will be referred as *outgoing modes*. Thus, for $m \leq \Lambda$, the function ψ_m^R represents a wave of energy E propagating from the left in the incoming open channel m , scattering against the right part of the potential and reemitted with amplitude S_{ml}^R in the various open and closed channels l . The wave functions with $m > \Lambda$ do not correspond to propagating modes. They are usually neglected in the semiclassical approximation, since their contributions decrease exponentially in the asymptotic domain. Here we have to consider them, since the wave function is expanded on a complete basis on Γ .

We shall use the scattering functions ψ_m^R and ψ_m^L to construct an eigenfunction of the original Hamiltonian. As Ψ has to satisfy the Schrödinger equation on the R and L sides of Γ , a good ansatz is a function defined by a linear combination of the ψ_m^R in the region $x \geq 0$, and a linear combination of the ψ_m^L in the region $x \leq 0$. Such a function does not exist for arbitrary value of the energy, since the wave functions of both decompositions and their normal derivatives (with respect to Γ) have to match at $x = 0$. Actually, this matching is the quantization condition. For this purpose we have to find two sets of coefficients a_m^R and a_m^L , $m \in \mathbb{N}^*$, such that

$$\Psi(x, y) = \begin{cases} \sum_{m=1}^{\infty} a_m^R \psi_m^R(x, y) & \text{for } x \leq 0 \\ \sum_{m=1}^{\infty} a_m^L \psi_m^L(x, y) & \text{for } x \geq 0 \end{cases} \quad (3.23)$$

and the values of both the R and the L decompositions of Ψ and $\partial_x \Psi$ have to be matched at $x = 0$. Using the orthonormality of the functions $\eta_l(y)$, this condition transforms into a system of linear equations

$$\begin{aligned}
\sum_{m=1}^{\infty} a_m^R \frac{1}{\sqrt{k_l}} [\delta_{ml} + S_{ml}^R] &= \sum_{m=1}^{\infty} a_m^L \frac{1}{\sqrt{k_l}} [\delta_{ml} + S_{ml}^L] \quad \forall l \in \mathbb{N}^* \\
i \sum_{m=1}^{\infty} a_m^R \sqrt{k_l} [\delta_{ml} - S_{ml}^R] &= i \sum_{m=1}^{\infty} a_m^L \sqrt{k_l} [-\delta_{ml} + S_{ml}^L] \quad \forall l \in \mathbb{N}^*
\end{aligned} \tag{3.24}$$

which is a set of homogeneous equations for the coefficients a^R and a^L . Using a matrix notation and remembering that scattering matrices are symmetric (see appendix A.2), we obtain the matching condition in the form

$$\begin{pmatrix} \mathbb{1} & -S^L \\ -S^R & \mathbb{1} \end{pmatrix} \begin{pmatrix} a^R \\ a^L \end{pmatrix} = 0 \tag{3.25}$$

which admits a non-trivial solution if and only if

$$\ker [\mathbb{1} - S(E)] \neq \emptyset \quad \text{with} \quad S(E) = S^L \cdot S^R. \tag{3.26}$$

Thus the system admits E as eigenenergy whenever $S(E)$ has an eigenvalue $+1$. Since each element of the kernel gives a different solution for the matching, the degeneracy simply corresponds to this number of elements. Furthermore, this quantization condition gives a constructive method to obtain not only the eigenenergies, but the wave function too. First, one has to look for a value of E such that (3.26) is satisfied. Then one solves (3.25) to obtain the coefficients of the decomposition (3.23).

For symmetrical systems, it is also possible to determine the parity of the wave function. Consider a system for which the section Γ is a symmetry line with:

$$V(x, y) = V(-x, y) \quad \forall x \in \mathbb{R}. \tag{3.27}$$

As both the R and the L scattering systems are identical, $S^R = S^L$. According to (3.26), the system admits an eigenfunction of energy E each time $S^L \cdot S^R$ has an eigenvalue $+1$. Thus the symmetric system will have eigenfunctions for each eigenvalue ± 1 of S^R . For this special case, the system (3.24) can be simplified and rewritten

$$\begin{aligned}
[\mathbb{1} + S^R] (a^R - a^L) &= 0 \\
[\mathbb{1} - S^R] (a^R + a^L) &= 0.
\end{aligned} \tag{3.28}$$

Assume $S^R(E)$ has an eigenvalue $+1$. The corresponding eigenvector $(a^R + a^L)$ must also satisfy the other equation of the system, so that $a^R = a^L$. From (3.23), one deduces that $\Psi(x, y) = \Psi(-x, y)$, i.e., that the corresponding wave function is symmetric. Similarly, the eigenvalues -1 of $S^R(E)$ lead to antisymmetric eigenfunctions verifying $\Psi(x, y) = -\Psi(-x, y)$.

A similar approach in terms of quantum propagators has been developed recently by T. Prosen (see [Pr]).

3.4 Exact Quantization of the Wedge Billiard

We shall apply the above scattering formalism to quantize the wedge billiard, which is a system considered as intermediate between billiards and potential problems of the type (3.17).

3.4.1 General Wedge

We take the section Γ directly on the y axis. The R system is formed by the right side of the wedge and the reflecting wall along the negative x axis [see Fig. 3.2(b)]. The motion in the y direction is bounded by the potential and the reflecting wall, whereas motion in the x direction is free. The combination of the reflecting wall and the linear potential forms the waveguide along the negative x axis. The L system is defined in the same way, using the left side of the wedge and a waveguide on the positive x axis. The channel eigenfunctions are the solutions of the one dimensional quantum bouncer (see section 3.2.1).

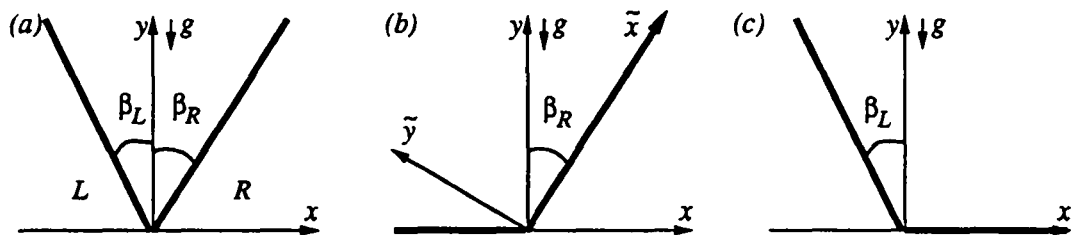


Fig. 3.2. Decomposition of the original wedge into two open wedges: (a) Original billiard system composed of two inclined sides. (b) The right scattering system (R) is composed of the right inclined side and a wave guide on the negative x axis. (c) The left scattering system (L) is composed of the left inclined side and a wave guide on the positive x axis.

To find the scattering matrix S^R of the right scattering system we will expand the wave functions ψ_m^R on another basis on the right side of the vertical axis, and use once again the matching condition at $x = 0$. In the domain $x \geq 0$, the right scattering system is separable when expressed in rotated coordinates $\tilde{x}\tilde{y}$ directed along the inclined boundary. Thus a natural basis is given by a product of two Airy functions vanishing at $\tilde{y} = 0$

$$\begin{aligned}
 \xi_r &= \text{Ai} \left[(2s)^{1/3} \tilde{y} + z_r \right] \text{Ai} \left[(2c)^{1/3} \tilde{x} - (2^{1/3} E + s^{2/3} z_r) c^{-2/3} \right] \\
 &= \text{Ai} \left[(2s)^{1/3} (-cx + sy) + z_r \right] \\
 &\quad \text{Ai} \left[(2c)^{1/3} (sx + cy) - (2^{1/3} E + s^{2/3} z_r) c^{-2/3} \right],
 \end{aligned} \tag{3.29}$$

where z_r ($r \in \mathbb{N}^*$) is the r 'th zero of the Airy function Ai . Each ψ_m^R can be expressed as a linear combination of the ξ_r 's

$$\psi_m^R(x, y) = \sum_{r=1}^{\infty} J_{mr} \xi_r(x, y) \quad (3.30)$$

and the matching condition between both decompositions of ψ_m^R at $x = 0$ reads

$$\begin{aligned} \sum_{l=1}^{\infty} \frac{1}{\sqrt{k_l}} [\delta_{ml} + S_{ml}^R] \eta_l(y) &= \sum_{r=1}^{\infty} J_{mr} \xi_r(0, y) \\ \sum_{l=1}^{\infty} i\sqrt{k_l} [\delta_{ml} - S_{ml}^R] \eta_l(y) &= \sum_{r=1}^{\infty} J_{mr} (\partial_x \xi_r)(0, y) \end{aligned} \quad (3.31)$$

where the coefficients S_{ml}^R and J_{mr} are the unknown. Multiplying by $\eta_n(y)$, integrating over y and using the orthonormality of the η_n 's, this transforms into

$$\begin{aligned} \delta_{mn} + S_{mn}^R &= \sum_{r=1}^{\infty} J_{mr} I_{rn}^1 \\ \delta_{mn} - S_{mn}^R &= \sum_{r=1}^{\infty} J_{mr} I_{rn}^2, \end{aligned} \quad (3.32)$$

where

$$\begin{aligned} I_{rn}^1 &= \sqrt{k_n} \int_0^{\infty} \xi_r(0, y) \eta_n(y) dy \\ I_{rn}^2 &= \frac{-i}{\sqrt{k_n}} \int_0^{\infty} (\partial_x \xi_r)(0, y) \eta_n(y) dy. \end{aligned} \quad (3.33)$$

Finally, system (3.32) can be simplified and rewritten in the following matrix form

$$\begin{aligned} S^R &= J \cdot I^- \\ \mathbb{1} &= J \cdot I^+ \end{aligned} \quad \text{with } I^{\pm} = \frac{1}{2} (I^1 \pm I^2). \quad (3.34)$$

Equation (3.34) does not assure that J is the inverse of I^+ , since both matrices are infinite dimensional. The scattering matrix S^L of the left scattering system is determined in the same way.

For systems with $\beta_L = \beta_R$, we have $S^L = S^R$ and the secular equation can be simplified. Using (3.32), we have

$$\begin{aligned} \det [\mathbb{1} + S^R] &= \det [J] \det [I^1] \\ \det [\mathbb{1} - S^R] &= \det [J] \det [I^2] \end{aligned} \quad (3.35)$$

and the problem reduces to finding the zeros of $\det [J]$, $\det [I^1]$ and $\det [I^2]$. Replacing (3.30) in (3.23) and permuting the sums, we obtain

$$\Psi(x, y) = \sum_{r=1}^{\infty} \left(\sum_{m=1}^{\infty} a_m^R J_{mr} \right) \xi_r(x, y), \quad (3.36)$$

so that an eigenvector of J^T with eigenvalue 0 (if it exists) would lead to an identically vanishing wave function. Hence it is enough to locate the solutions of the equations

$$\det [I^1(E)] = 0 \quad \text{and} \quad \det [I^2(E)] = 0. \quad (3.37)$$

Once an eigenenergy E_n has been found, the corresponding wave function then reads

$$\Psi(x, y) = \sum_{r=1}^{\infty} b_r \xi_r(x, y), \quad (3.38)$$

where b is the element of the kernel of $[I^1(E_n)]^T$ for antisymmetric eigenmodes or the element of the kernel of $[I^2(E_n)]^T$ for symmetric eigenmodes.

3.4.2 Integrable Symmetric Wedge

As a first illustration of this method, we apply it to the symmetric square wedge ($\beta_L = \beta_R = \pi/4$). Evaluation of the element $I_{mn}^1(E)$ at the eigenenergy $E = E_{ml}$ of the system [see (3.15)] gives

$$\begin{aligned} I_{mn}^1(E_{ml}) &= \sqrt{k_n} \int_0^{\infty} \text{Ai} [2^{-1/3}y + z_m] \text{Ai} [2^{-1/3}y - 2^{2/3}E_{ml} - z_m] \eta_n(y) dy \\ &= \sqrt{k_n} \int_0^{\infty} \text{Ai} [2^{-1/3}y + z_m] \text{Ai} [2^{-1/3}y + z_l] \eta_n(y) dy \\ &= I_{ln}^1(E_{ml}) \quad \forall n \in \mathbb{N}^*. \end{aligned} \quad (3.39)$$

Thus the m th and l th rows of $I^1(E_{ml})$ are identical. A similar computation of $I_{mn}^2(E)$ at $E = E_{ml}$ yields

$$I_{mn}^2(E_{ml}) = -I_{ln}^2(E_{ml}) \quad \forall n \in \mathbb{N}^* \quad (3.40)$$

which shows that the m th and l th rows of $I^2(E_{ml})$ differ only by a sign. As $I_{mn}^2(E_{mm}) = -I_{mn}^2(E_{mm}) = 0$ for all $n \in \mathbb{N}^*$, $\ker [I^2(E_{mm})] \neq \emptyset$. $S^R(E_{mm})$ has an eigenvalue +1 at $E = E_{mm}$ and the system admits a non-trivial symmetric solution

$$\left. \begin{array}{l} b_m \neq 0 \\ b_i = 0 \quad \text{for } i \neq m \end{array} \right\} \Rightarrow \Psi(x, y) = \xi_m(x, y), \quad (3.41)$$

as expected for this energy. For $m \neq l$, $\ker [I^2(E_{ml})] \neq \emptyset$ and $\ker [I^1(E_{ml})] \neq \emptyset$. Thus $S^R(E_{ml})$ has one eigenvalue +1 and another -1 at $E = E_{ml}$. The system of equations has two different non-trivial solutions

$$\left. \begin{array}{l} b_m = \pm b_l \\ b_i = 0 \quad \text{for } i \notin \{m, l\} \end{array} \right\} \Rightarrow \Psi(x, y) = \xi_m(x, y) \pm \xi_l(x, y) \quad (3.42)$$

and the energy level is degenerate. The solutions correspond respectively to a symmetric and an antisymmetric eigenmode of the billiard.

For the integrable half wedge ($\beta_L = 0$ and $\beta_R = \pi/4$), we have $S^L = -\mathbb{1}$. The secular equation transforms into $\det [\mathbb{1} + S^R] = 0$. Thus one has to consider only the above antisymmetric solutions vanishing on the vertical boundary.

3.4.3 Integrable Square Wedge

In order to achieve the discussion of the integrable wedge billiards we apply the scattering formalism to the square wedge billiard ($\beta_R + \beta_L = \pi/2$), assuming this time that the section $\tilde{\Gamma}$ is taken on the inclined side $\tilde{y} = 0$ (see Fig. 3.3).

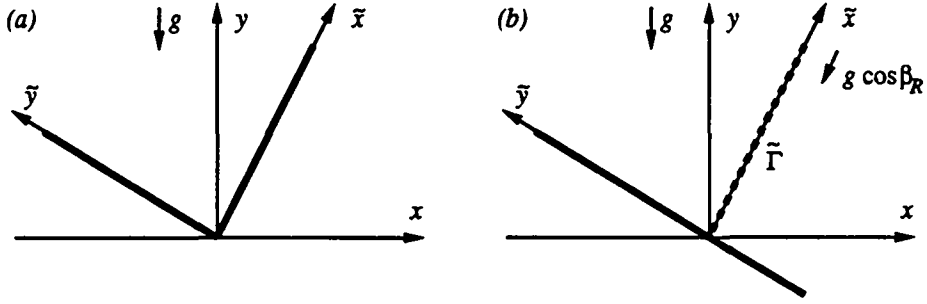


Fig. 3.3. (a) Square billiard system. (b) Decomposition of the original wedge into two scattering systems with the section $\tilde{\Gamma}$ on $\tilde{y} = 0$.

The potential in the waveguide is defined by the value of the original potential on the \tilde{x} axis. Hence it is also linear, but directed towards the \tilde{x} direction. The channel eigenfunctions $\tilde{\eta}_n(\tilde{x})$ and eigenenergies \tilde{E}_n correspond to the one dimensional quantum bouncer (see section 3.2.1) with $g = \cos(\beta_R)$. The scattering functions $\tilde{\psi}_m^R$ are decomposed on the basis

$$\tilde{\xi}_r = \text{Ai} \left[(2c)^{1/3} \tilde{x} + z_r \right] \text{Ai} \left[(2s)^{1/3} \tilde{y} - (2^{1/3} E + c^{2/3} z_r) s^{-2/3} \right] \quad (3.43)$$

with $r \in \mathbb{N}^*$. The matrix \tilde{S}^R is determined by the matching condition at $\tilde{y} = 0$ whereas $\tilde{S}^L = -\mathbb{1}$. As before, we compute the matrices

$$\begin{aligned} \tilde{I}_{rn}^1 &= \tilde{k}_n^{1/2} \int_0^\infty \tilde{\xi}_r(\tilde{x}, 0) \tilde{\eta}_n(\tilde{x}) d\tilde{x} = \tilde{k}_n^{1/2} \frac{\text{Ai}[f_r(E)] \text{Ai}'[z_r]}{(2c)^{1/6}} \delta_{rn} \\ \tilde{I}_{rn}^2 &= \frac{-i}{\tilde{k}_n^{1/2}} \int_0^\infty (\partial_{\tilde{y}} \tilde{\xi}_r)(\tilde{x}, 0) \tilde{\eta}_n(\tilde{x}) d\tilde{x} = \frac{-i}{\tilde{k}_n^{1/2}} \frac{(2s)^{1/3} \text{Ai}'[f_r(E)] \text{Ai}'[z_r]}{(2c)^{1/6}} \delta_{rn} \end{aligned} \quad (3.44)$$

with $f_r(E) = -(2^{1/3} E + c^{2/3} z_r) s^{-2/3}$ and $\tilde{k}_l(E)$ such that $\tilde{k}_l^2/2 + \tilde{E}_l = E$. The integrals are evaluated using the orthonormal properties of the $\tilde{\eta}_n$'s. Computation of $\tilde{I}_{mn}^1(E)$ at the eigenenergies $E_{ml} = -2^{-1/3}(c^{2/3} z_m + s^{2/3} z_l)$ yields

$$\tilde{I}_{mn}^1(E_{ml}) = 0 \quad \forall n \in \mathbb{N}^* \quad (3.45)$$

since

$$\text{Ai}[f_m(E_{ml})] = \text{Ai}[z_l] = 0. \quad (3.46)$$

Thus, the kernel of $[\tilde{I}^1(E_{ml})]^T$ admits the expected non-trivial solution

$$\left. \begin{array}{l} b_m \neq 0 \\ b_i = 0 \quad \text{for } i \neq m \end{array} \right\} \Rightarrow \Psi(x, y) = \tilde{\xi}_m(x, y). \quad (3.47)$$

As both the \tilde{I}^1 and \tilde{I}^2 are diagonal, we may immediately compute the exact S matrix in diagonal form, which reads

$$S_{mn}(E) = -\frac{[-f_m(E)]^{1/2} \text{Ai}[f_m(E)] + i \text{Ai}'[f_m(E)]}{[-f_m(E)]^{1/2} \text{Ai}[f_m(E)] - i \text{Ai}'[f_m(E)]} \delta_{mn}. \quad (3.48)$$

Using (3.46), it is then clear that the m th eigenvalue of $S(E_{ml})$ equals one. We can check that the restriction to the subspace of the $\tilde{\Lambda}$ open channels is unitary. When $m < \tilde{\Lambda}$, we have $|S_{mm}(E)| = 1$, since $f_m(E) < 0$. When $m > \tilde{\Lambda}$, we obtain $f_m(E) > 0$ and $0 < S_{mm}(E) < 1$. For $m \gg \tilde{\Lambda}$, we can use the asymptotic behavior of the Airy function to determine the decay rate of the elements. Here they do not decrease exponentially, as for instance in the case of a rectangular billiard, but like $1/m$. This slower decay may have some negative consequences in the numerical determination of eigenenergies in the general case.

Notice that though it would give the correct result, the choice Γ on $x = 0$ is inappropriate for this investigation. Thus, for symmetry reasons, it may be advantageous to take the section at different places.

3.5 Semiclassical Propagators

In this section we reintroduce the constant \hbar , since we want to discuss the semiclassical limit $\hbar \rightarrow 0$ (corresponding for billiards also to the limit $E \rightarrow \infty$).

The quantum mechanical transition amplitude between the state \mathbf{q}_1 at time t_1 and the state \mathbf{q}_2 at time t_2 of a d dimensional Hamiltonian system is the time propagator

$$K(\mathbf{q}_2, t_2; \mathbf{q}_1, t_1) = \langle \mathbf{q}_2 | \exp \left[-\frac{i}{\hbar} \hat{H}(t_2 - t_1) \right] | \mathbf{q}_1 \rangle. \quad (3.49)$$

According to Feynman's formulation of quantum mechanics [Fe], developed from an original idea by Dirac, the finite time propagator can be written as a path integral

$$\langle \mathbf{q}_2 | \exp \left[-\frac{i}{\hbar} \hat{H}(t_2 - t_1) \right] | \mathbf{q}_1 \rangle = \int_{(\mathbf{q}_1, t_1)}^{(\mathbf{q}_2, t_2)} d[\mathbf{q}(t)] \exp \left[\frac{i}{\hbar} \phi(\mathbf{q}(t)) \right] \quad (3.50)$$

involving purely classical quantities. This symbolic writing represents the sum over all possible paths (in configuration space) satisfying the boundary condition $\mathbf{q}(t_1) = \mathbf{q}_1$ and $\mathbf{q}(t_2) = \mathbf{q}_2$. Denoting L the Lagrangian of the system, the functional $\phi(\mathbf{q}(t))$ is defined with respect to the Lagrangian action

$$\phi(\mathbf{q}_2, t_2; \mathbf{q}_1, t_1) = \int_{t_1}^{t_2} dt L(\mathbf{q}(t), \dot{\mathbf{q}}(t)) \quad (3.51)$$

evaluated along all the possible paths (not necessarily physical) $\mathbf{q}(t)$. This formula only makes sense for finite time $t_2 - t_1$. This restriction comes from the nature of path integration where the original path has to be broken into a sum infinitesimal paths. It can be shown that (3.50) satisfies the Schrödinger equation [FH]. Moreover, this formula reflects two fundamental properties of quantum mechanics. Firstly, the superposition principle is verified, since (3.50) relates an amplitude of probability to a sum of amplitudes from the various paths. Secondly, the uncertainty principle is assumed because the paths are given by a boundary condition at both end, and not by an initial condition specifying space and momentum at the same time.

This formulation is very convenient when discussing semiclassical aspects of quantum mechanics. For $\hbar \ll 1$, the integrand of (3.50) is generally a very rapidly oscillating functional, so that the contribution of most of the paths $\mathbf{q}(t)$ are canceled by the ones of nearby paths $\mathbf{q}(t) + \delta\mathbf{q}(t)$. This mechanism of cancellation fails only when the paths $\mathbf{q}_\gamma(t)$ are such that

$$\delta\phi(\mathbf{q}_\gamma(t)) = \delta \int_{t_1}^{t_2} dt L(\mathbf{q}_\gamma(t), \dot{\mathbf{q}}_\gamma(t)) = 0. \quad (3.52)$$

Invoking Hamilton's principle, these paths $\mathbf{q}_\gamma(t)$ are the solutions of the classical equations of motion. Expanding the functional $\phi(\mathbf{q}(t))$ to second order around these classical trajectories, the stationary phase approximation to Feynman's propagator gives (see [Gul] equ. 10)

$$K(\mathbf{q}_2, t_2; \mathbf{q}_1, t_1) \simeq \sum_{\gamma} \left[\frac{\partial^2 \phi_{\gamma} / \partial \mathbf{q}_2 \partial \mathbf{q}_1}{(-2\pi i \hbar)^d} \right]^{1/2} \exp \left[\frac{i}{\hbar} \phi_{\gamma}(\mathbf{q}_2, t_2; \mathbf{q}_1, t_1) \right] \quad (3.53)$$

where ϕ_{γ} is the Lagrangian action evaluated along the corresponding classical path $\mathbf{q}_{\gamma}(t)$. This expression clearly mixes classical and quantal ideas. It is called semiclassical because it is a combination of classical dynamics and quantum superposition.

Another derivation is given by Miller [Mi], who shows the relation between canonical transformations of classical mechanics and unitary transformations of quantum mechanics. The assumption that for canonically conjugate variables \mathbf{p} and \mathbf{q}

$$\langle \mathbf{q} | \mathbf{p} \rangle = \left(\frac{1}{2\pi\hbar i} \right)^{d/2} \exp \left[\frac{i}{\hbar} \mathbf{q} \mathbf{p} \right] \quad \text{and} \quad \langle \mathbf{p} | \mathbf{q} \rangle = \left(\frac{-1}{2\pi\hbar i} \right)^{d/2} \exp \left[-\frac{i}{\hbar} \mathbf{p} \mathbf{q} \right], \quad (3.54)$$

is equivalent to requiring $[\hat{q}_m, \hat{p}_n] = i\hbar\delta_{mn}$, or to assuming the uncertainty principle. Evaluating transformations between two representations $(\mathbf{q}_1, \mathbf{p}_1)$ and $(\mathbf{q}_2, \mathbf{p}_2)$, such as

$$\langle \mathbf{q}_2 | \mathbf{q}_1 \rangle = \int d\mathbf{p}_1 \langle \mathbf{q}_2 | \mathbf{p}_1 \rangle \langle \mathbf{p}_1 | \mathbf{q}_1 \rangle \quad (3.55)$$

in stationary phase approximation², he can show that the classical limit of these transformations is obtained from the corresponding classical generating functions. In classical mechanics, there is a canonical transformation which describes the time evolution of coordinates and momenta according to the classical equations of motion: the dynamical transformation. As the classical generator of the transformation connecting (\mathbf{q}_2, t_2) to (\mathbf{q}_1, t_1) is the Lagrangian action, one directly gets (3.53). The generator relating (\mathbf{p}_2, t_2) to (\mathbf{p}_1, t_1) is the double Legendre transformation of the Lagrangian action $\bar{\phi}(\mathbf{q}_2, t_2; \mathbf{q}_1, t_1)$,

$$\bar{\phi}(\mathbf{p}_2, t_2; \mathbf{p}_1, t_1) = \phi(\mathbf{q}_2, t_2; \mathbf{q}_1, t_1) - \mathbf{p}_2 \mathbf{q}_2 + \mathbf{p}_1 \mathbf{q}_1 \quad (3.56)$$

with

$$\mathbf{q}_2 = -\frac{\partial \bar{\phi}}{\partial \mathbf{p}_2} \quad \text{and} \quad \mathbf{q}_1 = \frac{\partial \bar{\phi}}{\partial \mathbf{p}_1} \quad (3.57)$$

so that $\mathbf{q}_2 = \mathbf{q}_2(\mathbf{p}_2, t_2; \mathbf{p}_1, t_1)$ and $\mathbf{q}_1 = \mathbf{q}_1(\mathbf{p}_2, t_2; \mathbf{p}_1, t_1)$ are the classical coordinates of the trajectory with boundary condition $\mathbf{p}(t_1) = \mathbf{p}_1$ and $\mathbf{p}(t_2) = \mathbf{p}_2$. Replacing the Lagrangian L by the Hamiltonian H and integrating by parts, we obtain another useful expression for $\bar{\phi}$

$$\begin{aligned} \bar{\phi}(\mathbf{p}_2, t_2; \mathbf{p}_1, t_1) &= \int_{t_1}^{t_2} dt [\mathbf{p} \dot{\mathbf{q}} - H(\mathbf{p}, \mathbf{q})] - \mathbf{p}_2 \mathbf{q}_2 + \mathbf{p}_1 \mathbf{q}_1 \\ &= \int_{t_1}^{t_2} dt [-\dot{\mathbf{p}} \mathbf{q} - H(\mathbf{p}, \mathbf{q})]. \end{aligned} \quad (3.58)$$

The semiclassical approximation to the propagator in momentum representation then reads

$$K(\mathbf{p}_2, t_2; \mathbf{p}_1, t_1) \simeq \sum_{\gamma} \left[\frac{\partial^2 \bar{\phi}_{\gamma} / \partial \mathbf{p}_2 \partial \mathbf{p}_1}{(-2\pi i \hbar)^d} \right]^{1/2} \exp \left[\frac{i}{\hbar} \bar{\phi}_{\gamma}(\mathbf{p}_2, t_2; \mathbf{p}_1, t_1) \right] \quad (3.59)$$

where $\bar{\phi}_{\gamma}$ is the action evaluated along the classical trajectory γ .

²The dominant contribution to the integral $I = \int_{-\infty}^{\infty} dt g(t) \exp[if(t)/\hbar]$ (with $g(t)$ a slowly varying function of t) in the limit $\hbar \rightarrow 0$ is given by the contributions to the integral in the neighborhood of the stationary points. Let us assume that $\partial f / \partial t = 0$ at $t = t_0$. Then, expanding $f(t)$ to second order in t around t_0 and neglecting higher orders, we obtain the so called *stationary phase* or *saddle-point* approximation $I \approx g(t_0) \sqrt{(2\pi i \hbar) / f''(t_0)} \exp[if(t_0)/\hbar]$. This approximation may be generalized to integrals in higher dimensions.

Consider now the S matrix. The semiclassical expression for the S matrix may be obtained starting from the infinite time limit of the propagator in the interaction representation

$$S = \lim_{\substack{t_i \rightarrow -\infty \\ t_f \rightarrow +\infty}} \exp \left[\frac{i}{\hbar} H_0 t_f \right] \exp \left[-\frac{i}{\hbar} H(t_f - t_i) \right] \exp \left[-\frac{i}{\hbar} H_0 t_i \right] \quad (3.60)$$

where H_0 and H are the asymptotic and interaction Hamiltonians respectively. Classical asymptotic states of a d dimensional Hamiltonian system are characterized by $d - 1$ dimensional action variables \mathbf{I} , since the momentum p associated to the scattering direction is determined by energy conservation. The $d - 1$ conjugate angle variables will be denoted φ and the scattering coordinate q . We shall write $|p, \mathbf{I}\rangle$ the momentum eigenstate of H_0 with energy E . The on-shell S matrix elements in momentum representation are simply the matrix elements of the above S operator between initial and final momentum states. Thus, we obtain

$$S(E, \mathbf{I}_f, \mathbf{I}_i) = \exp \left[\frac{i}{\hbar} E(t_f - t_i) \right] \langle p_f, \mathbf{I}_f | \exp \left[-\frac{i}{\hbar} H(t_f - t_i) \right] | p_i, \mathbf{I}_i \rangle \quad (3.61)$$

where we used the fact that $\exp[iH_0 t/\hbar]|p, \mathbf{I}\rangle = \exp[iEt/\hbar]|p, \mathbf{I}\rangle$. In the semiclassical limit, we can replace the propagator by its semiclassical approximation. Thus, ignoring all pre-exponential factors (which may be determined in the end), we get

$$\begin{aligned} S(E, \mathbf{I}_f, \mathbf{I}_i) &\propto \lim_{\substack{t_i \rightarrow -\infty \\ t_f \rightarrow +\infty}} \exp \left[\frac{i}{\hbar} E(t_f - t_i) + \frac{i}{\hbar} \bar{\phi}(p_f, \mathbf{I}_f, t_f; p_i, \mathbf{I}_i, t_i) \right] \\ &\propto \exp \left[\frac{i}{\hbar} \bar{\Phi}(E, \mathbf{I}_f, \mathbf{I}_i) \right]. \end{aligned} \quad (3.62)$$

The new action $\bar{\Phi}$ is the Legendre transform of $\bar{\phi}$ with respect to the variables time $t = t_f - t_i$ and energy E , which are hence connected by the functional relation

$$E = E(p_f, \mathbf{I}_f, t_f; p_i, \mathbf{I}_i, t_i) = -\frac{\partial \bar{\phi}}{\partial (t_f - t_i)}. \quad (3.63)$$

Inserting expression (3.58) for $\bar{\phi}$, it is easy to verify that $\bar{\Phi}$ reads

$$\begin{aligned} \bar{\Phi}(E, \mathbf{I}_f, \mathbf{I}_i) &= \lim_{\substack{t_i \rightarrow -\infty \\ t_f \rightarrow +\infty}} \left\{ E(t_f - t_i) + \int_{t_i}^{t_f} dt \left(-\dot{p}q - \dot{\mathbf{I}}\varphi - H \right) \right\} \\ &= \int_{-\infty}^{\infty} dt \left(-\dot{p}q - \dot{\mathbf{I}}\varphi \right) \end{aligned} \quad (3.64)$$

and that it is well defined, since $\dot{p} \rightarrow 0$ and $\dot{\mathbf{I}} \rightarrow 0$ for $|t| \rightarrow \infty$. The pre-exponential factor is determined by requiring that the S matrix is unitary. A lengthy but straightforward computation yields the semiclassical approximation

$$S_{sc}(E, \mathbf{I}_f, \mathbf{I}_i) = \sum_{\gamma} \left[\frac{\partial^2 \bar{\Phi}_{\gamma} / \partial \mathbf{I}_f \partial \mathbf{I}_i}{(-2\pi i \hbar)^{d-1}} \right]^{1/2} \exp \left[\frac{i}{\hbar} \bar{\Phi}_{\gamma}(E, \mathbf{I}_f, \mathbf{I}_i) \right] \quad (3.65)$$

where the action $\bar{\Phi}_{\gamma}$ is evaluated along the various paths γ . It may be advantageous to use the S matrix in angle representation instead of momentum representation. Setting

$$\Phi(E, \varphi_f, \varphi_i) = \bar{\Phi}(E, \mathbf{I}_f, \mathbf{I}_i) + \mathbf{I}_f \varphi_f - \mathbf{I}_i \varphi_i \quad (3.66)$$

the inverse double Legendre transform of with

$$\mathbf{I}_i = -\frac{\partial \Phi}{\partial \varphi_i} \quad \text{and} \quad \mathbf{I}_f = \frac{\partial \Phi}{\partial \varphi_f}, \quad (3.67)$$

one obtains

$$S_{sc}(E, \varphi_f, \varphi_i) = \sum_{\gamma} \left[\frac{\partial^2 \Phi_{\gamma} / \partial \varphi_f \partial \varphi_i}{(-2\pi i \hbar)^{d-1}} \right]^{1/2} \exp \left[\frac{i}{\hbar} \Phi_{\gamma}(E, \varphi_f, \varphi_i) \right]. \quad (3.68)$$

This semiclassical approximation clearly fails at the conjugate points where an eigenvalue of the matrix $[\partial^2 \Phi / \partial \varphi_f \partial \varphi_i]^{-1}$ changes sign, since the value of the amplitude diverges. Nevertheless, it may be shown (by changing representation) that the approximation is still valid after crossing such points. One may also consider the absolute value of the determinant, in which case the phase has to be decreased by $\pi/2$ for each conjugate point. Collisions with hard walls also produce a change of phase in the wave function, so that one must add to the phase a factor $-\pi$ for each collision of the billiard. The resulting semiclassical formula then reads

$$S_{sc}(E, \varphi_f, \varphi_i) = \sum_{\gamma} \left[\frac{|\partial^2 \Phi_{\gamma} / \partial \varphi_f \partial \varphi_i|}{(-2\pi i \hbar)^{d-1}} \right]^{1/2} \exp \left[\frac{i}{\hbar} \Phi_{\gamma}(E, \varphi_f, \varphi_i) - i\nu_{\gamma} \frac{\pi}{2} \right] \quad (3.69)$$

where the index ν_{γ} is the Maslov index including the contributions from both the conjugate points and the hard walls encountered along the path γ .

3.6 Semiclassical Analysis

Starting from the scattering formalism, we will rederive the well known semiclassical trace formula for the density of states

$$d(E) = \sum_{n=1}^{\infty} \delta(E - E_n). \quad (3.70)$$

We show in appendix A.2 that S is unitary with respect to the subspace of open channels. We will denote S_{sq} the restriction of S with no evanescent modes, which

is the starting point of all the semiclassical theory based on scattering. It is called *semiquantal* approximation, because it neglects the modes which do not have a classical analogue. The matrix S_{sq} is a $\Lambda \times \Lambda$ matrix for which the quantization condition (3.26) may be written as the secular equation

$$Z_{sq}(E) = \det [\mathbb{1} - S_{sq}(E)] = 0. \quad (3.71)$$

The accuracy of this approximation will be discussed in the following chapter.

First we want to take advantage of the unitarity of $S_{sq}(E)$ to rewrite the semiquantal determinant (3.71) away from the threshold energies as a phase times an amplitude. Using the notation $e^{i\theta_l(E)}$ for the Λ eigenvalues of $S_{sq}(E)$, we may write

$$Z_{sq}(E) = \exp \left[\frac{i\Theta(E)}{2} \right] 2^\Lambda \prod_{l=1}^\Lambda \sin \left[\frac{\theta_l(E)}{2} \right], \quad (3.72)$$

where $\Theta(E) = \sum_{l=1}^\Lambda \theta_l(E) - \Lambda\pi$. The last product is real on the real energy axis. Therefore, the imaginary part of its logarithmic derivative, calculated at $E + i\epsilon$ in the limit $\epsilon \searrow 0$ is a sum of delta functions located at the eigenenergies. Using the expansion

$$\log \det [\mathbb{1} - S_{sq}(E)] = - \sum_{n=1}^{\infty} \frac{1}{n} \text{Tr} S_{sq}^n(E), \quad (3.73)$$

we obtain a semiquantal approximation for the exact density $d(E)$

$$d_{sq}(E) = \frac{1}{2\pi} \frac{\partial}{\partial E} \Theta(E) + \frac{1}{\pi} \lim_{\epsilon \rightarrow 0} \text{Im} \left[\sum_{n=1}^{\infty} \frac{1}{n} \frac{\partial}{\partial E} \text{Tr} S_{sq}^n(E + i\epsilon) \right]. \quad (3.74)$$

The first term on the rhs corresponds to the smooth part of the density. The Wigner delay time [GW] is defined as

$$\tau(E) = \text{Tr} \left[\frac{1}{i\Lambda} S_{sq}^\dagger(E) S'_{sq}(E) \right] = \frac{1}{\Lambda} \sum_{l=1}^\Lambda \theta'_l(E) \quad (3.75)$$

where the prime stands for differentiation with respect to E . Thus, this quantity characterizing the scattering is connected to the mean level density of the billiard via

$$d_{AV}(E) \approx \frac{1}{2\pi} \Theta'(E) = \frac{1}{2\pi} \sum_{l=1}^\Lambda \theta'_l(E) = \frac{\Lambda}{2\pi} \tau(E). \quad (3.76)$$

Integrating over E , we obtain an expression for the mean integrated density

$$N_{AV}(E) \approx \frac{1}{2\pi} \Theta(E) + \text{const} . \quad (3.77)$$

Because of the piecewise constant term $-\Lambda\pi$ in the definition of $\Theta(E)$, this expression with $\text{const}=0$ is valid over the whole range of energy. The second term on the rhs

represents the oscillatory part of the density $d_{osc}(E) = d(E) - d_{AV}(E)$. Notice that it only depends on the quantities $\text{Tr}S_{sq}^n(E)$ which play a major role in this formalism.

Up to this point we remained at the semiquantal level where all information comes from the quantum description of the system. The next step in the derivation of the semiclassical quantization is to express these quantities in terms of the periodic orbits of the corresponding classical system. Here it is important to remember that the scattering matrix is the quantum analogue of the Poincaré map on the matching line Γ [Ju]. Let us define conjugate action and angle variables (I, φ) on Γ . The Poincaré map is the classical transformation which maps the initial condition (I_i, φ_i) onto $(I_f, \varphi_f) = P(I_i, \varphi_i)$ corresponding to the next intersection of the classical trajectory with the section Γ . The classical dynamics may also be represented by the above generating function (or action) $\Phi(E, \varphi_i, \varphi_f)$ which depends on the energy as a parameter. The mapping is expressed explicitly as

$$I_i = -\frac{\partial\Phi}{\partial\varphi_i} \quad \text{and} \quad I_f = \frac{\partial\Phi}{\partial\varphi_f}. \quad (3.78)$$

The S matrix is the analogue of the classical mapping: it maps incoming scattering states onto outgoing scattering states of the system. We shall use this correspondence for wedges where the dynamics is either hyperbolic or integrable.

When the map is hyperbolic, the trace of the semiquantal scattering matrix (3.69) and of its powers can be approximated semiclassically by a sum over isolated periodic orbits [BS]

$$\text{Tr}S_{sq}^n(E) \approx \sum_{\{\gamma | n_\gamma r_\gamma = n\}} \frac{n_\gamma \exp[ir_\gamma \{\Phi_\gamma(E) - \nu_\gamma \pi/2\}]}{\sqrt{|\det[\mathbb{1} - (\partial P_\gamma)^{r_\gamma}]|}}, \quad (3.79)$$

where $\Phi_\gamma(E) = \sum_{j=1}^{n_\gamma} \Phi(E, \varphi_{j-1}, \varphi_j)$ is the action³ of the periodic orbit γ (setting $\varphi_{n_\gamma} = \varphi_0$). The quantity ν_γ stands for the Maslov index [CRL], and ∂P_γ is the monodromy matrix. The sum runs over all isolated primitive periodic orbits γ of the billiard which cross n_γ times the section Γ , and which satisfy $n_\gamma r_\gamma = n$, where r_γ is the number of repetitions. Due to this restriction, generally only a finite number of periodic orbits contribute to this sum for each value of n . Inserting (3.79) in (3.74), we obtain a semiclassical approximation for the spectral density in terms of the periodic orbits. Noting that the double sum over all integers n and over the orbits γ such that $n_\gamma r_\gamma = n$ may be replaced by a double sum over all orbits and their repetitions r , we finally get

$$d(E) \approx d_{AV}(E) + \text{Re} \left[\sum_\gamma \sum_{r=1}^{\infty} \frac{T_\gamma(E)}{\pi} \frac{\exp[ir \{\Phi_\gamma(E) - \nu_\gamma \pi/2\}]}{\sqrt{|\det[\mathbb{1} - (\partial P_\gamma)^r]|}} \right], \quad (3.80)$$

³For periodic orbits, the action $\Phi_\gamma(E) = \oint_\gamma \mathbf{q}(E) \cdot \mathbf{p}$ is equivalent to the action $\phi_\gamma = \oint_\gamma \mathbf{p}(E) \cdot \mathbf{dq}$. The constant term resulting from partial integration vanishes because of the periodicity of the orbit.

where $T_\gamma(E) = \frac{\partial}{\partial E} \Phi_\gamma(E)$ stands for the period of the orbit γ . This formula is known as the *Gutzwiller Trace Formula* [Gu2]. The semiclassical approximation of the S matrix in the present context is identical to the semiclassical T operator which was introduced by Bogomonly [Bog] who derived it using different considerations.

We can also apply the scattering approach to integrable systems. The integrability implies $\Phi = \Phi(E, \varphi_f - \varphi_i)$, since then $I_f = I_i$. Depending whether the difference $\Delta\varphi = \varphi_f - \varphi_i$ is a rational multiple of 2π or not, the orbit will be periodic or quasiperiodic. The ratio $\rho = \frac{\Delta\varphi}{2\pi}$ is called the rotation number. The semiclassical approximation to the S matrix in the φ representation reads

$$S_{sc}(E, \varphi_i, \varphi_f) = \left[\frac{|\partial^2 \Phi / \partial \varphi_i \partial \varphi_f|}{-2\pi i} \right]^{-1/2} \exp \left[i \left\{ \Phi(E, \varphi_f - \varphi_i) - \nu \frac{\pi}{2} \right\} \right] \quad (3.81)$$

where ν is the associated Maslov index. From this expression, one gets the action representation by double Legendre transformation. Hence we obtain

$$S_{sc}(E, I_i, I_f) = \delta_{I_i, I_f} \exp \left[i \left\{ -\Delta\varphi(E, I_i) I_i + \Phi(E, \Delta\varphi(E, I_i)) - \nu \frac{\pi}{2} \right\} \right], \quad (3.82)$$

where the pre-exponential factor reduces to a Kronecker symbol. Actually, the channel quantum numbers resulting from the quantization along Γ are the integers $I_i - \nu/4$ and $I_f - \nu/4$ (recall $\hbar = 1$). We shall now use the matrix S_{sc} as an approximation of the matrix S_{sq} . As S_{sc} is diagonal in this representation, it is straightforward to compute the phase of $\det [-S_{sc}(E)]$ and obtain the averaged integrated density

$$\frac{1}{2\pi} \Theta(E) \approx \sum_I \left[-\frac{\Delta\varphi(E, I) I}{2\pi} + \frac{\Phi(E, \Delta\varphi(E, I))}{2\pi} - \frac{\nu}{4} \right] - \frac{\Lambda}{2}, \quad (3.83)$$

where we have set $I = I_i = I_f$. To evaluate $\text{Tr} S_{sq}^n(E)$, one can use Poisson formula

$$\sum_{l=-\infty}^{+\infty} g(l) = \int_{-\infty}^{+\infty} dl \sum_{m=-\infty}^{+\infty} \exp [2\pi i m l] g(l) \quad (3.84)$$

which introduces a new sum over integers m . The resulting integral is solved in the saddle-point approximation which selects the action \tilde{I} such that $\Delta\varphi(E, \tilde{I}) = 2\pi m/n$. Notice that the main contributions come from the rational or periodic tori, since $\rho(\tilde{I}) \in \mathbb{Q}$. Hence we get

$$\text{Tr} S_{sq}^n(E) \approx \sum_{m=-\infty}^{\infty} \left[\frac{-n}{2\pi} \frac{\partial \Delta\varphi}{\partial I} \right]_{I=\tilde{I}}^{-1/2} \exp \left[i \left\{ n\Phi \left(E, \frac{2\pi m}{n} \right) - \frac{(m+n)\nu\pi}{2} + \frac{\pi}{4} \right\} \right] \quad (3.85)$$

that we can now insert in (3.74) to obtain the semiclassical expression of the density of states.

We may check these formulas on the integrable wedge $\beta_R + \beta_L = \pi/2$, with the section \tilde{I} along the inclined side (see subsection 3.2.1). As this system is separable

in the rotated coordinates, the rotation number is given by the ratio of the periods $T_{\tilde{x}}$ and $T_{\tilde{y}}$. The Hamiltonian in action variables reads

$$H = H_{\tilde{x}} + H_{\tilde{y}} = \left(\frac{3\pi c}{2\sqrt{2}} I_{\tilde{x}} \right)^{2/3} + \left(\frac{3\pi s}{2\sqrt{2}} I_{\tilde{y}} \right)^{2/3}, \quad (3.86)$$

where $I_{\tilde{x}} = \frac{1}{2\pi} \oint p_{\tilde{x}} d\tilde{x}$ and $I_{\tilde{y}} = \frac{1}{2\pi} \oint p_{\tilde{y}} d\tilde{y}$. The periods $T_{\tilde{x}}$ and $T_{\tilde{y}}$ are easily computed from the corresponding actions $I_{\tilde{x}}$ and $I_{\tilde{y}}$. Setting $\alpha = \left(\frac{2\sqrt{2}}{3\pi} \right)^{2/3}$, we get

$$\Delta\varphi(E, I_{\tilde{x}}) = 2\pi \frac{c}{s} \left[\frac{E - E_{\tilde{x}}(E, I_{\tilde{x}})}{E_{\tilde{x}}(E, I_{\tilde{x}})} \right]^{1/2} = 2\pi \frac{c}{s} \left[\frac{\alpha c^{-2/3} E - I_{\tilde{x}}^{2/3}}{I_{\tilde{x}}^{2/3}} \right]^{1/2}. \quad (3.87)$$

Inverting this relation, one obtains the generating function of the Poincaré map on the inclined boundary $\tilde{y} = 0$:

$$\Phi(E, \Delta\varphi) = \int d(\Delta\varphi) I(E, \Delta\varphi) = \frac{2\pi \Delta\varphi (\alpha E)^{3/2}}{\sqrt{(2\pi c)^2 + (s\Delta\varphi)^2}}. \quad (3.88)$$

Replacing Φ from (3.88) in (3.82), we get

$$S_{sc}(E, I_i, I_f) = \delta_{I_i, I_f} \exp \left[i \left\{ 2\pi \frac{c}{s} \left(\alpha c^{-2/3} E - I_i^{3/2} \right)^{3/2} - \nu \frac{\pi}{2} \right\} \right] \quad (3.89)$$

when ν is undetermined. One could also compute this semiclassical limit starting from the exact S matrix (3.48), and introducing appropriate expansions for the Airy function. This derivation yields the same result, but also leads to the determination of the Maslov index ($\nu = 3$). The semiclassical integrated density then reads

$$N_{sq}(E) \approx \frac{c}{s} \sum_I \left(\alpha c^{-2/3} E - I^{2/3} \right)^{3/2} - \frac{(\nu + 2)\Lambda}{4} \approx \frac{E^3}{12\pi s c}, \quad (3.90)$$

as expected for this wedge. We may also evaluate semiclassically the trace of any power of S_{sq} , which gives

$$\begin{aligned} \text{Tr} S_{sq}^n(E) &\approx \sum_{m=-\infty}^{+\infty} \sqrt{\frac{3s (\alpha E)^{3/4} (nc)^{3/2} |ms|^{1/2}}{c (n^2 c^2 + m^2 s^2)^{5/4}}} \\ &\times \exp \left[2\pi i \left\{ \frac{(\alpha E)^{3/2} n m}{\sqrt{n^2 c^2 + m^2 s^2}} - \frac{(n+m)\nu}{4} + \frac{1}{8} \right\} \right]. \end{aligned} \quad (3.91)$$

Substituting this expression in the second term of the rhs of (3.74), we obtain a semiclassical approximation for the oscillatory part of the density. Regrouping the terms with positive and negative m , one obtains a real function for real energy, which reads

$$d_{osc}(E) \approx \sum_{n,m=1}^{\infty} \sqrt{\frac{3^3}{sc} \frac{1}{\alpha} \frac{(\alpha E)^{5/4} (nc)^{3/2} (ms)^{3/2}}{(n^2 c^2 + m^2 s^2)^{7/4}}} \times \cos \left[2\pi \left\{ \frac{(\alpha E)^{3/2} nm}{\sqrt{n^2 c^2 + m^2 s^2}} - \frac{(n+m)\nu}{4} + \frac{1}{8} \right\} \right]. \quad (3.92)$$

For integrable systems it is also possible to derive the Berry Tabor [BT1] semiclassical expression for $d(E)$ using EBK quantization. The EBK values for the actions are $I_1 = n_1 + \nu/4$ and $I_2 = n_2 + \nu/4$. Then, transforming both the sums into integrals using Poisson sum rule, the density reads

$$d(E) \approx \sum_{n_1, n_2=0}^{\infty} \delta \left(E - H \left[n_1 + \frac{\nu}{4}, n_2 + \frac{\nu}{4} \right] \right) \approx \int_0^{\infty} dI_1 dI_2 \sum_{m_1, m_2=-\infty}^{+\infty} \varphi_{m_1, m_2}(I_1, I_2) \delta(E - H[I_1, I_2]) \quad (3.93)$$

with

$$\varphi_{m_1, m_2}(I_1, I_2) = \exp \left[2\pi i m_1 \left(I_1 - \frac{\nu}{4} \right) + 2\pi i m_2 \left(I_2 - \frac{\nu}{4} \right) \right]. \quad (3.94)$$

The integration over dI_2 fixes $I_2 = I_2(E, I_1)$, and the one over dI_1 is solved in the saddle-point approximation. The term with $m_1 = m_2 = 0$ does not oscillate and hence gives the averaged density, for which we find $\frac{E^3}{12\pi sc}$, as before. Removing this part and regrouping the terms pairwise with respect to m_1 and m_2 , we obtain exactly the same double sum as in (3.92).

This check provides further support for the formalism based on scattering, since the starting point of both derivations are quite different. However the computations rely on the same methods. Except for one of the sums in (3.92) which comes from the expansion of the logarithm, the sums were generated by Poisson formula. In both cases, it is the saddle-point approximation which selects the contributions of the periodic tori with $\rho \in \mathbb{Q}$.

4. Numerical Results on Quantum Mechanics

4.1 Preliminary

We start this last chapter with some numerical checks of the quantization scheme developed in the previous chapter. We test the accuracy of the energy levels determined numerically and discuss the applicability of the method for higher energies.

Next we verify the Gutzwiller trace formula involving energy levels and periodic orbits. We also test semiclassical relations between the semiclassical S matrix and the periodic orbits, and comment on the deviations. In discussing the periodic orbits of the wedge, we draw a particular attention to the role played by the sets of special orbits described in the first chapter. We give a very simple rule for computing the Maslov index of a given periodic orbit.

In the subsequent section we provide illustrations of quantum propagation in the wedge billiard. First we show that the spreading of the wave function in phase space is much faster when the underlying classical dynamics is chaotic than when integrable. The second illustration concerns the quantum dynamics of a wave packet in the corner of the wedge, where the interference phenomenon is related to the evolution of a beam of classical trajectories.

We close this chapter with a detailed statistical investigation. This analysis is possible due to the efficiency of the scattering method which provides accurate data sets. The first statistical test concerns the distribution of energy levels in both integrable and chaotic cases. Next we show that the eigenphases of the scattering matrix associated to the wedge lead to an equivalent characterization of the system. Then we look at these quantities for a chaotic wedge when a parameter of the system is varied. We compute the “velocities” and “curvatures” (first and second derivatives of a quantity with respect to the parameter) and analyze the corresponding distributions which provide complementary information on the system. Notice that these distributions are now studied with applications to atomic and mesoscopic physics.

4.2 Checks of the Quantum Formalism

In this section we show how to implement the scattering method to determine energy levels and wave functions of half wedges. We also discuss the accuracy of these results and the efficiency of the method.

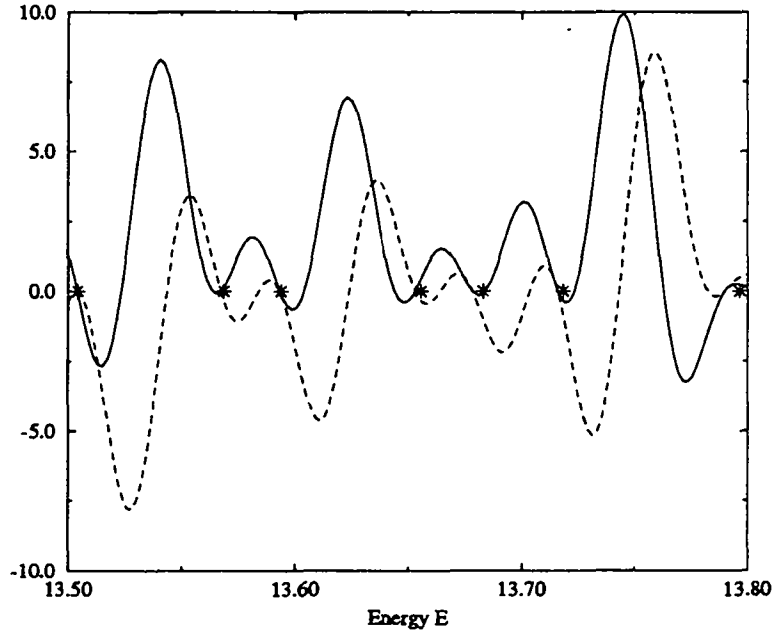


Fig. 4.1. Behavior of $\text{Re}\{\det[\mathbb{1} - S(E)]\}$ (solid line) and $\text{Im}\{\det[\mathbb{1} - S(E)]\}$ (dashed line) with no evanescent modes for the half wedge with $\beta_R = \pi/3$. The positions of the exact energy levels are marked with stars on the energy axis.

The S matrix is an infinite dimensional matrix. Only in the case $\beta_R = \pi/4$ it is possible to treat analytically the full S matrix. For other values of β_R , we have to consider restrictions of S with finite numbers of elements. The main problem in practical computations is to find the optimal restriction which will yield the required accuracy at the minimum computational effort. It is shown in appendix A.2 that S is unitary with respect to the subspace of open channels. They contain the most important part of the information, since they represent traveling modes which give the leading contribution to the semiclassical limit. Thus, we have to consider at least the restriction to the subspace of the open channels.

Figure 4.1 represents the behavior of the real and imaginary parts of $\det[\mathbb{1} - S(E)]$ for a truncation of the S matrix corresponding to the open modes only. The system admits an eigenenergy E whenever both real and imaginary parts vanish simultaneously. As both functions never vanish numerically for the very same value of E , one has to look for minima of $|\det[\mathbb{1} - S(E)]|$ close to zero. For the half wedge, we have seen that the eigenenergies are also given by the zeros of $\det[I^1(E)]$. The use

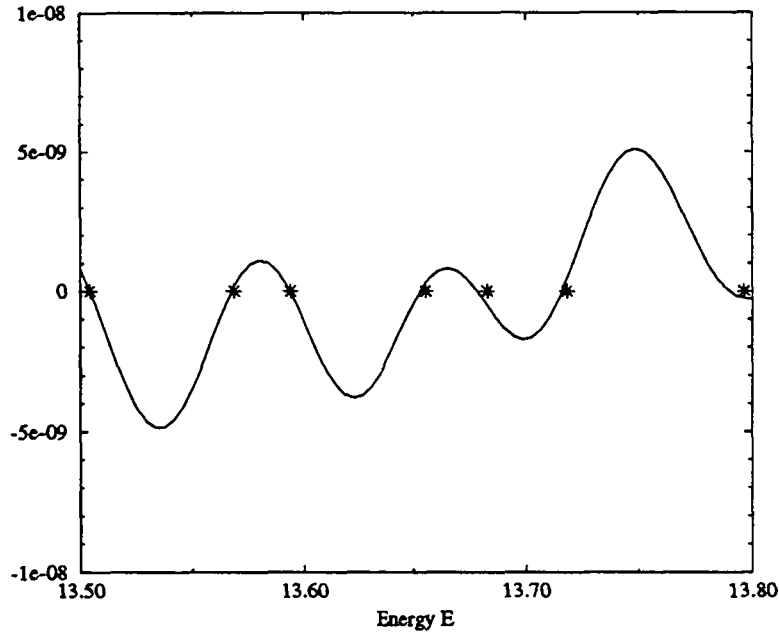


Fig. 4.2. Behavior of $\det[\text{Re}\{I^1(E)\}]$ for the half wedge with $\beta_R = \pi/3$, where the matrix I^1 has size $\Lambda \times \Lambda$. The positions of the exact energy levels are marked with stars on the energy axis.

of this formula spares the computation of the matrix $I^2(E)$ and the computation of the S matrix. Moreover, the imaginary part of the rows of $I^1(E)$ is collinear with the real part, so that one can reduce the computation of the eigenenergies to the determination of the zeros of the real function $\det[\text{Re}\{I^1(E)\}]$. In Fig. 4.2 we plot $\det[\text{Re}\{I^1(E)\}]$, where I^1 is restricted to the first Λ rows and columns¹. It should be noted that the kernels of the full matrices S and I^1 lead to the same energies and wave functions, but the truncations to the same number of elements yield slightly different approximations.

Unfortunately, truncating S to the subspace of open channels does not always give a good estimate, and may even lead to missing of some of the eigenvalues. This is well illustrated by the integrable case $\beta_L = 0$ and $\beta_R = \pi/4$ at $E = E_{mn}$ with $n = 1$. To see that the 1st and the m th row of I^1 are equal, the dimension of the restriction of S must be at least m . But due to the inclination of the boundary, we may have $m \simeq \Lambda / \sin(\beta_R)$. Hence it is necessary to include $\Lambda(\csc(\beta_R) - 1)$ evanescent modes to reproduce all levels of the integrable case. Such phenomenon might happen whenever both the $\psi_m^R(x, y)$ and the $\xi_r(x, y)$ basis do not have the same number of elements which contribute semiclassically. This clearly demonstrates the need of including some closed channels in the computations to obtain a precise and reliable spectrum. On the other hand, the size of the elements of S which involve closed channels

¹The integrals involving products of Airy functions are determined numerically using a Gauss-Laguerre algorithm. The precision of integration may be checked evaluating numerically the same integral after an analytic integration by parts.

decreases steadily at a rate which is slower than exponential. Hence including too many evanescent modes leads to numerical imprecision. However, as we have no analytical method to estimate the number of evanescent modes which guarantees a desired accuracy, we have to investigate this problem numerically.

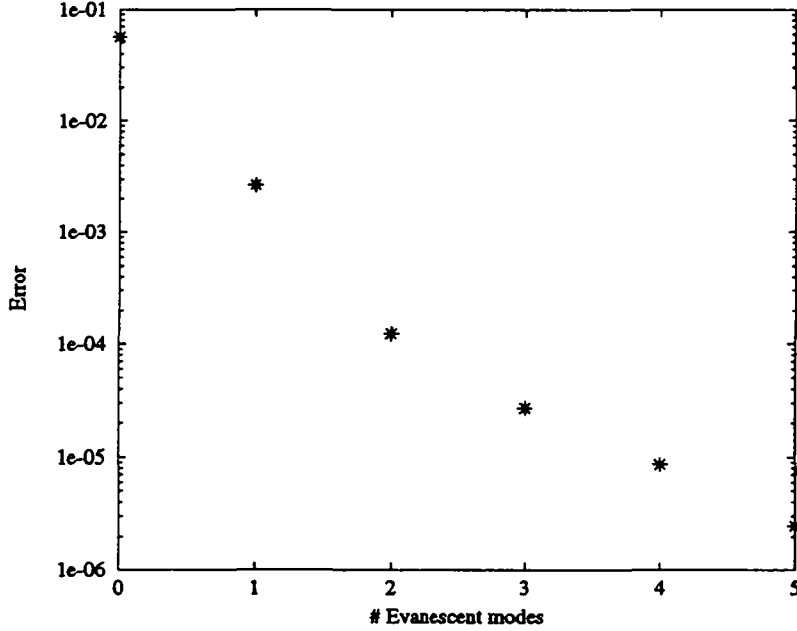


Fig. 4.3. Error in the position of the levels as a function of the number of evanescent modes for $\beta_L = 0$ and $\beta_R = \pi/3$. The error decreases exponentially with the number of evanescent modes.

In Fig. 4.3 we plot the mean error in the zeros of the secular equation as a function of the number of evanescent modes. The mean is taken over the 100 lowest eigenenergies for $\beta_R = \pi/3$, and the error is given in units of the mean level spacing. The gain in precision is higher when adding the first and second non-propagating modes. This might be a consequence of the difference between both decompositions of Ψ , as explained above. Although the number of points is small, the error seems to decrease exponentially when more than two channels are added. Thus the algorithm converges very rapidly when the number of closed channels is increased. In what follows, we assume that the values to which the zeros tend are the exact eigenenergies.

We have pointed out above that the truncation of the space of evanescent modes might lead to missing some eigenenergies. To check this point we studied the integrated density

$$N(E) = \sum_{n=1}^{\infty} \theta(E - E_n) \quad (4.1)$$

with θ the unit step function, and the fluctuations around the averaged value [SG3]

$$N_{AV}(E) = \frac{\tan(\beta_R)}{12\pi} E^3 - \frac{1 + \sec(\beta_R)}{3\sqrt{2}\pi} E^{3/2} + \frac{1}{6}, \quad (4.2)$$

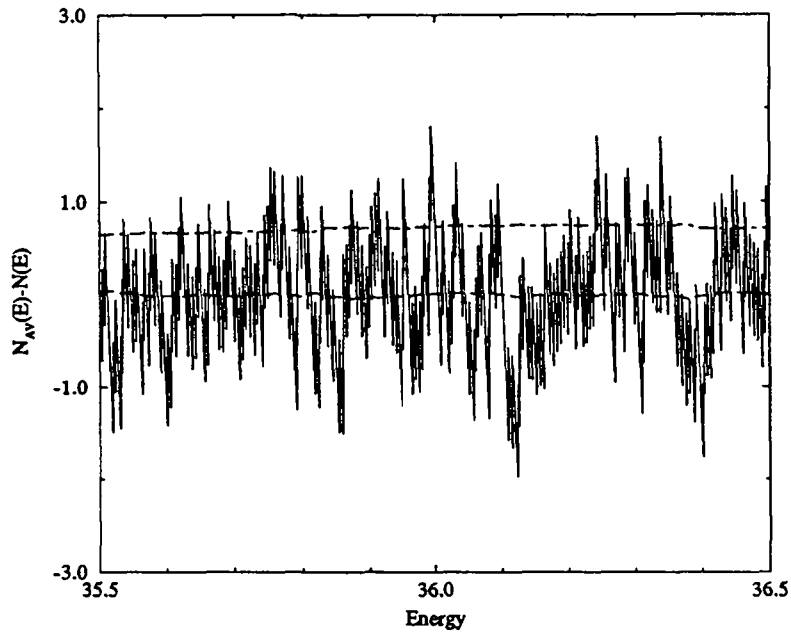


Fig. 4.4. Fluctuations of the exact density $N(E)$ around its averaged value $N_{AV}(E)$ for $\beta_L = 0$ and $\beta_R = \pi/3$. The dashed line indicates the running average over 200 values, and the dashed-dotted line the running standard deviation.

in which the constant term has been postulated to be the same as for billiards with smooth boundary in spite of the corner. The solid line in Fig. 4.4 represents a plot of the difference $N_{AV}(E) - N(E)$ for 200 levels starting at the 2000th eigenenergy when $\beta_R = \pi/3$. One expects this quantity to fluctuate around the number of missing levels. The dashed line is the corresponding running average over 200 values. Its small value shows that no level is missed, and seems to confirm the choice of the constant term $1/6$ in N_{AV} . The dashed-dotted line, which is the running standard deviation from the running average, reflects the strong rigidity of the spectrum, as expected for a chaotic system. The number of open modes $\Lambda(E)$ for large E may be approximated from (3.6) and the asymptotic behavior of z_n for large n [AS]. As the leading term of N_{AV} goes like E^3 , we obtain

$$\Lambda \sim E^{3/2} \sim \sqrt{N_{AV}}. \quad (4.3)$$

Thus the dimension of the restricted S increases only as the square root of the number of levels, which renders this algorithm efficient. For instance, $\Lambda = 45$ for the 1000th levels of a wedge with $\beta_R = \pi/3$. This allows the computation of relatively high energy levels.

We did not encounter any numerical difficulty in the determination of the first 3300 eigenenergies of the wedge with $\beta_R = \pi/3$. The time of computation is highly dependent on the ability of locating the next zero of $\det[I^1(E)]$. For energies of this order, computation of I^1 becomes time consuming, since one has to evaluate

Λ^2 integrals numerically. This is the only impediment which prevented us from extending the calculations for higher energies. However, the additional $\Lambda(\csc(\beta_R)-1)$ evanescent modes might be another source of numerical problems for much higher energies. The elements I_{rn}^1 tend to 0 for $n, r \rightarrow \infty$. Thus, if one considers too many evanescent modes, the determinant becomes numerically identical to zero.

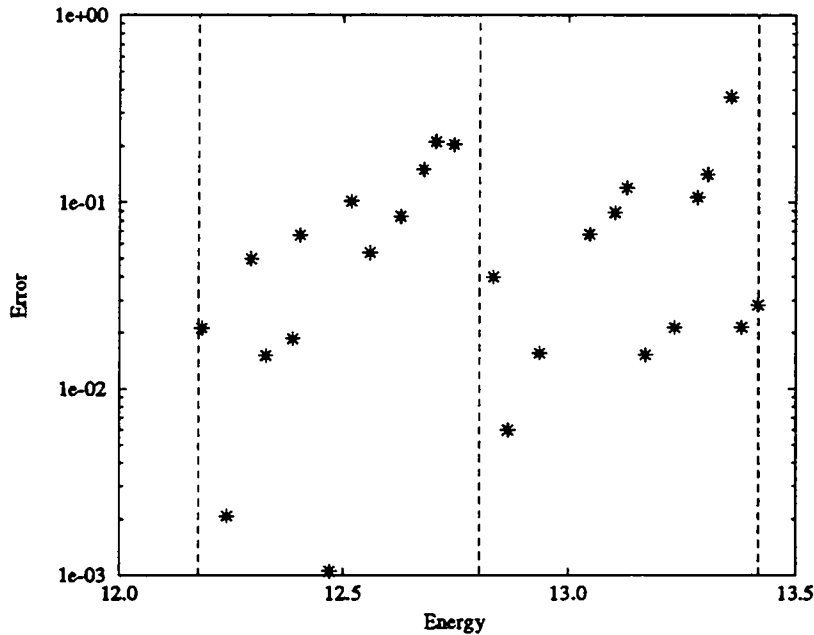


Fig. 4.5. Shift in the position of the zeros corresponding to the semiquantal approximation for $\beta_L = 0$ and $\beta_R = \pi/3$. The maximum is obtained just before the opening of a new channel.

Next we discuss the restriction S_{sq} with no evanescent modes and the secular equation (3.71). Figure 4.5 represents the shift in the position of all the zeros of the semiquantal approximation with 13 and 14 open channels for $\beta_R = \pi/3$. The error is measured with respect to the exact position of the levels in units of the mean levels spacing. The thresholds of the 13–15 channels are marked by dashed lines. Comparison with results obtained for other billiards with the same method [DoS, ScS] reveals that the error is some order of magnitude larger for the wedge billiard. This is mainly due to the corner made by the wave guide and the boundary at $x = 0$, because the evanescent modes are essential for the proper description of the wave function near such a singularity. This problem does not appear for the above mentioned billiards where the wave guides were chosen to match the boundary smoothly. However, one can see on this figure that the shift reaches its maximum just before the opening of a new channel, emphasizing the role played by the almost conducting mode. As mentioned above, a more serious drawback of the semiquantal approximation is that it might miss or add some eigenvalues. For instance, the secular equation for $\beta_R = \pi/3$ and $E \leq E_{300}$ cannot locate 10 (3.3%) of the eigenenergies and generates 6 (2%) irrelevant ones.

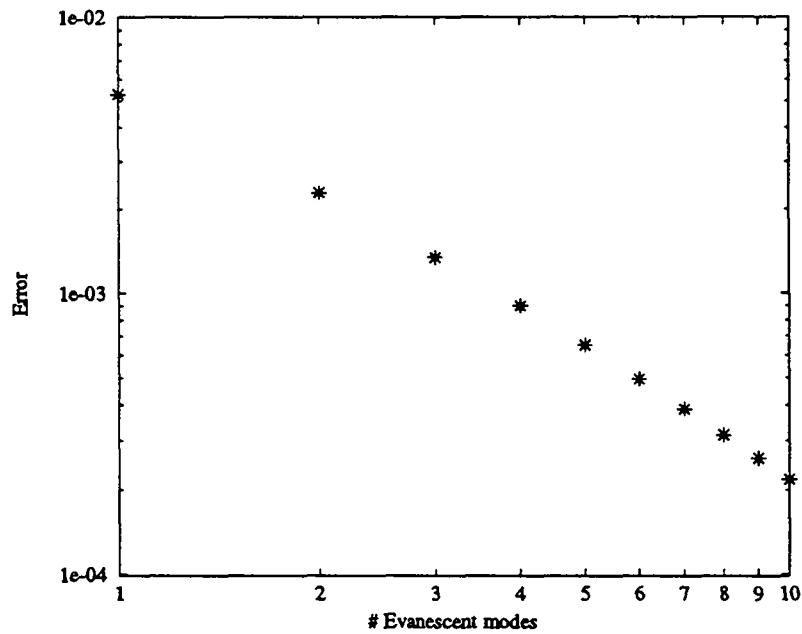


Fig. 4.6. Estimation of the error in the computation of the unitary part of the S matrix as a function of the number of evanescent modes for $\beta_L = 0$ and $\beta_R = \pi/3$. The error decreases in a power law with the number of evanescent modes.

Computation of the S matrix from (3.34) involves the inversion of a finite approximation of the matrix I^+ , which is a further source of numerical imprecision. The accuracy of the numerical S matrix can be verified with the help of the relations derived in appendix A.2. A reasonable estimate of the error is the mean over the difference $S_{oo} \cdot S_{oo}^\dagger - \mathbb{1}$, where S_{oo} represents the unitary part of S . We chose to verify the accuracy of S_{oo} , since this part is the relevant one for the semiclassical analysis. In Fig. 4.6 we plot the error in the unitary part of $S(E)$ as a function of the number of evanescent modes for $E = E_{10}$ at $\beta_R = \pi/3$. As one can see, the error only decreases as a power law in this case. Notice that $S_{oo} \cdot S_{oo}^* = \mathbb{1}$ is a symmetry which follows automatically from (3.34) and hence always satisfied.

4.3 Checks of the Semiclassical Analysis

In this section we discuss the applicability and the validity of the above semiclassical formula. In the numerical analysis we concentrate on the hyperbolic half wedge billiard ($\beta_L = 0$ and $\beta_R > \pi/4$).

First we consider the Gutzwiller trace formula (3.80). It is important to take this formula as an equation between distributions. As we cannot observe delta distributions numerically, it will be advantageous to apply these distributions on testfunctions.

Moreover, we have at our disposal only a finite number of eigenenergies. Testfunctions with strong decaying properties will be appropriate, because they will cancel the effect of the missing high eigenenergies. It has been shown that such a procedure with suitable testfunctions may even render the sum absolutely convergent [SS]. The price for this convergence is that the delta distributions transform into peaks of finite width. A more significant check is obtained when one considers a weighted Fourier transform of this equation. The peaks should then resolve the actions of the periodic orbits. It is interesting because in this way one can detect the existence of semiclassical contributions from other kind of orbits. Broadly speaking, (3.80) shows that the periodic orbits “know” about the eigenenergies of the quantum system. The Fourier transform tests how the quantum system “remembers” the periodic orbits. Such a representation is usually called length spectrum, for the actions of Euclidean billiard are proportional to the length of the orbits.

We have seen that the angle is the only parameter influencing the dynamics. Thus, the classical system scales with energy and we have $\Phi_\gamma(E) = \Phi_\gamma E^{3/2}$ where $\Phi_\gamma = \Phi_\gamma(1)$. With the help of the new variable $\kappa = E^{3/2}$, we define the transformation

$$D(x) = \int_0^\infty d\kappa \exp \left[- \left(\frac{\kappa - \kappa_o}{\Delta\kappa} \right)^2 \right] \cos [(\kappa - \kappa_o)x] d(\kappa). \quad (4.4)$$

Notice that this transformation is not invertible. As $d(\kappa)$ is known for $0 < \kappa < E_{max}^{3/2}$, we have to chose $\Delta\kappa$ and κ_o so that the testfunction almost vanishes out of this range.

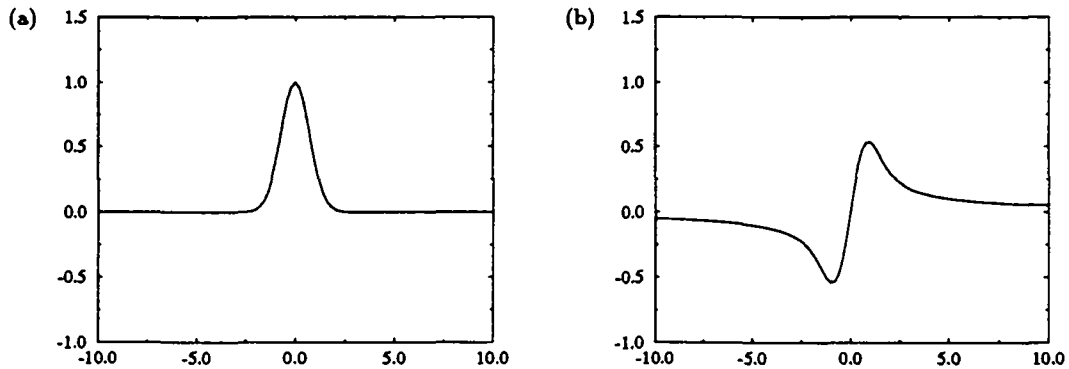


Fig. 4.7. Plots of the functions $f_c(z)$ (a) and $f_s(z)$ (b).

While the transform of the exact density of energy is straightforward and gives

$$D(x) = \sum_n \exp \left[- \left(\frac{\kappa_n - \kappa_o}{\Delta\kappa} \right)^2 \right] \cos [(\kappa_n - \kappa_o)x], \quad (4.5)$$

the transform of its semiclassical approximation can be computed analytically for $\kappa_o = 0$ and well approximated for $\kappa_o \gg \Delta\kappa$. For $\kappa_o = 0$, i.e., when most of the weight of the testfunction is put around $\kappa = 0$, we obtain

$$\begin{aligned}
D_{sc}(x)|_{\kappa_o=0} = & \frac{\tan(\beta_R)}{4\pi} \frac{(\Delta\kappa)^2}{3} \left[1 - \Delta\kappa x f_s\left(\frac{\Delta\kappa x}{2}\right) \right] - \frac{1 + \sec(\beta_R)}{2\sqrt{2}\pi} \frac{\Delta\kappa\sqrt{\pi}}{3} f_c\left(\frac{\Delta\kappa x}{2}\right) \\
& + \sum_{\gamma} \sum_{r=1}^{\infty} \frac{\Phi_{\gamma}}{\pi} \frac{1}{\sqrt{|\det[1 - (\partial P_{\gamma})^r]|}} \frac{\sqrt{\pi}\Delta\kappa}{2} \\
& \times \left\{ \frac{\cos(r\nu_{\gamma}\pi/2)}{2} \left[f_c\left(\frac{\Delta\kappa(r\Phi_{\gamma} + x)}{2}\right) + f_c\left(\frac{\Delta\kappa(r\Phi_{\gamma} - x)}{2}\right) \right] \right. \\
& \left. + \frac{\sin(r\nu_{\gamma}\pi/2)}{\sqrt{\pi}} \left[f_s\left(\frac{\Delta\kappa(r\Phi_{\gamma} + x)}{2}\right) + f_s\left(\frac{\Delta\kappa(r\Phi_{\gamma} - x)}{2}\right) \right] \right\} \quad (4.6)
\end{aligned}$$

where

$$f_c(z) = e^{-z^2} \quad \text{and} \quad f_s(z) = e^{-z^2} \int_0^z dt e^{t^2}. \quad (4.7)$$

The function $f_s(z)$ is known as *Dawson's integral*. Both $f_c(z)$ and $f_s(z)$ (see Fig. 4.7) contribute to the sum mainly around $z = 0$. Thus, the Fourier transform of the density will be composed of a background term coming from the averaged density plus a sum of odd and even peaks centered at $x = \pm r\Phi_{\gamma}$, which correspond to the action of the periodic orbits and to their multiples.

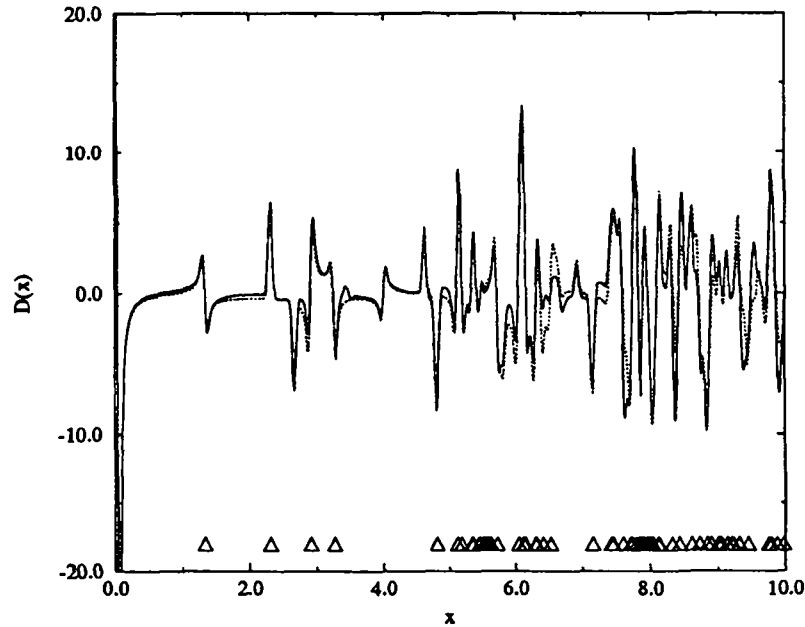


Fig. 4.8. Action spectrum for $\beta_L = 0$, $\beta_R = \pi/3$, $\Delta\kappa = 50$ and $\kappa_o = 0$. The solid line represents the transform of the exact density computed from 3370 levels. The dotted line is obtained from 95 periodic orbits, whose actions are marked with triangles.

When $\kappa_o \gg \Delta\kappa$, one can extend the integration over the whole κ axis, since the contribution of the testfunction is then negligible for $\kappa < 0$. Thus, integrating over all values of κ we obtain the approximation

$$\begin{aligned}
D_{sc}(x)|_{\kappa_o \gg \Delta\kappa} \approx & \left[\frac{\tan(\beta_R)}{4\pi} \kappa_o - \frac{1 + \sec(\beta_R)}{2\sqrt{2}\pi} \right] \frac{2\Delta\kappa\sqrt{\pi}}{3} f_c \left(\frac{\Delta\kappa x}{2} \right) \\
& + \sum_{\gamma} \sum_{r=1}^{\infty} \frac{\Phi_{\gamma}}{\pi} \frac{1}{\sqrt{|\det[\mathbb{1} - (\partial P_{\gamma})^r]|}} \frac{\sqrt{\pi}\Delta\kappa}{2} \\
& \times \frac{\cos(r\nu_{\gamma}\pi/2)}{2} \left[f_c \left(\frac{\Delta\kappa(r\Phi_{\gamma} + x)}{2} \right) + f_c \left(\frac{\Delta\kappa(r\Phi_{\gamma} - x)}{2} \right) \right]. \quad (4.8)
\end{aligned}$$

Figure 4.8 represents the Gutzwiller trace formula (3.80) applied on the above test-function with $\kappa_o = 0$ for the wedge with $\beta_R = \pi/3$. The solid line is obtained from (4.5) with the lowest 3370 eigenenergies. A reasonable choice for the width of the Gaussian is $\Delta\kappa = 50$. The dotted line stands for the semiclassical approximation (4.6) with 95 periodic orbits. These are all periodic orbits with action $\Phi_{\gamma} < 10$, except the grazing ones with $m > 13$. The actions (in units of \hbar) are marked with triangles. The agreement between both curves is rather good in general. Recall that the coding of the periodic orbits with the letters T and V (according to the sequence of submaps) is believed to lead to a different word for each periodic orbit. The orbit with action $\Phi_{\gamma} \approx 3.26$ is bouncing exactly in the corner, and hence may be coded either $TTTV$ or TVV . As the angle is of the type π/n with $n \in \mathbb{N}^*$ and n is odd, this orbit is well defined, but the corresponding monodromy matrix does not exist [DR]. Perturbation of this orbit leads to either $TTTV$ or TVV , depending on the first side hit near to the corner. So one has to derive a special saddle-point approximation which takes into account both behaviors. Following Szeredi [SG2], we approximate the total contribution of this special orbit by half the contributions of both $TTTV$ and TVV .

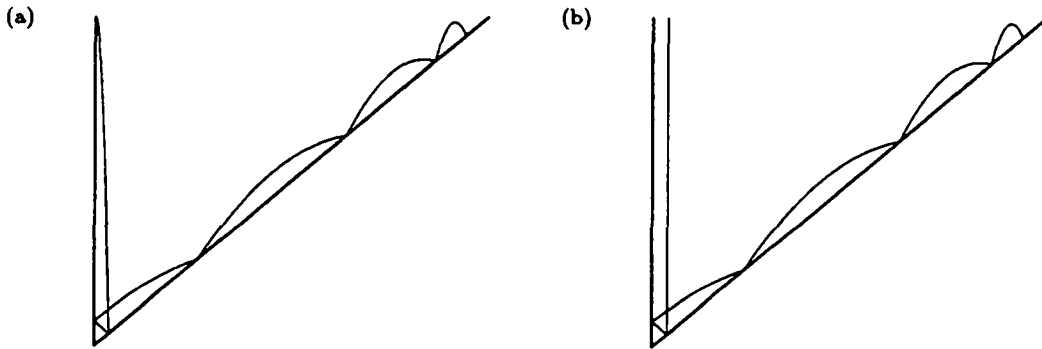


Fig. 4.9. Families tending to an orbit running along the boundary: (a) Orbit of the grazing family $VVVT^m$ for $m = 6$. (b) Orbit of the grazing family $VTVT^m$ for $m = 6$.

A crucial assumption for the derivation of the Gutzwiller formula is that all periodic orbits are isolated and unstable. In the present case, we encounter only one problematic family of *grazing orbits* (see Fig. 4.9) which tend to a limit orbit running along

the boundary. The contribution of such families is difficult to estimate, since only the first members may be considered as isolated, but not the ones near the accumulation point. Nevertheless, it has been observed on the stadium billiard [SSCL] that adding only the contributions of a few first members reproduces the exact density accurately, pointing out a high cancellation phenomenon between pairs of periodic orbits belonging to different grazing families.

Table 4.1. Asymptotic behavior of grazing families $VVVT^m$ and $VTVT^m$ for large m .

	$VVVT^m$	$VTVT^m$
Φ_γ	$4\sqrt{2}(1 - m^{-2} + 2m^{-3}) + O(m^{-5})$	$4\sqrt{2}(1 - m^{-2} + 2m^{-3}) + O(m^{-4})$
σ_γ	-1	+1
μ_γ	$\log(2m^2 + 4m + 8 + O(m^{-2}))$	$\log(2m^2 + 4m + 10 + O(m^{-2}))$
ν_γ	$15 + 3m$	$13 + 3m$

We shall now analyze in detail the contribution of grazing orbits for the wedge with $\beta_R = \pi/3$ [SG2]. The code for the most obvious grazing family reads $VVVT^m$, where T^m means that the particle successively hits m times the inclined side without touching the vertical one. There exists another grazing family, labeled $VTVT^m$, which is a good candidate to cancel the contributions of the family $VVVT^m$ for large m . Both families tend to the same limit orbit sliding along the boundary, bouncing in the corner, going up vertically and coming back on the same path. Bouncing along the inclined boundary is integrable motion. So the map T reduces to a linear transformation in appropriate coordinates, and it is possible to compute analytically the exact location and the properties of both families. The behavior of the quantities describing both grazing families is summarized in Table 4.1, where the denominator $|\det[\mathbb{1} - (\partial P_\gamma)^r]|^{-1/2}$ is characterized by σ_γ , the sign of the trace of the monodromy matrix ∂P_γ , and μ_γ , the largest eigenvalue of ∂P_γ . Notice that the limit trajectory is bouncing exactly in the vertex, where specular reflection may not be continuously defined for arbitrary angle. Here it is well defined, since the boundary is regular near the corner and the angle is of the type π/n . In contrast to what has been observed in [SG2], we did not find infinite families for $\beta_R = 49^\circ$. We suspect that they may exist only when the limit orbit is well defined.

The Maslov index ν_γ is generally very difficult to compute analytically. It may be extracted from numerical simulations using the method described in [CRL]. Special care has to be taken when the particle bounces against the vertical wall with almost zero velocity. Out of the numerical data we found the simple rule “add 3 for a T mapping and 5 for a V mapping”. This rule seems incredibly simple, but it never failed on the several hundreds orbits we investigated. We have no analytical proof of it.

The main difference between both families is the way of inverting the direction of the velocity near the vertical side. Orbits of the type $VVVT^m$ hit the vertical side perpendicularly with almost zero velocity, whereas the orbits $VTVT^m$ bounce up vertically, slow down to zero velocity and come back because of the potential. This causes a difference of 2 in the Maslov index. Therefore the contributions of both families, which are very close in absolute value for large m , take opposite signs and cancel. However, this does not mean that one may consider the orbits near the accumulation point as isolated.

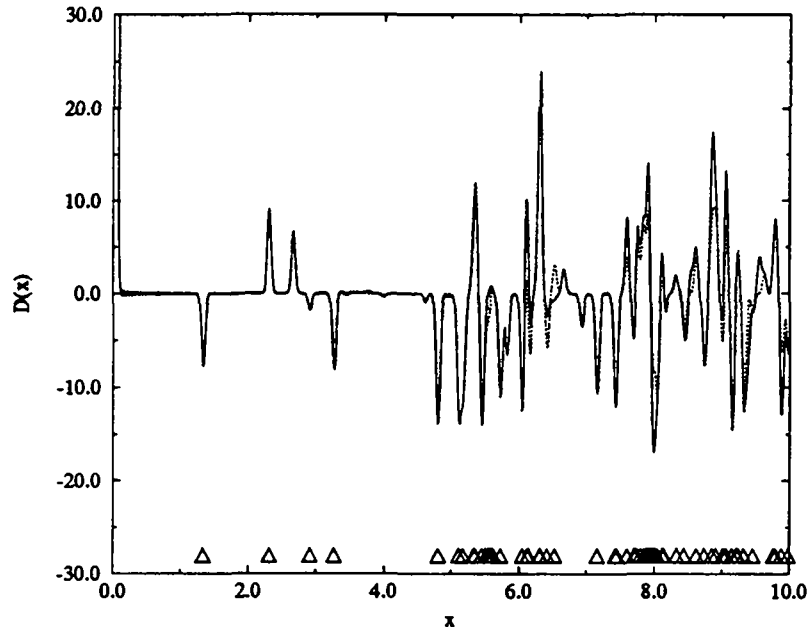


Fig. 4.10. Action spectrum for $\beta_L = 0$, $\beta_R = \pi/3$, $\Delta\kappa = 50$ and $\kappa_o = 150$. The solid line represents the transform of the exact density computed from 3370 levels. The dotted line is obtained from the same 95 periodic orbits as before. The actions of the periodic orbits are marked with triangles.

The situation appears to be similar in the stadium, where one grazing family bounces twice in the corner to invert the direction of its velocity, while the other bounces perpendicularly to one side. This leads to the same difference in the Maslov indexes, and hence to cancellation of the contributions. Notice that in both cases, the grazing families are due to a part of the boundary along which motion is integrable, and the limit orbit bouncing exactly in the corner is well defined. Thus it seems that the symmetry of the dynamics near the corner plays a central role in the existence of infinite families and in the mechanism of cancellation.

The point of accumulation of grazing orbits stands at $x = 4\sqrt{2} \approx 5.65$. The excellent matching between the curves around that point, despite the reduced number of members of the grazing families, is due to the above described cancellation phenomenon. The other differences might originate from terms which have been neglected in the approximation (3.79). One cannot exclude a possible calculation error in the Maslov

index, because of the difficulties involved in the numerical evaluation of some orbits. Such errors are difficult to detect when several orbits have nearly the same action.

In Fig. 4.10 we set $\kappa_o = 150$ and used exactly the same data as before. The agreement between the curves improves significantly. This demonstrates the importance of the choice of the testfunction. Centering the Gaussian away from zero takes advantage of more eigenenergies, since the density of levels increases with κ . Moreover, as (3.80) is expected to hold in the semiclassical regime, it is natural to shift the weight to higher energies.

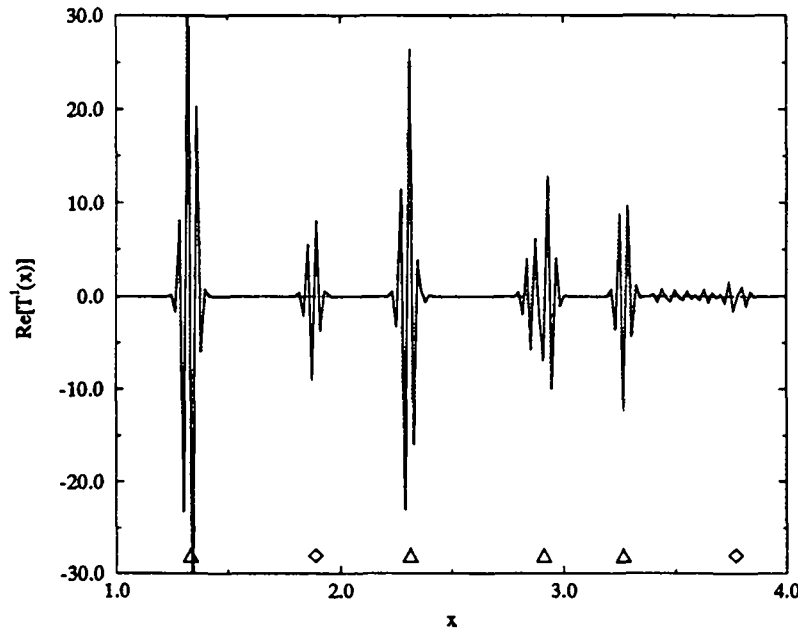


Fig. 4.11. Real part of the action spectrum of $\text{Tr}S_{sq}$ for $\beta_L = 0$, $\beta_R = \pi/3$, $\Delta\kappa = 50$ and $\kappa_o = 150$. The solid line represents the transform of the semiquantal expression. The dotted line is obtained from the periodic orbits bouncing only once against the vertical wall. The contributions due to the onset of new channels are marked with diamonds.

The Gutzwiller trace formula makes use of all periodic orbits of the classical system. Hence it is very difficult to identify the contributions of the various periodic orbits from the rest. In our derivation we obtained this formula as a sum over the traces of the powers of S_{sq} . We can therefore check the semiclassical approximation in more detail by considering the approximation (3.79) of $\text{Tr}S_{sq}^n$ for each n separately. For the wedge billiard, the period n_γ represents the number of collisions with the vertical boundary, and hence corresponds to the number of V 's contained in the code of the orbit. Because of the potential, each periodic orbit has to hit at least once the vertical side, so that each code contains at least one V . Thus every periodic orbit of the system contributes to one of the powers of S . Here again we are confronted with the problem of the contributions of the grazing families. For $\beta_R = \pi/3$, all members of the families $VTVT^m$ and $VVVT^m$ have to be included in the evaluation of $\text{Tr}S_{sq}^2$.

and $\text{Tr}S_{sq}^3$ respectively. Here the previous mechanism of cancellation does not apply, since both families contribute to separate quantities. However, as the Maslov index steadily increases by 3 for each member of the same family, contributions from consecutive members (considered here as separated) will have different phases so that the whole sum will converge at the end.

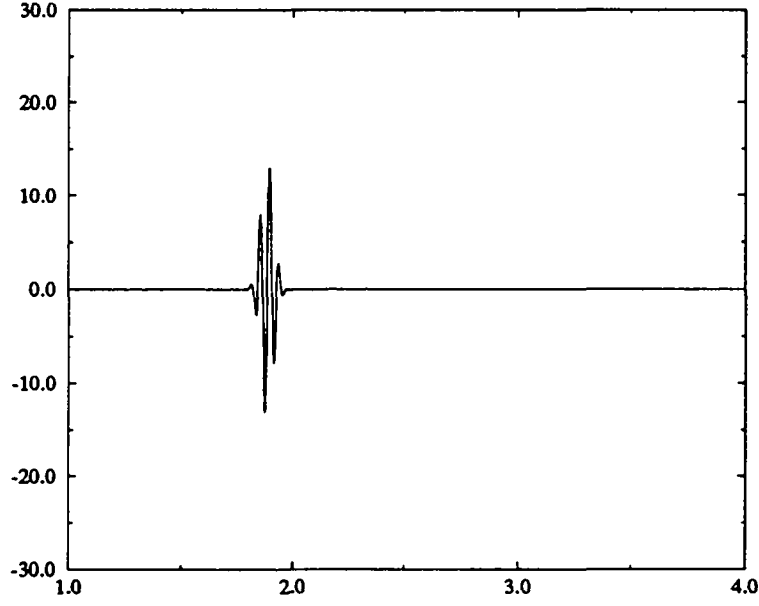


Fig. 4.12. Real part of the function $C_m(x)$ for $m = 1$, $\Delta\kappa = 50$, $\kappa_o = 150$. This contribution is due to the repetitive opening of new conducting channels.

For the same reasons discussed above, we calculate a weighted Fourier transform of $\text{Tr}S_{sq}^n(\kappa)$:

$$T^n(x) = \int_0^\infty d\kappa \exp\left[-\left(\frac{\kappa - \kappa_o}{\Delta\kappa}\right)^2\right] \exp[i\kappa x] \text{Tr}S^n(\kappa). \quad (4.9)$$

The semiclassical approximations with $\kappa_o = 0$ and $\kappa_o \gg \Delta\kappa$ read

$$T_{sc}^n(x)|_{\kappa_o=0} = \sum_{\{\gamma | n_\gamma r_\gamma = n\}} \frac{n_\gamma}{\sqrt{|\det[\mathbb{1} - (\partial P_\gamma)^{r_\gamma}]|}} \Delta\kappa \exp\left[-ir_\gamma \nu_\gamma \frac{\pi}{2}\right] \times \left[\frac{\sqrt{\pi}}{2} f_c\left(\frac{\Delta\kappa(r_\gamma \Phi_\gamma - x)}{2}\right) + i f_s\left(\frac{\Delta\kappa(r_\gamma \Phi_\gamma - x)}{2}\right) \right] \quad (4.10)$$

$$T_{sc}^n(x)|_{\kappa_o \gg \Delta\kappa} \approx \sum_{\{\gamma | n_\gamma r_\gamma = n\}} \frac{n_\gamma}{\sqrt{|\det[\mathbb{1} - (\partial P_\gamma)^{r_\gamma}]|}} \Delta\kappa \sqrt{\pi} \times \exp\left[ir_\gamma \left(\Phi_\gamma - \nu_\gamma \frac{\pi}{2}\right) - i\kappa_o x\right] f_c\left(\frac{\Delta\kappa(r_\gamma \Phi_\gamma - x)}{2}\right) \quad (4.11)$$

We shall present results which are calculated for the semiclassical domain $\kappa_o \gg \Delta\kappa$. Figure 4.11 represents the real part of the transform for $n = 1$ and $\kappa_o = 150$. The

solid line stands for $T^1(x)$. It is obtained from the discrete Fourier transform of 900 values with κ between 0 and 332. The dotted line represents $T_{sc}^1(x)|_{\kappa_0 \gg \Delta\kappa}$. It is computed from all periodic orbits bouncing only one time against the vertical wall. The actions of these four orbits are marked with triangles. The semiclassical approximation perfectly matches the exact curve around the periodic orbits. For the same reason as before, we take half the contribution of the orbit $TTTV$. Here the process is obvious, since TVV does not contribute to this sum.

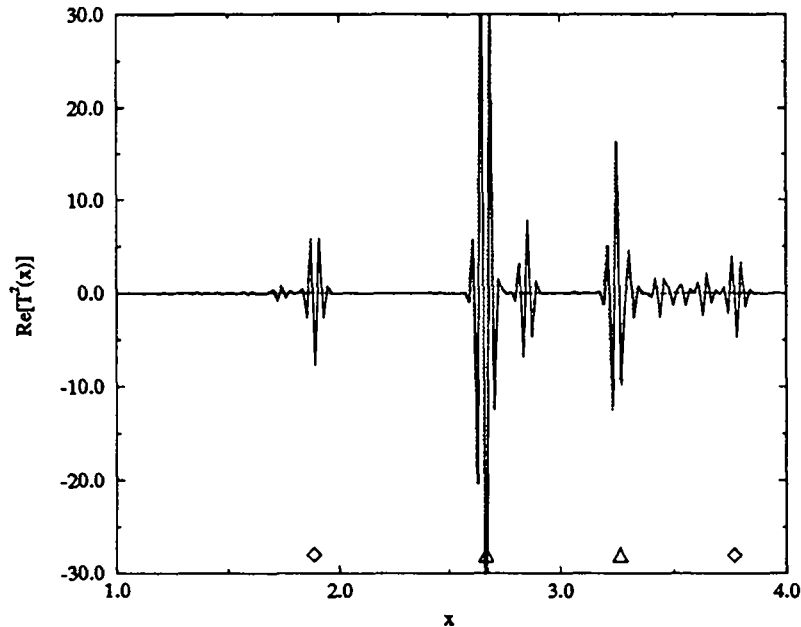


Fig. 4.13. Real part of the action spectrum of $\text{Tr}S_{s,q}^2$ for $\beta_L = 0$, $\beta_R = \pi/3$, $\Delta\kappa = 50$ and $\kappa_0 = 150$. The solid line represents the transform of the semiquantal expression. The dotted line is obtained from the two shortest periodic orbits bouncing twice against the vertical wall. The contributions due to the onset of new channels are marked with diamonds.

Apart from the large peaks which appear at the location of periodic orbits, there are also other contributions which are yet unexplained by the semiclassical theory. We shall show that the peaks at multiples of $4\sqrt{2}/3 \approx 1.88$ (marked with diamonds) are related to the onset of thresholds.

We have checked that the above peaks at multiples of $4\sqrt{2}/3$ appear independently of the value of β_R . Hence they cannot be associated with isolated periodic orbits of the classical system. They would rather be connected with classical motion in the wave guide. They appear at multiples of the action of an orbit which would bounce perpendicularly to the walls of the wave guide. Actually their quantum origin lies in the behavior of $S_{s,q}$ at the threshold for a new conducting mode for

$$\kappa_l = E_l^{3/2} \approx a l \quad \text{where} \quad a = \frac{3\pi}{2\sqrt{2}} \quad \text{and} \quad l \in \mathbb{N}^*. \quad (4.12)$$

The constant a is determined by the asymptotic behavior of the zeros of A_i . As the size of S_{sq} increases by one at κ_l , the traces are also discontinuous. We can model such discontinuities by a theta distribution shifted away from the origin times an amplitude.

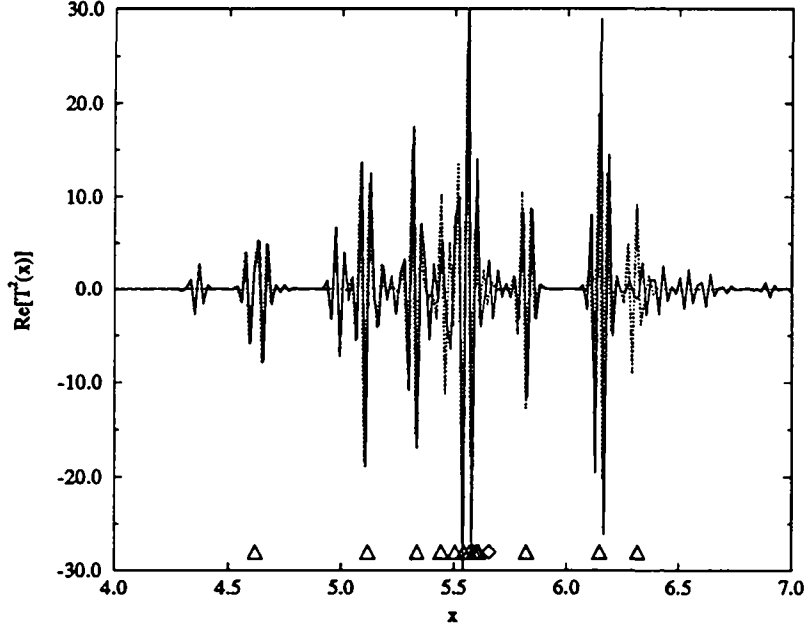


Fig. 4.14. Real part of the action spectrum of $\text{Tr}S_{sq}^2$ for $\beta_L = 0$, $\beta_R = \pi/3$, $\Delta\kappa = 50$ and $\kappa_o = 150$. The solid line represents the transform of the semiquantal expression. The dotted line is obtained from the periodic orbits bouncing twice against the vertical wall and the lowest 10 members of the grazing family $VTVT^m$. The contributions due to the onset of new channels are marked with diamonds.

Because of the unitarity of S_{sq} , all its elements are of order 1. Thus the amplitude will be of the same order. What is important for the Fourier transform is the repetitive appearance of a discontinuity for each κ_l . Using the Fourier decomposition of theta distributions, the sum reduces to a geometric series. Reintegrating over a closed path in the complex plane, we obtain

$$\sum_{l=1}^{\infty} \theta(\kappa - \kappa_l) \approx \theta(\kappa - a) \left[\left(\frac{\kappa}{a} - \frac{1}{2} \right) - \sum_{m \in \mathbb{Z}^*} \frac{i}{2\pi m} \exp \left(i\kappa \frac{2\pi m}{a} \right) \right]. \quad (4.13)$$

Evaluation of the first term of this distribution over the previous Gaussian testfunction with $\kappa_o \gg \Delta\kappa$ gives a contribution near zero, whereas the other terms $m \in \mathbb{Z}^*$ lead to functions

$$\begin{aligned} C_m(x) &= \frac{i}{2\pi m} \int_a^{\infty} d\kappa \exp \left[- \left(\frac{\kappa - \kappa_o}{\Delta\kappa} \right)^2 \right] \exp \left[i\kappa \left(x - \frac{2\pi m}{a} \right) \right] \\ &= \frac{i}{2\pi m} \Delta\kappa \sqrt{\pi} \exp \left[i\kappa_o \left(x - \frac{2\pi m}{a} \right) \right] f_c \left[\left(x - \frac{2\pi m}{a} \right) \frac{\Delta\kappa}{2} \right]. \end{aligned} \quad (4.14)$$

Figure 4.12 represents $\text{Re}\{C_1(x)\}$, and we can see that the shape of this correction well fits the peak at $x = 4\sqrt{2}/3$ on Fig.4.13. It is clear that each C_m is at the origin of a similar contribution localized around $x_m = m4\sqrt{2}/3$. Moreover, such functions are totally independent of value of the angle of the wedge.

In Fig. 4.13 and Fig. 4.14 we plot $T^2(x)$ and $T_{sc}^2(x)|_{\kappa_0 \gg \Delta\kappa}$ on a range including all periodic orbits bouncing twice against the vertical wall. The dotted line results from 5 isolated periodic orbits and from the first 10 members of the family $VTVT^m$. The semiclassical approximation reproduces well the behavior of $T^2(x)$ near the accumulation point at $x \approx 5.65$, pointing out the proper mechanism of cancellation of this family.

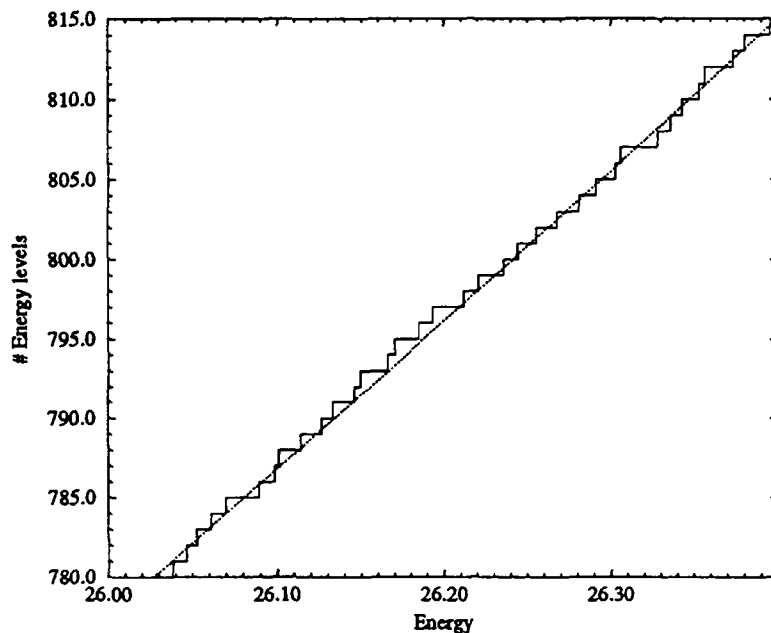


Fig.4.15. Integrated density of energy for $\beta_L = 0$, $\beta_R = \pi/3$ and E such that $\Lambda(E) = 40$. The solid line represents the exact integrated density $N(E)$. The dotted line is obtained from the phase of $\det(-S)$ divided by 2π and stands for the semiclassical approximation of $N_{AV}(E)$.

The traces of the powers of S give the semiclassical approximation of the oscillatory part of $d(E)$. It is also easy to check the formula for the averaged density via (3.77), which gives an approximation of the integrated averaged density as a quantity depending on the S matrix. The solid line on Fig. 4.15 represents the exact integrated density $N(E)$ for the range of energy where $\Lambda(E) = 40$ and $\beta_R = \pi/3$. The dotted line is computed from the variation of the phase of $\det(-S)$ divided by 2π and stands for the semiclassical approximation of $N_{AV}(E)$.

4.4 Semiclassical Evolution of a Wave Packet

In this section we turn back to the problem of characterizing a chaotic system. We have seen that classically a system is chaotic if small differences in the initial conditions leads to large differences in the final outcome. As a result, the long time behavior of the system is unpredictable. Similar quantities involving time evolution are hardly available quantum mechanically.

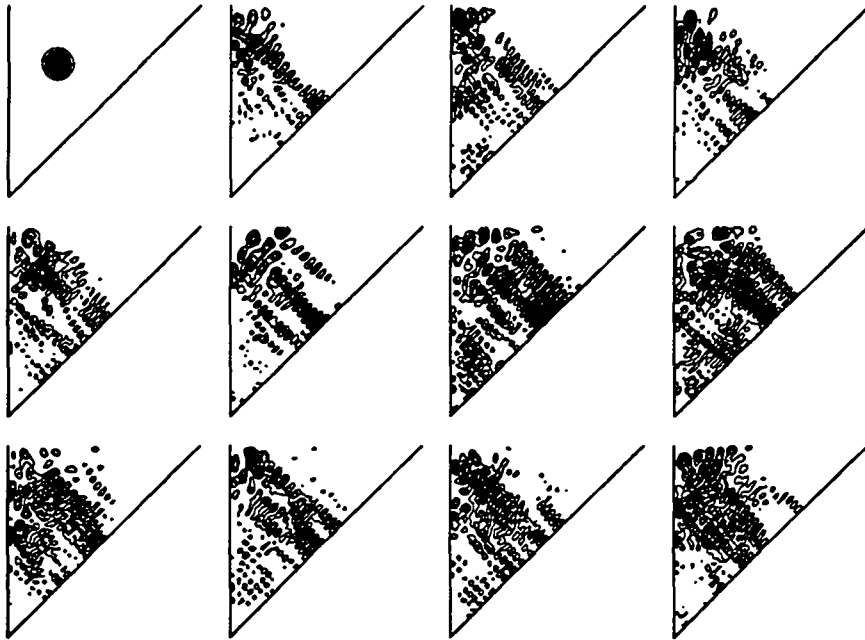


Fig. 4.16. Quantum propagation of a Gaussian wave packet in a half wedge with angle $\beta_R = \pi/4$.

Time evolution of a quantum system is trivial, once an eigenbasis of the Hamilton operator \hat{H} has been found. For integrable systems, one can then decompose any wave function on this basis and let the phases evolve according to Schrödinger's equation. For non-integrable systems, we are stuck because we do not know the eigenfunctions analytically. This is why this problem has to be investigated on a computer. One could imagine decomposing the wave function on some truncated basis determined numerically, and then computing the evolution as in the integrable case. As a matter of fact it appears to be much simpler to integrate directly the Schrödinger equation, starting from an initial wave function on a discretized Hilbert space. Such techniques involving Fourier transformation have been developed in molecular dynamics to compute quantum propagation for time independent as well as time dependent Hamiltonians (see [Ko]). This Fourier method is able to represent a system with the efficiency of one sampling point per unit volume \hbar in phase space. With proper choice of the parameters and initial wave function, one expects

exponential convergence in relation to the number of sampling points, so that a good description is already obtained with a relatively small number of points.

The method is straightforward to implement and will not be discussed in this context. We will consider the quantum propagation of Gaussian wave packets on a two dimensional phase space of size 64×64 . The initial Gaussian wave functions are of the form

$$\Psi_{(\mathbf{x}_\alpha, \mathbf{p}_\alpha)}(\mathbf{x}) = \frac{1}{\sqrt{\pi\sigma^2}} \exp \left[-\frac{(\mathbf{x} - \mathbf{x}_\alpha)^2}{2\sigma^2} + \frac{i}{\hbar} \mathbf{p}_\alpha(\mathbf{x} - \mathbf{x}_\alpha) \right]. \quad (4.15)$$

They are centered around points \mathbf{x}_α in configuration space, and the velocity is directed along \mathbf{p}_α , where $(\mathbf{x}_\alpha, \mathbf{p}_\alpha)$ corresponds to an initial condition of the underlying classical system. Setting the ratio of the typical quantum and classical actions $\hbar = 0.01$, we obtain a reasonable description of the system in the semiclassical approximation (here again we could rather use the word semiquantal, since the equations are involving purely quantum quantities).

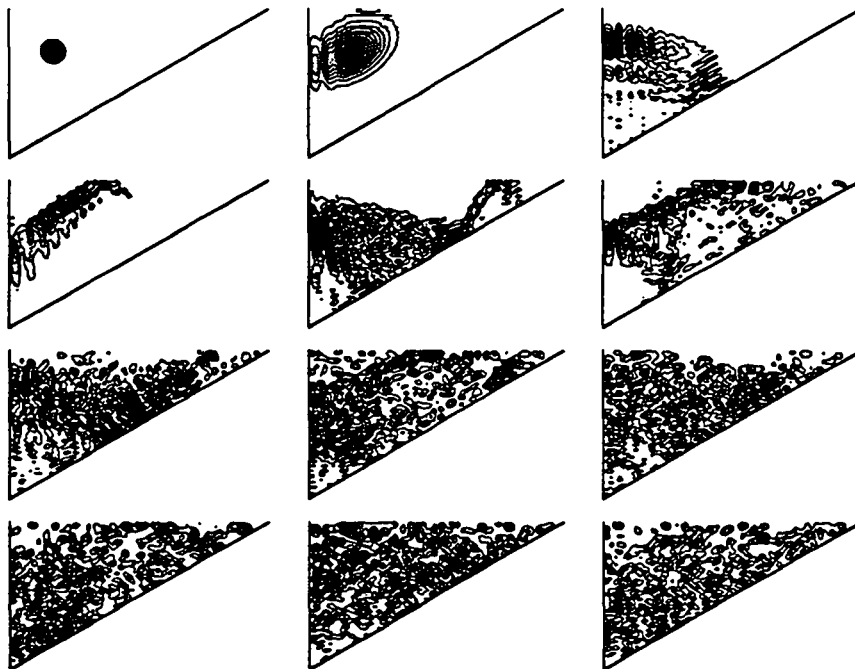


Fig. 4.17. Quantum propagation of a Gaussian wave packet in a half wedge with angle $\beta_R = \pi/3$.

First we consider a half wedge with $\beta_R = \pi/4$, and set the parameters $(\mathbf{x}_\alpha, \mathbf{p}_\alpha)$ of the initial wave packet so that the classical initial condition corresponds to the shortest periodic orbit of the system. Since this half wedge is integrable, the orbit is marginally stable. Figure 4.16 represents the quantum evolution of the density of probability $|\Psi_{(\mathbf{x}_\alpha, \mathbf{p}_\alpha)}(\mathbf{x})|^2$. The time interval between the snapshots is 10 times the period of the periodic orbit ($10 \times \sqrt{2}$). Already after the first time step ($t \simeq 14.1$), the wave function does not look like a localized state anymore. However, even after

time of order \hbar^{-1} (see last snapshot with $t \simeq 155.5$) the wave function did still not spread over the whole phase space. Figure 4.17 represents a similar sequence of snapshots for the chaotic half wedge with $\beta = \pi/3$. The time interval is half the period of the periodic orbit ($\frac{1}{2} \times 2$) on which the localized state is set. On the fifth picture ($t = 4$) the structure of a localized peak is already lost. But this time the spreading over the whole phase space is much faster than in the integrable case.

This comparison provides an easy illustration of the difference between two quantum systems with underlying integrable and chaotic classical dynamics. Changing the size of the grid would certainly improve the quality of the result, but is not necessary for our purpose. Note that a refinement of this method for billiards has been used in [ToH] to show that the long time semiclassical dynamics is still accurate for time beyond $\ln(\hbar^{-1})$.

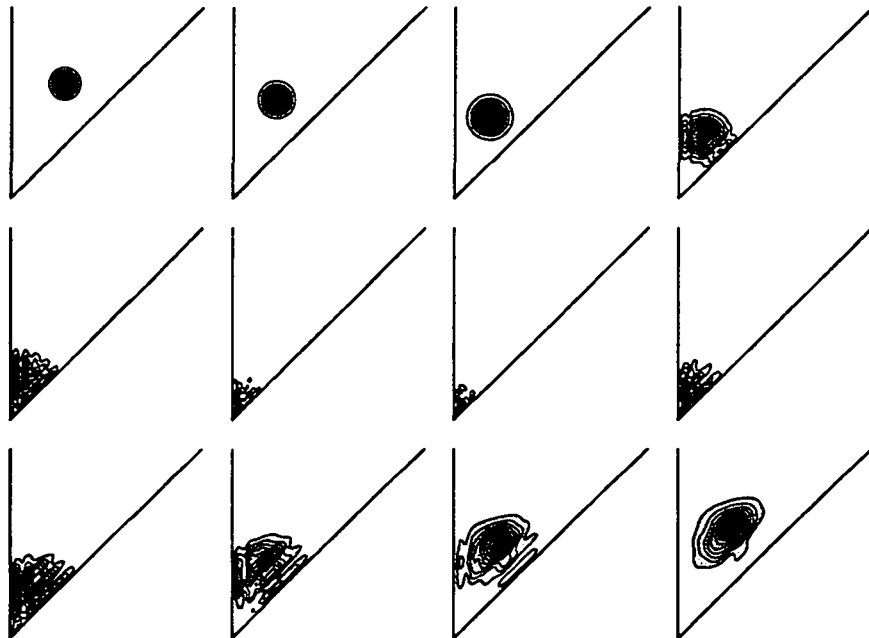


Fig. 4.18. Quantum propagation of a Gaussian wave packet in the corner of a half wedge with angle $\beta_R = \pi/4$.

Our second illustration is related to the influence of the singularity in the corner of the wedge. As a quantum system is essentially a boundary condition problem in the case of billiards, the singularity can not be treated as in the classical case. However, we found interesting to see what happens to a wave packet sent straight into the corner, in analogy to a swarm of classical trajectories. The quantum propagation of such a wave packet in a corner with angle $\beta_R = \pi/4$ is represented in Fig 4.18. The time interval between the snapshots is much shorter than before, so that we can examine what happens in the corner. On the sequence, one can clearly see how the wave packet focuses on the top of the corner and then comes out of it, slightly

deformed. In this case the spreading does not seem to have been influenced by the singularity, in the same way that a swarm of trajectories is not separated but just deformed after leaving such a corner.

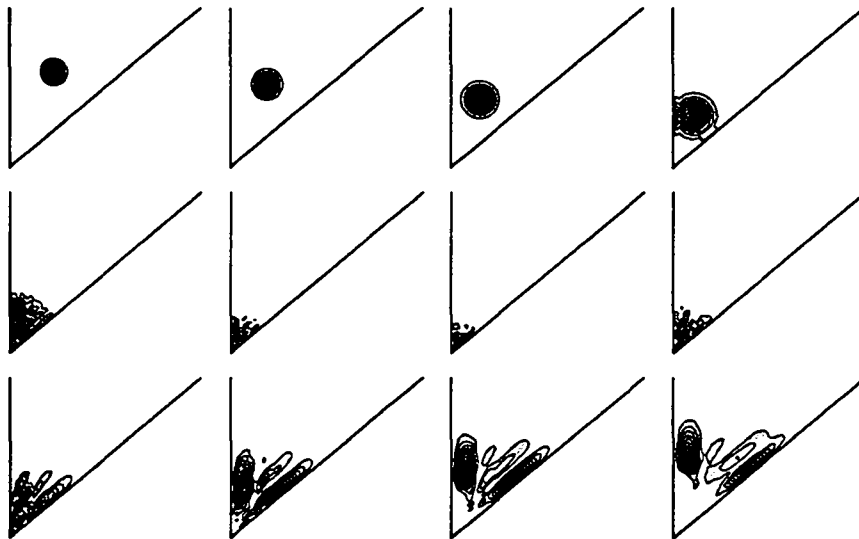


Fig. 4.19. Quantum propagation of a Gaussian wave packet in the corner of a half wedge with angle $\beta_R = 50^\circ$.

On Fig 4.19 we repeat the same experiment on a half wedge with $\beta_R = 50^\circ$. As the angle is not of the type π/n , we expect that the singularity will have a stronger effect on the dynamics. Actually the wave packet also focuses on the top of the corner, but comes out in two pieces. The directions of these latter correspond to the directions of the two pieces of the swarm in the classical case. Thus, in the semiclassical limit, one finds the same kind of behavior as in the classical case, though the dynamics is governed by a wave equation. Hence corners may be used as devices which may cut localized states into several pieces.

4.5 Statistical Analysis

We have seen in the previous section that quantum propagation of a given system may be treated numerically. Nevertheless, statistical properties of classical systems are defined in the limit of infinite time. When studying the correspondence between classical and quantum systems, such investigation becomes problematic since both limits $\hbar \rightarrow 0$ and $t \rightarrow \infty$ do not commute. This is why one is led to consider sta-

tionary properties of the systems. First, we will study the statistics of the energy levels which are believed to be described by Poissonian random processes and Random Matrix Theory (RMT) in integrable and strongly chaotic cases respectively. A second characterization will be obtained looking at the statistical properties of the eigenphases of the S matrix. Next we will check other theoretical predictions about the universal behavior of these quantities when a parameter of the system is varied.

4.5.1 Statistics of Eigenenergies

Quantum Hamiltonians can be represented by Hamiltonian matrices. Generally, even if one knows the Hamiltonian matrix exactly, it is too complicated to be diagonalized practically. The purpose of statistical mechanics is to make predictions in spite of the lack of knowledge resulting from the complexity of the system. The Hamiltonian will be characterized by some average property over the fluctuations $d_{osc}(E) = d(E) - d_{AV}(E)$ of the spectrum (the average density $d_{AV}(E)$ contains information on the volume of the system in phase space). To compare the fluctuations of different systems, we have to rescale them in such way that they have the same mean level spacing. The usual procedure (which is not unique) is called *unfolding* of the spectrum and consists in the transformation

$$E_i \mapsto \varepsilon_i = N_{AV}(E_i) \quad (4.16)$$

of the eigenenergies E_i into the rescaled energies ε_i . The resulting sequence $\{\varepsilon_i\}$ has an average constant mean spacing equal to unity [BG].

As an example, Figure 4.20 represents the lower part of the unfolded spectra of the integrable half wedge ($\beta_R = \pi/4$) and of a chaotic wedge ($\beta_R = \pi/3$). Although

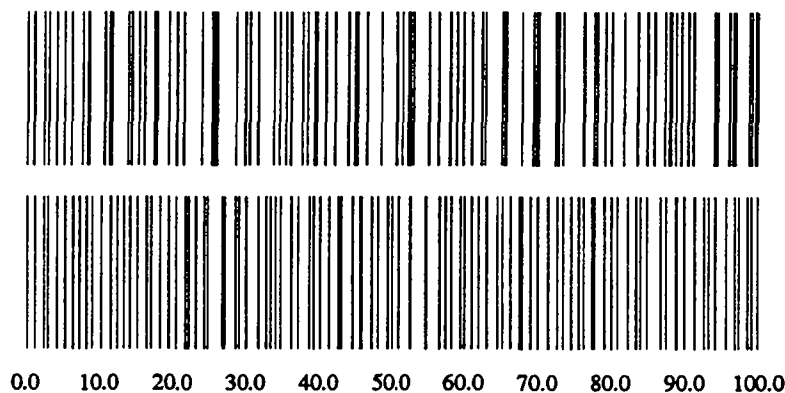


Fig. 4.20. Unfolded spectra of the first 100 eigenvalues corresponding to the integrable half wedge (above) and of a chaotic wedge with $\beta_R = \pi/3$ (below).

the averaged spacing is unity, the eigenenergies seem to be distributed in a different way.

The Bohigas-Giannoni-Schmit [BGS] conjecture is stating that for classically ergodic systems, the statistics of the energy levels is described by an ensemble of the RMT. The underlying space-time symmetries impose restrictions on the ensemble. In the absence of spin, the Hamiltonian matrix can be chosen to be real and symmetric, provided that the Hamiltonian is invariant with respect to time inversion. In this case, the statistical properties of the spectrum will coincide with the ones of the Gaussian Orthogonal Ensemble (GOE). When time reversal symmetry is broken (as in presence of magnetic field, for instance), one has to consider Hermitian matrices which share ensemble properties with the Gaussian Unitary Ensemble (GUE). The statistics is universal in each case, which means that there is no parameter in the theory. Hence the statistical properties should not depend on any particular details of the system.

Using semiclassical arguments, Berry and Tabor [BT2] have shown that for integrable systems the statistics should be close to Poissonian (the second moments of the distributions are the same). This can be heuristically understood because of the existence of quantum numbers. Hence the spectrum is a random superposition of infinitely many number sequences yielding the Poissonian statistics due to the complete absence of statistical correlations.

In this subsection we will verify the above conjectures on the half wedge billiard, using the data set obtained with the scattering method. Some checks concerning the level spacing distribution have already been performed by Wittek [Wi] (using a conventional numerical algorithm to determine the energy levels) who analyzed the behavior of the level spacing distribution as a function of the angle. Here we will introduce several statistical quantities and discuss their universality as a preamble to the next subsection.

The first quantity of interest is the level spacing distribution $P(s)$, where $P(s) ds$ is defined as the probability to find the spacing between any two neighboring energy levels in the interval $[s, s + ds]$. For purely random level sequences, the spacing distribution is Poisson

$$P(s) = \exp[-s] \quad (4.17)$$

while the prediction of RMT for the Gaussian Orthogonal Ensemble (since time reversal symmetry is preserved here) gives the Wigner distribution

$$P(s) = \frac{\pi}{2} s \exp\left[-\frac{\pi}{4} s^2\right]. \quad (4.18)$$

A fundamental difference between both distributions appears at small s , where $P(s) \approx 1 - s$ for Poisson and $P(s) \approx s$ for Wigner. Thus chaotic quantum sys-

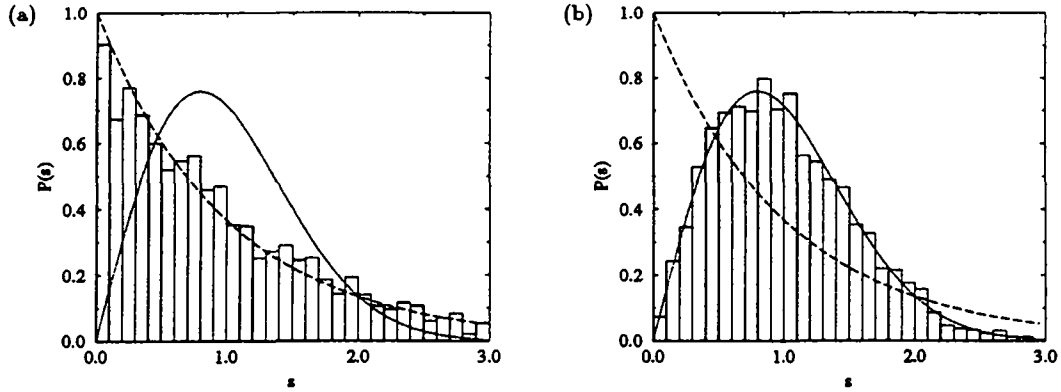


Fig. 4.21. Histogram of the level spacing distribution $P(s)$ of the integrable half wedge (a) and chaotic half wedge (b) with $\beta_R = \pi/3$ obtained from the first 3000 energy levels in each case. The dashed and dotted lines represent the Poisson and Wigner distributions respectively.

tems are showing level repulsion, whereas integrable ones, as a consequence of the randomness of the sequence, do not. Figure 4.21 represents the spacing distributions corresponding to an integrable and a chaotic half wedge. These plots seem to confirm the above predictions, but it is relatively hard to comment on the deviations.

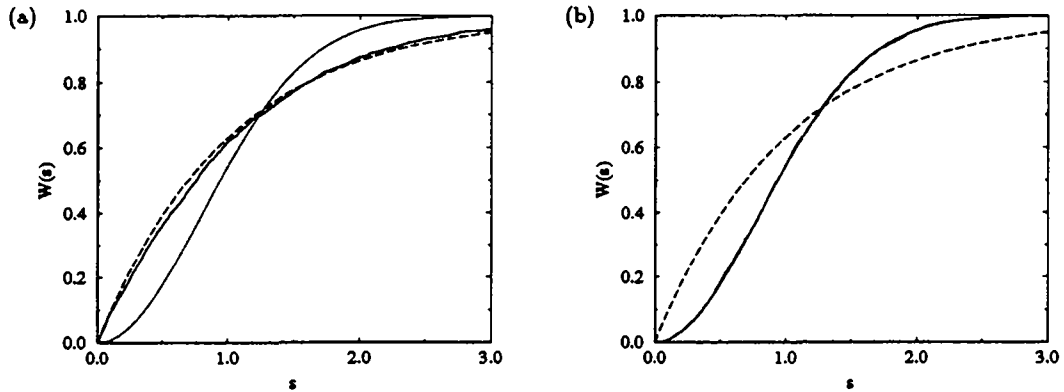


Fig. 4.22. Cumulative level spacing distribution $W(s)$ of the integrable half wedge (a) and chaotic half wedge (b) with $\beta_R = \pi/3$ obtained from the first 3000 energy levels in each case. The dashed and dotted lines represent the Poisson and Wigner cumulative distributions respectively.

It is well known in the statistics that histograms are not a very convenient way of representing the data, since a lot of valuable information is lost due to binning. To allow a better analysis of the data, one should rather use the cumulative level spacing distribution

$$W(s) = \int_0^s dx P(x) = \begin{cases} 1 - \exp[-s] & \text{for Poisson} \\ 1 - \exp\left[-\frac{\pi}{4}s^2\right] & \text{for Wigner} \end{cases} \quad (4.19)$$

represented in Fig. 4.22. Notice that the deviations from the predictions appear to be bigger in the integrable case than in the chaotic case.

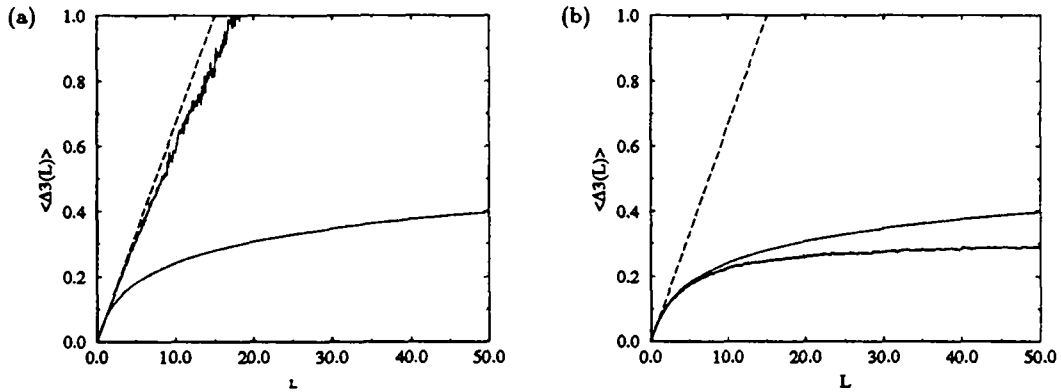


Fig. 4.23. Spectral rigidity $\langle \Delta_3(L) \rangle_\epsilon$ of the integrable half wedge (a) and chaotic half wedge (b) with $\beta_R = \pi/3$ obtained from the first 3000 energy levels in each case. The dashed and dotted lines represent the Poisson and GOE expectations.

The Δ_3 statistics accounts for the rigidity of a finite spectral level sequence. It is defined as the mean square deviation of the spectral staircase function $N(\epsilon)$ counting the number of energy levels below ϵ from the best fit straight line:

$$\Delta_3(\epsilon, L) = \frac{1}{L} \min_{A,B} \int_\epsilon^{\epsilon+L} d\epsilon [N(\epsilon) - A\epsilon - B]^2. \quad (4.20)$$

Usually, one represents the mean $\langle \Delta_3(L) \rangle_\epsilon$ over many non-overlapping adjacent segments of length L . Following Berry [Be], we discuss the signification of this quantity. When $L \ll 1$, we have $\langle \Delta_3(L) \rangle_\epsilon \simeq L/15$ for any level distribution, because of the staircase nature of $N(\epsilon)$. For integrable systems, one expects the behavior

$$\langle \Delta_3(L) \rangle_\epsilon \simeq L/15 \quad (4.21)$$

on the range $[1, L_{max}]$, where L_{max} is determined by the periods of the shortest periodic orbits. When $L > L_{max}$, $\langle \Delta_3(L) \rangle_\epsilon$ reaches a non-universal saturation value Δ_∞ . For classically chaotic system, $\langle \Delta_3(L) \rangle_\epsilon$ grows only logarithmically

$$\langle \Delta_3(L) \rangle_\epsilon \simeq \ln(L)/\pi^2, \quad (4.22)$$

indicating stronger rigidity, or long range order. The corresponding saturation value Δ_∞ is much smaller than in the integrable case (see Fig. 4.23). In both cases L_{max} is much bigger than unity. Thus, this statistics delivers complementary information on middle range correlations, the long range behavior being dominated by the shortest periodic orbits of the system.

Another useful variable is the number statistics (see [BG])

$$n(\epsilon, L) = N(\epsilon + L/2) - N(\epsilon - L/2) \quad (4.23)$$

which corresponds to the number of levels contained in the interval $[\epsilon - L/2, \epsilon + L/2]$. As the mean level spacing is unity, its average value $\langle n(\epsilon, L) \rangle_\epsilon$ is L . The variance of the number statistics

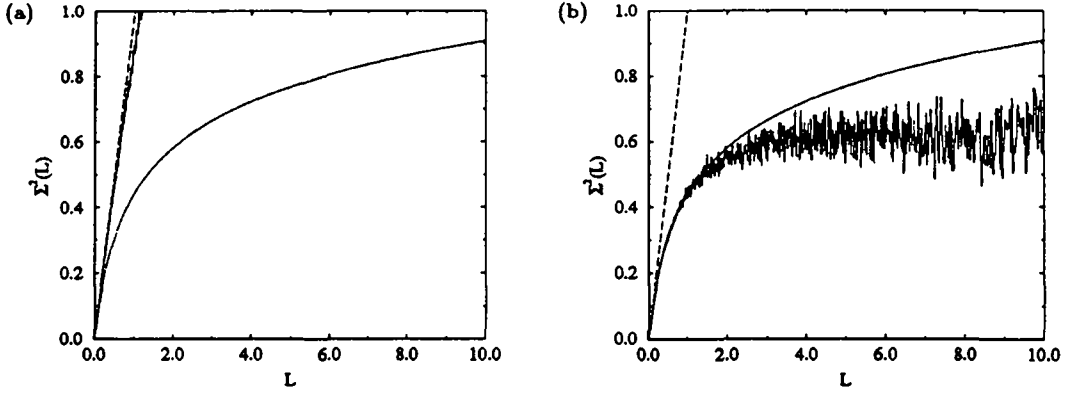


Fig. 4.24. Variance $\Sigma^2(L)$ for the integrable half wedge (a) and chaotic half wedge (b) with $\beta_R = \pi/3$ obtained from the first 3000 energy levels in each case. The dashed and dotted lines represent the Poisson and GOE expectations.

$$\Sigma^2(L) = \langle (n(\varepsilon, L) - L)^2 \rangle_\varepsilon \quad (4.24)$$

is also a measure of the rigidity of the spectrum. For Poisson spectrum, we have

$$\Sigma^2(L) \simeq L \quad (4.25)$$

which means that we expect $L \pm \sqrt{L}$ levels in an interval of length L . For GOE spectrum, the variance $\Sigma^2(L)$ increases only logarithmically and we obtain

$$\Sigma^2(L) \simeq \frac{2}{\pi^2} \ln L. \quad (4.26)$$

Thus, the fluctuations are much smaller than in the integrable case (see Fig. 4.24).

Notice that both $\langle \Delta_3(L) \rangle_\varepsilon$ and $\Sigma^2(L)$ are two points measures which may be shown to verify

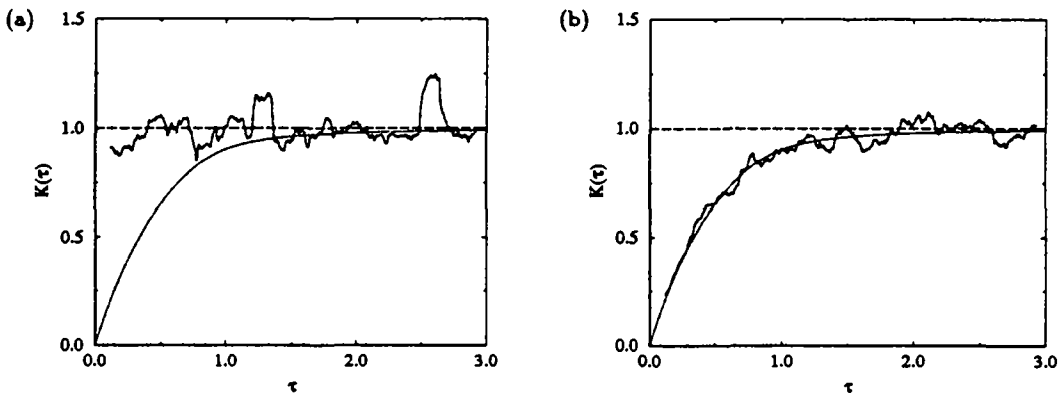


Fig. 4.25. Running average of the spectral form factor $K(\tau)$ for the integrable half wedge (a) and chaotic half wedge (b) with $\beta_R = \pi/3$ obtained from the first 3000 energy levels in each case. The dashed and dotted lines represent the Poisson and Wigner predictions respectively.

$$\langle \Delta_3(L) \rangle_\varepsilon = \frac{2}{L^4} \int_0^L dx (L^3 - 2Lx^2 + x^3) \Sigma^2(x) \quad (4.27)$$

in RMT. They are also related to the two points cluster function Y_2 , which is such that $(1 - Y_2(x)) dx$ represents the probability of observing a level in an infinitesimal interval dx at a distance x from a given level. Next, we present graphs (see Fig. 4.25) of an equivalent quantity in the time domain, the spectral form factor

$$K(\tau) = 1 - \int_{-\infty}^{\infty} dx Y_2(x) \exp[-2\pi i \tau x]. \quad (4.28)$$

For both types of spectra, we have $K(\tau) \rightarrow 1$ when $\tau \gg 1$. The difference lies in the behavior for $\tau < 1$, where $K(\tau) \simeq 1$ for Poisson spectrum, and $K(\tau) \simeq 2\tau - \tau \ln(1 + 2\tau)$ for Wigner spectrum (see [Boh]).

Observation of these variables clearly shows that RMT does not describe the level structure of strongly chaotic systems on all ranges. Surprisingly, sequences of energy levels corresponding to chaotic systems are showing greater rigidity, and hence may be considered as more regular than sequences associated to integrable systems.

4.5.2 Statistics of Eigenphases

In the previous subsection we focused on the fluctuations of the energy spectral density. Moreover, denoting $\delta_{2\pi}$ the 2π periodic delta function, one can rewrite the semiclassical density as

$$d(E) = \sum_{n=1}^{\infty} \delta(E - E_n) = \sum_{l=1}^{\Lambda} \frac{\partial \theta_l}{\partial E} \delta_{2\pi}(\theta_l(E)) \quad (4.29)$$

since one of the eigenphases of the S matrix goes through zero for each eigenenergy of the system. This equation shows that there is some correspondence between the energy spectral density and the eigenphase spectral density.

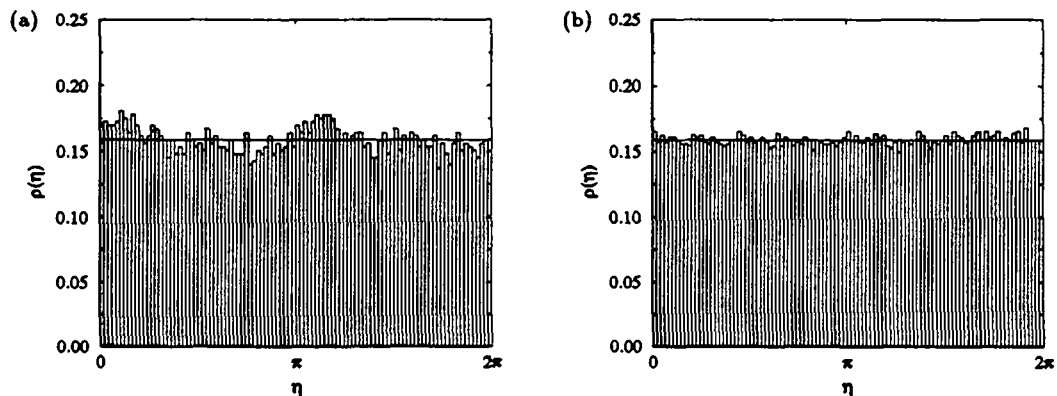


Fig. 4.26. Histogram of the distribution of eigenphases of S for the integrable half wedge (a) and chaotic half wedge (b) with $\beta_R = \pi/3$. Average over 200 S matrices with 100 open channels.

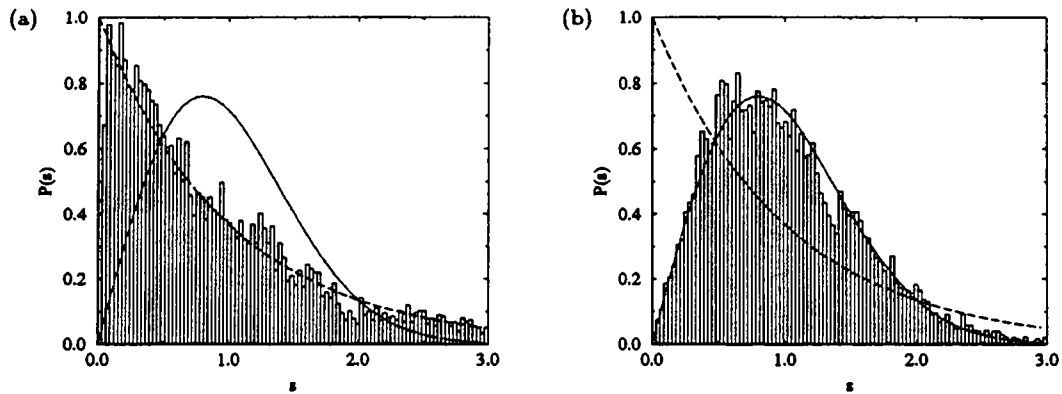


Fig. 4.27. Histogram of the phase spacing distribution $P(s)$ for the integrable half wedge (a) and chaotic half wedge (b) with $\beta_R = \pi/3$. Energy average over 200 S matrices with 100 open channels. The dashed and dotted lines represent the Poisson and COE expectations.

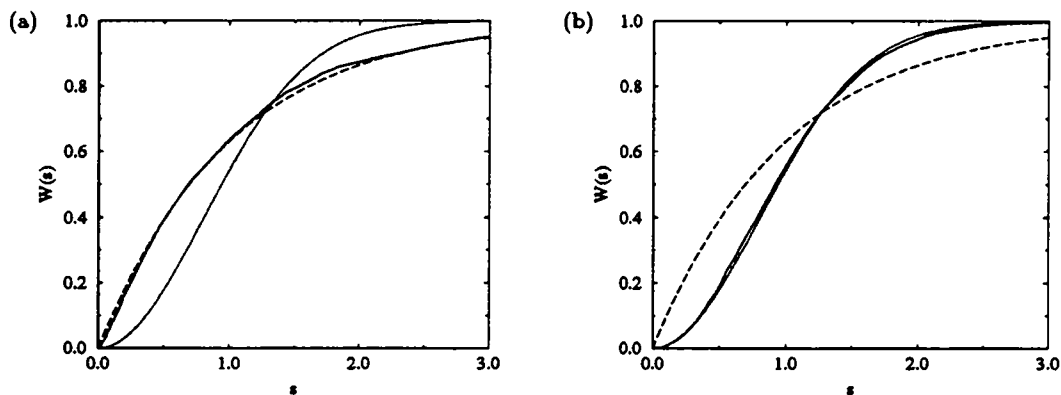


Fig. 4.28. Cumulative phase spacing distribution $W(s)$ for the integrable half wedge (a) and chaotic half wedge (b) with $\beta_R = \pi/3$. Energy average over 200 S matrices with 100 open channels. The dashed and dotted lines represent the Poisson and COE expectations.

Suppose now that the system is characterized by a unitary S matrix, and not by its Hamiltonian H . It has been shown (see [BS]) that S matrices corresponding to classically chaotic systems with time reversal symmetry can be described by the Circular Orthogonal Ensemble (COE) of RMT. As the scattering process is not chaotic for the wedge billiard (recall that the map is hyperbolic, and *iterations* of the scattering map yield chaos) we would like to check the predictions of RMT on this model. Notice that they will concern the unitary part (or semiclassical part) of the S matrix only, and hence the phases which are connected to the energy density. In order to increase our database, we will consider averages over the eigenphases of S matrices at different energies.

First, one has to check that the distribution of the eigenphases of S (or S^R , since $S^L = -1$) on the unit circle is constant and equals $\frac{1}{2\pi}$, as expected for COE (see Fig. 4.26). This is the main difference between GOE and COE: eigenvalues of GOE

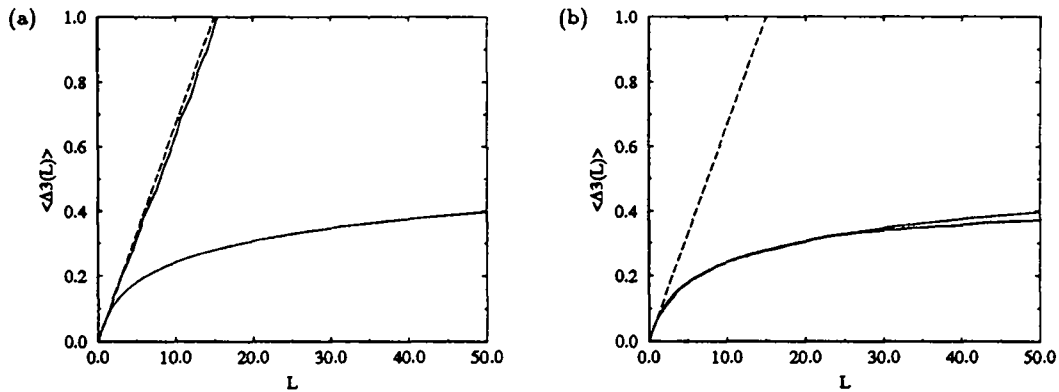


Fig. 4.29. Spectral rigidity $\langle \Delta_3(L) \rangle_e$ for the integrable half wedge (a) and chaotic half wedge (b) with $\beta_R = \pi/3$. Energy average over 200 S matrices with 100 open channels. The dashed and dotted lines represent the Poisson and COE expectations.

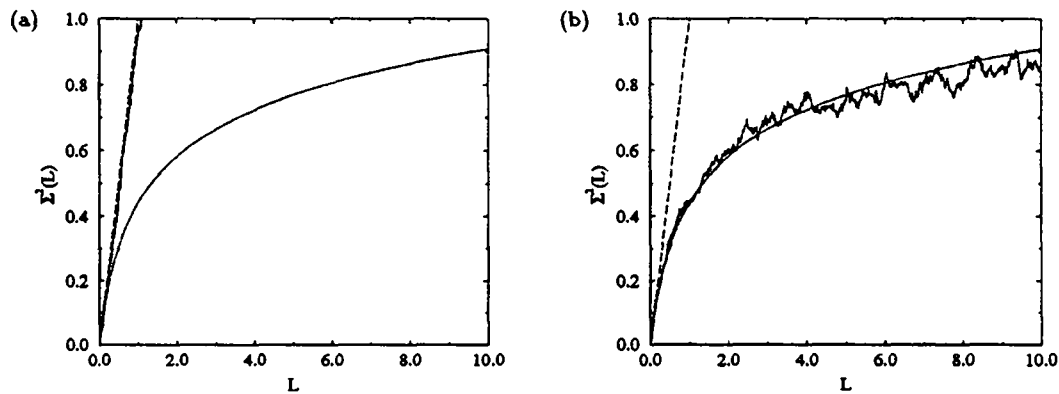


Fig. 4.30. Variance Σ^2 for the integrable half wedge (a) and chaotic half wedge (b) with $\beta_R = \pi/3$. Energy average over 200 S matrices with 100 open channels. The dashed and dotted lines represent the Poisson and COE expectations.

matrices follow the semi-circle density rule, whereas eigenvalues of matrices of the COE type show a uniform probability distribution. However, in the asymptotic limit of infinitely large Hamiltonian matrices the eigenvalue density is roughly constant, and the two points correlation function Y_2 is identical for COE and GOE. Therefore, all two points measures which may be computed from Y_2 are the same for COE and GOE in this limit.

Thus, the statistical properties of the eigenphases will be identical to the ones of the eigenenergies if the former are well described by COE. Figures 4.27, 4.28, 4.29, 4.30 and 4.31 represent the spectral quantities $P(s)$, $W(s)$, $\langle \Delta_3(L) \rangle_e$, $\Sigma^2(L)$ and $K(\tau)$ computed from S matrices corresponding to an integrable and a chaotic wedge.

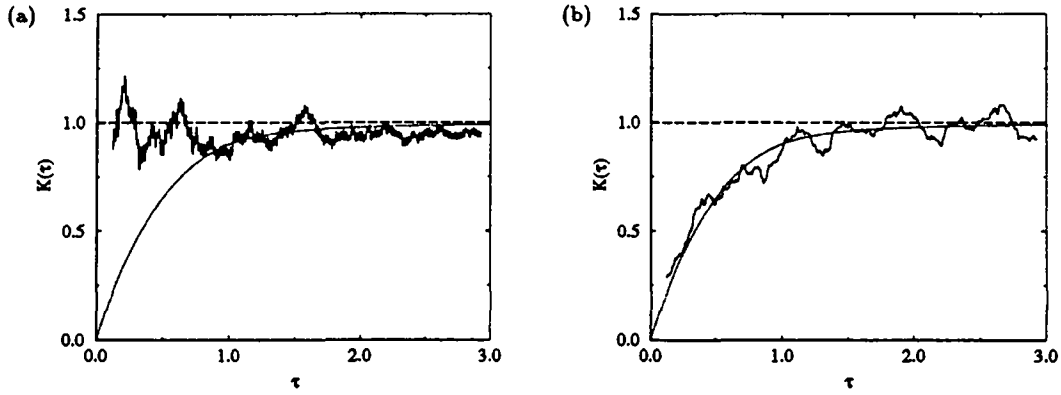


Fig. 4.31. Running average of the spectral form factor $K(\tau)$ for the integrable half wedge (a) and chaotic half wedge (b) with $\beta_R = \pi/3$. Energy average over 200 S matrices with 100 open channels.

All quantities confirm the hypothesis that the ensemble of the scattering matrices is COE, even if the scattering process is not chaotic but just hyperbolic. Hence the eigenphases of the S matrix are giving an equivalent characterization of the system.

4.5.3 Statistics of Level Velocities and Curvatures

We have seen how RMT can be applied to make predictions on single Hamiltonian systems. In this subsection we shall try to characterize a one parameter family of Hamiltonians $\hat{H}(\lambda)$ by the motion of the eigenenergies when the parameter λ is varied. This investigation is motivated by the possibility of a link between high sensitivity of energy levels to a small change of the parameter and the irregularity of the underlying classical dynamics. The physical intuition is that the existence of a multitude of avoided-crossings of levels for classically chaotic systems yields higher dependence on the parameter than for classically integrable systems. This sensitivity should be reflected in the distribution of (rescaled) level velocities $V_n = d\varepsilon_n/d\lambda$ and curvatures $K_n = d^2\varepsilon_n/d\lambda^2$. Moreover, the interest in curvature distributions is raised by the relation with the fluctuations of physical quantities in several mesoscopic quantum systems.

It will be assumed that the underlying classical system is completely chaotic and belongs to the same universality class over the whole range of λ . Thus, we will not consider transitions between integrable and chaotic systems. The turning on of a magnetic field which would change the universality class has to be excluded too. For Hamiltonians $\hat{H}(\lambda) = \hat{H}_1 + \lambda\hat{H}_2$, the equations of motions of the eigenenergies $E_n(\lambda)$ may also be generated by a classical Hamiltonian \mathcal{H} where λ is playing the role of a fictitious time. Using the approach of statistical mechanics on this classical system, one may determine some distributions of classical physical quantities which may be

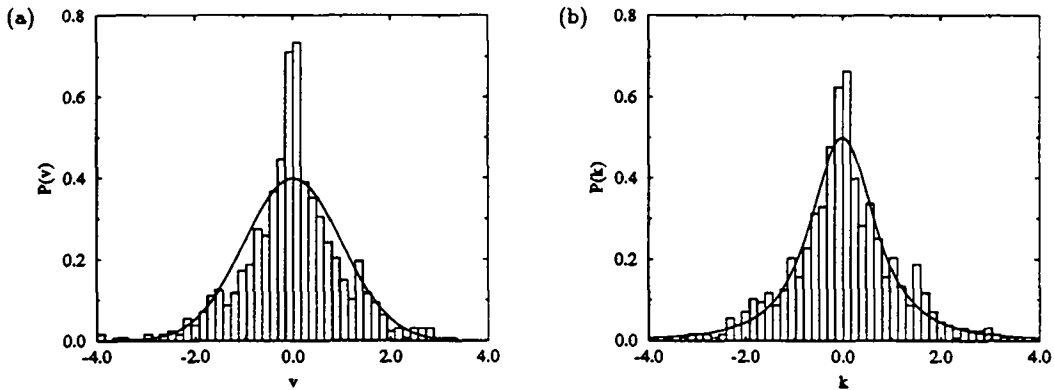


Fig. 4.32. (a) Histogram of the dimensionless velocity distribution from 800 levels of the half wedge with $\beta_R = \pi/3$. The smooth curve represents the normalized Gaussian distribution. (b) Histogram of the dimensionless curvature distribution from the same levels. The smooth curve represents the theoretical distribution.

then translated back in terms of the original quantum system. For instance, one finds that the tail of the level curvature distribution $P(K)$ for systems corresponding to Orthogonal Ensembles (OE) goes like

$$P(K) = \frac{(\pi \bar{\rho} \sigma^2)^2}{2} \frac{1}{|K|^3} + \dots \quad (4.30)$$

where $\bar{\rho}$ is the average density of levels and σ the standard deviation of the Gaussian level velocity distribution (see [GRMN]). Performing the substitution

$$k_n = \frac{1}{\pi \bar{\rho} \sigma^2} K_n \quad (4.31)$$

we obtain a dimensionless curvature. It has been postulated (on the assumption that the formula should be as simple as possible²) that the analytic expression for the full curvature distribution is universal and reads

$$P(k) = \frac{1}{2} \frac{1}{(1+k^2)^{3/2}} \quad (4.32)$$

for systems described by the OE (see [ZD]). Numerical experiments on the kicked-top model are in complete agreement with this distribution. Computations on the stadium billiard revealed a non-universal behavior at small curvatures, which has been attributed to the existence of bouncing ball eigenstates [TaH]. Hence, the curvature distribution has been proposed as a quantitative measure of the existence of scars in a quantum system.

Here we will consider the half wedge with $\beta_R = \pi/3$ and vary the angle around this value. Since we vary a boundary condition, our system is not of the type $\hat{H}(\lambda) =$

²It turns out that the similar analytic expression for the curvature distribution of systems corresponding to Unitary Ensembles is exact [Op].

$\hat{H}_1 + \lambda \hat{H}_2$, but we still expect the predictions to be valid in this case. The classical system is fully chaotic on the range $\beta_R \in]\pi/4, \pi/2[$, so that the other assumptions on the system are verified. As we keep $\beta_L = 0$, we have $\beta = \beta_R$, and we can drop the index R to simplify the notation. The data set is composed of the $N = 800$ lowest energy levels for three values of the wedge angle around $\beta = \pi/3$, from which the discretized derivatives are extracted.

First, we have to check that the distribution of the N level velocities $V_n = d\varepsilon_n/d\beta$ is Gaussian. Then, we may evaluate the variance σ^2 and perform the substitution (4.31) with $\bar{\rho} = N$ on the level curvatures $K_n = d^2\varepsilon_n/d\beta^2$. On Fig. 4.32 (a), we have plotted the distribution of the dimensionless centered reduced velocities

$$v_n = \frac{V_n - \langle V_n \rangle_n}{\sigma} \quad (4.33)$$

where $\langle V_n \rangle_n$ denotes the mean velocity. Comparison with the smooth line which stands for the normalized centered Gaussian distribution with unit variance reveals that the numerical distribution is only approximately Gaussian. Figure 4.32 (b) is a histogram of the curvature distribution computed from 800 dimensionless level curvatures k_n . The agreement with the theoretical distribution (4.32) is rather good, taking into account the small amount of data we possess.

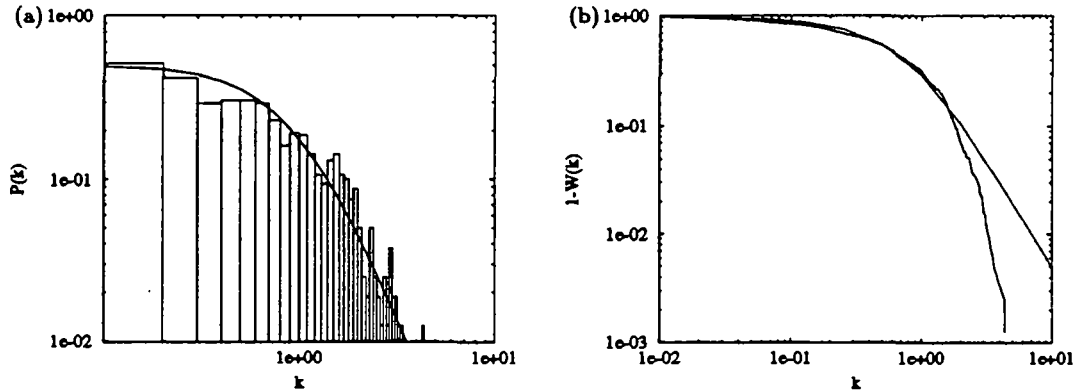


Fig. 4.33. (a) Tail of level curvature distribution $P(k)$ from 800 levels of the half wedge with $\beta_R = \pi/3$. (b) Integrated level curvature distribution $1 - W(k)$ from the same curvatures.

The large curvature behavior of the distribution may be investigated on a double logarithmic plot as in Fig. 4.33 (a). The representation as a histogram does not bring much, since we do not have much data concerning large curvatures. This is why we suggest the use of the integrated distribution $W(k)$, to take advantage of all information contained in the database. For the OE, the analytic expression of $W(k)$ reads

$$W(k) = \int_{-\infty}^k dx P(x) = \frac{1}{2} \left(\frac{k}{\sqrt{1+k^2}} + 1 \right). \quad (4.34)$$

Figure 4.33 (b) is a double logarithmic plot of $1 - W(k)$ for the same data as before. This quantity should behave asymptotically like k^{-2} for large k if RMT apply. Obviously the numerical data does not follow the expected prediction. We have no explanations for this behavior. Whatever the case is, we must admit that this data set is too small to perform significant checks on the large curvature behavior.

4.5.4 Statistics of Phase Velocities and Curvatures

As the system may also be characterized by S matrices, we can repeat the same statistical analysis on the motion of eigenphases of the S matrix when the parameter λ is varied. Moreover, taking averages over several S matrices, we obtain a larger database with a lower computational effort. Since the S matrix is a function of the

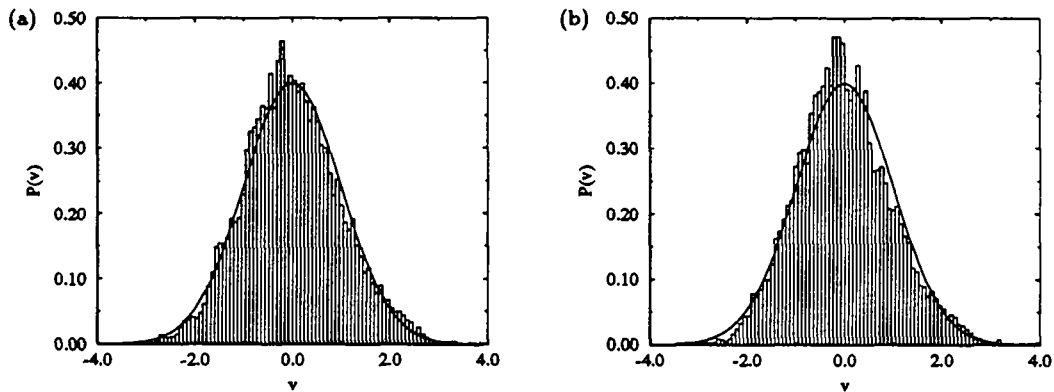


Fig. 4.34. Histograms of distribution of eigenphase velocities $\partial\theta_i/\partial\beta|_E$ (a) and $\partial\theta_i/\partial\varepsilon|_\beta$ (b) for the half wedge with $\beta_R = \pi/3$. Energy average over 200 S matrices with 100 open channels in both cases.

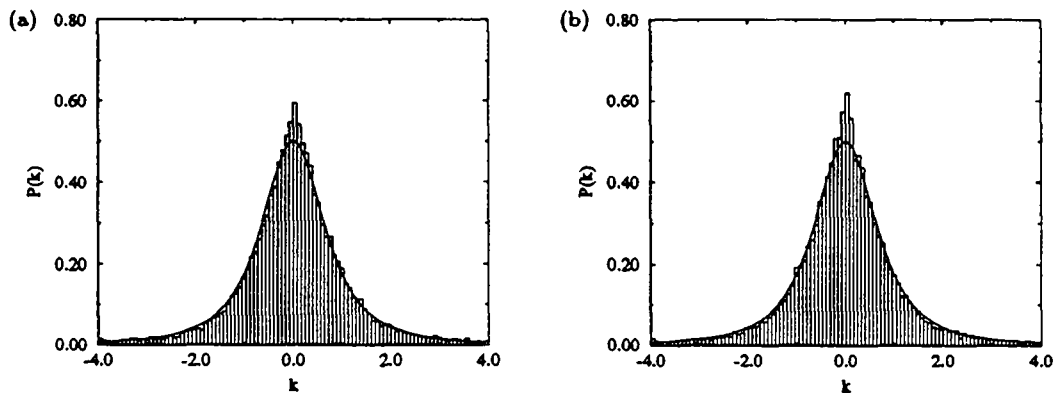


Fig. 4.35. Histograms of distribution of eigenphase curvatures $\partial^2\theta_i/\partial\beta^2|_E$ (a) and $\partial^2\theta_i/\partial\varepsilon^2|_\beta$ (b) for the half wedge with $\beta_R = \pi/3$. Energy average over 200 S matrices with 100 open channels.

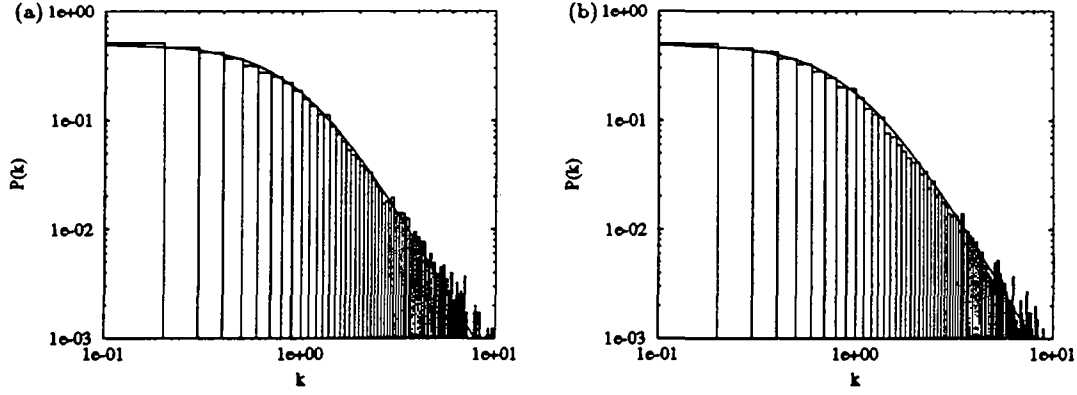


Fig. 4.36. Tails of histograms of distribution of eigenphase curvatures $\partial^2\theta_1/\partial\beta^2|_E$ (a) and $\partial^2\theta_1/\partial\epsilon^2|_\beta$ (b) for the half wedge with $\beta_R = \pi/3$. Energy average over 200 S matrices with 100 open channels.

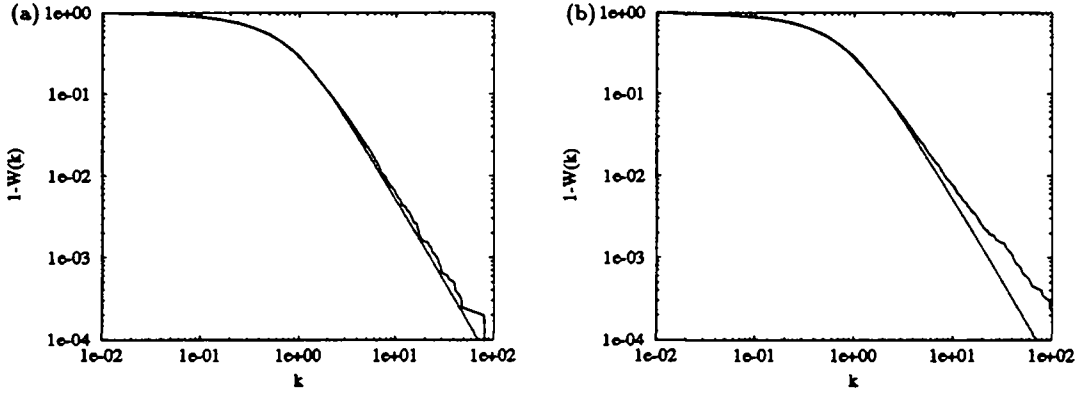


Fig. 4.37. Tails of the integrated distributions $1 - W(k)$ of curvatures $\partial^2\theta_1/\partial\beta^2|_E$ (a) and $\partial^2\theta_1/\partial\epsilon^2|_\beta$ (b) for the half wedge with $\beta_R = \pi/3$. Energy average over 200 S matrices with 100 open channels.

energy as well as the angle, we may vary either parameter separately. We will present here the analysis of the statistics with respect to both parameters.

First we keep the original energy E of the system constant, and let the angle vary. It is important to fix the energy E and not the rescaled energy ϵ , since the unfolding procedure depends explicitly on the angle. The corresponding velocities and curvatures are then $\partial\theta_1/\partial\beta|_E$ and $\partial^2\theta_1/\partial\beta^2|_E$ respectively. Then we shall keep the value of the angle constant and let ϵ change. This time we have to consider the rescaled energy, since we want to take averages over S matrices at different energies to increase our database. This yields the velocities $\partial\theta_1/\partial\epsilon|_\beta$ and curvatures $\partial^2\theta_1/\partial\epsilon^2|_\beta$.

Figure 4.34 represents the distributions of the centered reduced eigenphase velocities, which we may verify to be well approximated by a centered Gaussian with unit variance in both cases. Using the variances of both original distributions and setting

$\bar{\rho} = \frac{\Lambda}{2\pi}$, we may then construct the respective histograms of dimensionless curvatures, which are represented in Fig. 4.35. The agreement with the postulated distribution is generally good except around the origin. However, the excess at small curvatures is much smaller than in the case of the stadium billiard. This observation is compatible with the suggestion to use the curvature distribution as an indicator of scarring, since the system does not possess orbits of the “bouncing ball” type. Nevertheless it remains unclear whether this small excess around $k = 0$ corresponds to the existence of scars in this model or not.

In order to investigate the large k behavior of the distribution, we have plotted the histograms (see Fig.4.36) and the graphs of $1 - W(k)$ (see Fig.4.37) as double logarithmic plots. Comparison of both representations clearly demonstrates the superiority of the second one. Whereas the agreement with the prediction is good on both histograms, we notice a bigger deviation for the curvatures computed with respect to variation of the energy.

The above results seem to confirm the universal behavior of the long tail curvature distribution. However, the number of systems which have been investigated is still too small to draw serious conclusions. It would be interesting to check the behavior at small curvatures on a model which does not present any scarring, in order to make clear the signification of the deviations observed here.

4.5.5 Statistics of Eigenvalues of the time delay matrix

The last statistical analysis is performed on the velocities $\tau_l = \partial\theta_l/\partial E|_{\beta}$. Up to a factor $1/\Lambda$, these velocities are the eigenvalue of the time delay matrix

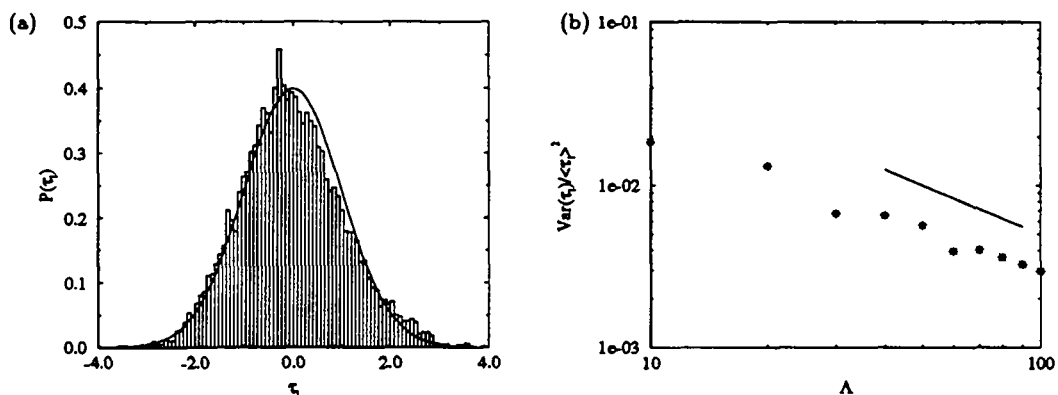


Fig. 4.38. (a) Histogram of the distribution of velocities τ_l for the half wedge with $\beta_R = \pi/3$ and $\Lambda = 100$. (b) Plot of the dimensionless quantity $\text{Var}(\tau_l)/\langle \tau_l \rangle^2$ as a function of Λ for the same half wedge. The solid line goes like $1/\Lambda$.

$$T(E) = \frac{1}{i\Lambda} S^\dagger \frac{\partial S}{\partial E}, \quad (4.35)$$

and their average corresponds to the Wigner delay time (3.75)

$$\tau(E) = \langle \tau_l \rangle_l = \frac{1}{\Lambda} \sum_{l=1}^{\Lambda} \left. \frac{\partial \theta_l}{\partial E} \right|_{\beta}. \quad (4.36)$$

As one can see on Fig.4.38 (a), the centered reduced velocity distribution is of the Gaussian type as well. It is interesting to look at the behavior of the variance of this distribution as a function of the number of open channels.

For systems presenting chaotic scattering, it has been shown that the dimensionless quantity $\text{Var}(\tau_l)/\langle \tau_l \rangle^2$ should behave like $8 \log \Lambda/\Lambda^2$ when $\Lambda \gg 1$ (see [DoS]). In Fig.4.38 (b) we can see that the decay is much slower for the half wedge, in which case scattering is only hyperbolic. The solid line in the figure stands for a function decreasing like $1/\Lambda$. Nevertheless, since $\langle \tau_l \rangle \propto \Lambda^{1/3}$ the width of the distribution is becoming narrower when the energy is increased. As a consequence, one can replace the factors τ_l in (4.29) by the average τ , and obtain

$$\sum_{n=1}^{\infty} \delta(E - E_n) = \tau(E) \sum_{l=1}^{\Lambda} \delta_{2\pi}(\theta_l(E)) \quad \Lambda \gg 1 \quad (4.37)$$

a much simpler semiclassical relation between the eigenenergy density and the eigenphase density.

Discussion

The first part of this thesis has been devoted to classical mechanics, in order to become acquainted with the basic features of the wedge billiard. Recall that this model falls into the class of “inclined billiards” where the motion between successive bounces is not free, and hence departs from Euclidean billiards. The structure of the integrable phase space has been explained in the context of continuous as well as discrete dynamics. A new set of coordinates which play the role of angle-action variables for the map is given explicitly. Special attention has been drawn on integrable segments of trajectories, and on their effect on the statistical behaviors. Although the integrable wedges have been solved and several properties of the fully chaotic ones have been computed, very little is known about the wedges with mixed dynamics. Our qualitative description of the pre-images of the corner is a first attempt toward understanding mixed systems, or at least separating phase space in regions of integrable and chaotic motion. We could prove that iterates of the bouncing map are more regular when the angles are divisors of π , but we could not give a quantitative measure of the influence of the singularities. The isomorphism with the one dimensional system of ordered particles raises very interesting questions, such as for instance the relationship between statistical properties of the classical isomorphic systems, or the connection between the quantum associated systems. Here we have just shown that the dynamics and the singularities of both classical systems are in one to one correspondence.

In the second part, we have extended the scattering approach to quantization to include Hamiltonians with binding potential. The general scattering formalism has been applied to the wedge billiard both analytically and numerically. This approach has a few advantages. The quantization condition is formulated as a secular equation which requires that at an eigenenergy the spectrum of the associated S matrix includes the value 1. It is not sensitive to the regularity of the dynamics and is valid for integrable, chaotic as well as mixed systems. Restricting the S matrix to the space of opened channels, and proceeding with the semiclassical approximation, we were able to derive not only the Gutzwiller trace formula for chaotic and integrable systems, but also to calculate the leading terms for the smooth level density. The

fundamental step in the semiclassical approximation is the calculation of $\text{Tr}S^n$ in terms of periodic orbits of the classical Poincaré Scattering Map. We could test the accuracy of this approximation numerically, and found a very good agreement with the quantum data. The scattering approach provides a very convenient numerical tool. Thousands of eigenvalues of the wedge billiard have been computed with a very high accuracy. Using this database, we have been able to check various aspects of the semiclassical theory, which were not accessible to previous authors who had to perform their analysis in terms of numerical spectra which were poorer both in accuracy and number of levels. We could for instance test the role of families of periodic orbits which converge to a limit orbit.

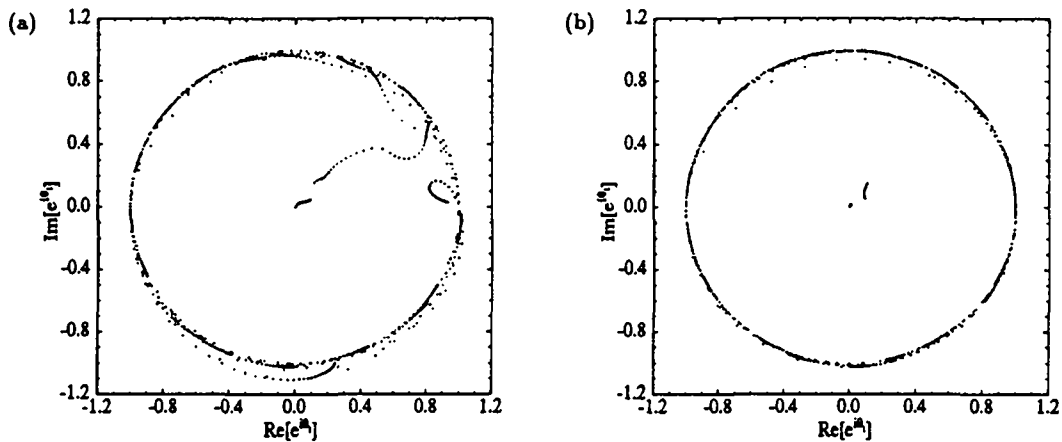


Fig. 4.39. Parametric representations of the 25 first eigenphases $e^{i\theta_j}$ as a function of the energy for the half wedge with $\beta_R = \pi/3$ near a threshold. The energy parameter runs from 10 units of the mean level spacing below the 21st threshold to 10 units above. (a) Energy interval below the threshold. The energy difference between the dots is chosen to decrease exponentially. (b) Energy interval above the threshold. Here the energy difference between the dots increases exponentially.

However, there are a few points which need further elucidation. The quantization condition, namely that an eigenvalue occurs whenever the $S(E)$ matrix has 1 as an eigenvalue, is well defined for any finite truncation of the extended S matrix, but may be problematic when the full S operator is considered. The extended S matrix is not unitary, and at threshold energies it is not even analytic in the energy E . We observed numerically that, between thresholds, the spectrum of the extended S matrix is composed of A eigenvalues which are in the close vicinity of the unit circle, and the rest, which are concentrated near 0. As a threshold is approached, the absolute value of one of the eigenvalues near 0 starts to increase and at the threshold energy it reaches the unit circle by the vicinity of 1. This occurrence of the value 1 in the spectrum does not signal the appearance of a new eigenenergy of the system. Rather, it is a consequence of the opening of a new channel. In Fig. 4.39 we trace the dependence of the eigenvalues of the S matrix near a threshold. We are not able to provide an explanation for the observed behavior, but it seems to be universal

(see for instance a similar figure in [ScS]), and therefore essential for the complete understanding of the scattering approach.

Our next goal was to give a characterization of the quantum systems in terms of stationary quantities. Using the data sets provided by the scattering method we have performed several statistical analyses on the eigenvalues of the Hamiltonian H and on the eigenphases of the S matrix. We have seen that actually both quantities seem to deliver the same statistical information on the system. We also have looked at the way these quantities are changing when a parameter is varied and the underlying classical dynamics remains chaotic. We could not only check that the tail of the curvature distributions follows the predictions of RMT, but also test the global shape of the distributions. We observed that the formula proposed by Zakrzewski *et al.* [ZD] fits the data well, except in the small curvatures region where the deviation is larger. Beyond the universal behavior, the small curvature distribution contains information on the amount of eigenstates which are less sensitive to the variation of the parameter. Hence it provides a new characterization of the system. It would be worth performing the same kind of analysis on integrable systems first, to see what can be learned in this way. It is clear that the distribution of curvatures will be much narrower for integrable systems, since they do not show the feature of avoided-crossings of levels. The investigation could then be repeated on mixed systems, for which only standard level statistics has been done (see for instance [Ro]). This may lead to an interesting classification of quantum systems.

Appendices

A.1 Local Properties of the Bouncing Map near Corners

A.1.1 Continuity of P^σ for Euclidean Billiards

In this appendix, we show that there may exist a power $\sigma \in \mathbb{N}^*$ such that P^σ (the σ th iterate of the bouncing map P) is continuous for a set of particular "corners" made by edges which are smooth curves. We perform our computations in the Oxy plane, where the trajectories between two collisions are straight lines.

First we must describe a "corner". We want to find corner angles for which elastic collision at the vertex can be defined by equating the limiting trajectories as in the case of straight line edges. Thus we assume that the corner angle is less than π .

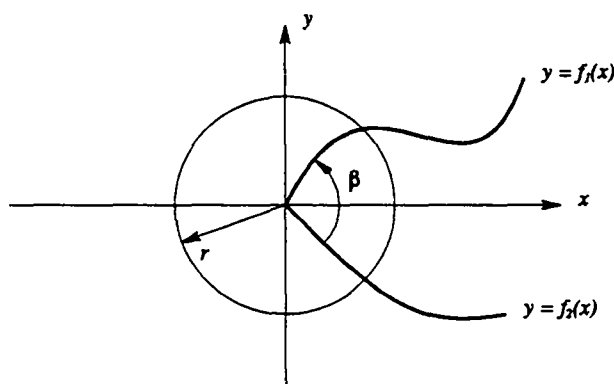


Fig. A.40. Sketch of the bounding edges of a typical corner with angle β .

We construct a most general corner as in Fig. A.40. Without loss of generality we can put it at the origin of the Oxy plane. We assume that there is some distance $r > 0$ such that the edges meeting at the corner may be described by two functions $y = f_1(x)$ and $y = f_2(x)$, $0 \leq x \leq r$ with $f_1(0) = f_2(0) = 0$ and $f_1'(0) \neq f_2'(0)$. We assume that f_1 and f_2 are twice continuously differentiable on $0 \leq x \leq r$, and that they may be approximated by Taylor series

$$f_j(x) = f_j'(0)x + \frac{f_j''(0)x^2}{2} + o(x^2), \quad 1 \leq j \leq 2, \quad (\text{A.38})$$

on this interval. We also assume that $f_j''(x)$ does not change sign on this interval, though it may be zero. Finally we note that

$$\tan \beta = \frac{f_1'(0) - f_2'(0)}{1 + f_1'(0)f_2'(0)}. \quad (\text{A.39})$$

In discussing collisions in this corner, we assume that the billiard starts on a straight line trajectory $y = ax + \varepsilon$ within a distance smaller or equal to r from the origin. We shall consider two trajectories, one with $\varepsilon > 0$ striking the edge $y = f_1(x)$ first, close to the corner and the other with $\varepsilon < 0$ striking $y = f_2(x)$ first. We then let ε tend to 0 and compare both outgoing trajectories. We shall find the angles β for which the limits of the two reflected trajectories are the same as the positions on the first edge tend to the corner.

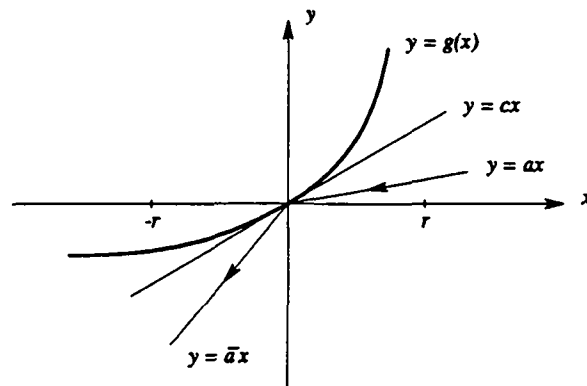


Fig. A.41. Collision of a billiard with a single curved boundary.

First we have to discuss single collisions of a billiard with a curved surface. We consider a collision with the boundary $y = g(x)$, where g is continuously twice differentiable on some interval $-r \leq x \leq r$. We have $g(0) = 0$,

$$g(x) = g'(0)x + \frac{g''(0)x^2}{2} + o(x^2) \quad (\text{A.40})$$

on $-r \leq x \leq r$. The collision occurs at the origin as in Fig. A.41.

We prove an obvious lemma about straight edges and then extend it to curved edges.

Lemma 1 *After colliding with the boundary $y = cx$, the trajectory $y = ax$ is given by $y = \bar{a}x$, with*

$$\bar{a} = \frac{2c - a + ac^2}{1 - c^2 + 2ac}. \quad (\text{A.41})$$

Proof. We write γ and $\bar{\gamma}$ the angles made by the incoming and reflected trajectories with the Ox axis, and β the angle between the boundary and the same axis, and so

$$\tan(\gamma) = a, \quad \tan(\bar{\gamma}) = \bar{a} \quad \text{and} \quad \tan(\beta) = c. \quad (\text{A.42})$$

The elasticity of the collision is given by the simple relation between the angles

$$\gamma - \beta = \beta - \bar{\gamma}. \quad (\text{A.43})$$

This can be expressed via a , \bar{a} and c as

$$\bar{a} = \tan(2\beta - \gamma) = \frac{2 \tan(\beta) - \tan(\gamma) + \tan(\gamma) \tan^2(\beta)}{1 - \tan^2(\beta) + 2 \tan(\gamma) \tan(\beta)} = \frac{2c - a + ac^2}{1 - c^2 + 2ac} \quad (\text{A.44})$$

which brings the conclusion. \square

Now consider the trajectory $y = ax + \varepsilon$ with $|\varepsilon| \ll 1$ striking the boundary $y = g(x)$ introduced above. We assume $g'(0) \equiv c \neq a$ so that the trajectory meets the boundary for the first time near the origin. The following lemma shows that the subsequent trajectory is close to the one with $\varepsilon = 0$.

Lemma 2 *After colliding with the smooth boundary $y = g(x)$, the trajectory $y = ax + \varepsilon$, $|\varepsilon| \ll 1$ is given by $y = \bar{a}x + \tilde{\varepsilon}$ where $\bar{a} = \bar{a} + O(\varepsilon)$ (with \bar{a} from equation (A.41)) and $\tilde{\varepsilon} = O(\varepsilon)$.*

Proof. Let the intersection of the incoming trajectory and the boundary $y = g(x)$ be (x_1, y_1) and let ε be small enough that $|x_1| \leq r$. Then $ax_1 + \varepsilon = g(x_1)$. Thus

$$\varepsilon = (c - a)x_1 + \frac{g''(0)x_1^2}{2} + o(x_1^2) \quad (\text{A.45})$$

and by standard reversion of series we get

$$x_1 = \frac{\varepsilon}{c - a} - \frac{g''(0)\varepsilon^2}{2(c - a)^3} + o(\varepsilon^2). \quad (\text{A.46})$$

So $x_1 = O(\varepsilon)$ and $y_1 = ax_1 + \varepsilon = O(\varepsilon)$. The slope of the boundary at the point of intersection is then

$$g'(x_1) = c + g''(0)x_1 + o(x_1) = c + \frac{g''(0)\varepsilon}{c - a} + o(\varepsilon) = c + O(\varepsilon). \quad (\text{A.47})$$

(Actually we have calculated more terms than necessary, but these computations will be useful later.) The conclusion of the lemma is then obtained using lemma 1 and noting that for $t \neq 0$, $(s + O(\varepsilon))/(t + O(\varepsilon)) = s/t + O(\varepsilon)$. \square

Note that the argument still holds for the case $c = a$ if the second derivative and ε have same sign, and the third derivative exists on the interval $-r \leq x \leq r$. Thus

$$x_1^2 = \frac{2\varepsilon}{g''(0)} + O(\varepsilon^3) \quad (\text{A.48})$$

and all corrections are of order $O(\varepsilon^{3/2})$. This case corresponds to a concave boundary. If $c = a$ and the second derivative and ε have opposite signs, there is no intersection

with this edge. This corresponds to a convex boundary. If finally the second derivative vanishes, we can only give a conclusion by looking at the behavior of higher derivatives when they exist.

We now consider our original problem of the trajectory $y = ax + \varepsilon$, $|\varepsilon| \ll 1$ close to a corner as in Fig. A.40. We proceed in the same way as for one boundary by first considering straight boundaries and then more general boundaries. Thus we consider the trajectory $y = ax + \varepsilon$, $|\varepsilon| \ll 1$ and two straight edges $d_1 : y = f_1(x) = c_1x$ and $d_2 : y = f_2(x) = c_2x$ with $c_1 > a > c_2$. It is obvious that the particle alternatively hits d_1 and d_2 until it leaves the corner formed by these two boundaries and finally hits some other boundary. The trajectory is then a sequence of straight line segments between d_1 and d_2 . The slope of the k^{th} segment of trajectory is s_k (with $s_0 = a$). This k^{th} segment, starts on $d_{i(k)}$, where

$$i(k) = \begin{cases} (k+1) \bmod 2 + 1 & \text{if } \varepsilon > 0 \\ (k+1) \bmod 2 & \text{if } \varepsilon < 0. \end{cases} \quad (\text{A.49})$$

From lemma 1, the slopes are defined recursively by

$$\begin{aligned} s_0 &= a \\ s_{k+1} &= \frac{2c_{i(k+1)} - s_k + s_k c_{i(k+1)}^2}{1 - c_{i(k+1)}^2 + 2s_k c_{i(k+1)}} \quad 0 \leq k \leq n-1. \end{aligned} \quad (\text{A.50})$$

Here n is the number of collisions before the particle strikes another part of the system.

Now we consider the same incoming trajectory and, instead of d_1 and d_2 two smooth functions $f_1(x)$ and $f_2(x)$ intersecting at the origin as in Fig. A.40, such that $f_1'(0) = c_1$ and $f_2'(0) = c_2$. To show that the subsequent trajectory is close to the one with straight edges when $\varepsilon \rightarrow 0$, we first have to prove that the particle also hits alternatively f_1 and f_2 . It is obvious for convex edges (see Fig. A.41) that the particle cannot strike successively twice the same edge.

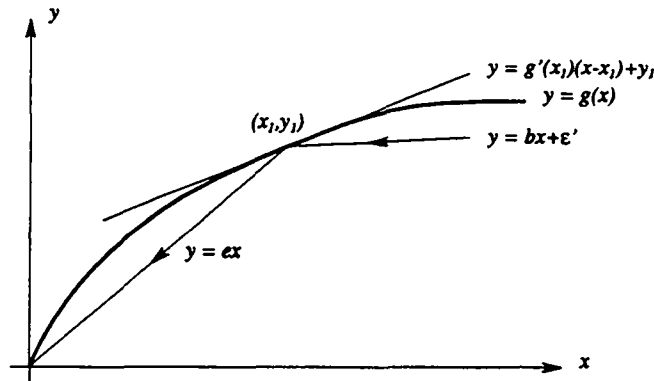


Fig. A.42. Collision of a billiard with a concave boundary

The next lemma shows that it cannot happen with concave edges either when ε tends to zero.

Lemma 3 Consider the edge $y = g(x)$ on \mathbb{R}^+ with $g(0) = 0$, $g'(0) = c > 0$ and $g''(x) < 0$ as in Fig. A.42. $\forall a < c, \exists \varepsilon_a$ such that for $\varepsilon \in]0, \varepsilon_a[$ the trajectory $y = ax + \varepsilon$ with $|\varepsilon| \ll 1$ cannot strike successively twice the edge $g(x)$.

Proof. The idea of the proof is the following. We consider the trajectory $y = ax + \varepsilon$ with $|\varepsilon| \ll 1$ striking the edge g at (x_1, y_1) close to the origin. We compute the slope b of the trajectory $y = bx + \varepsilon'$ which after one reflection at the point (x_1, y_1) meets exactly the origin as in Fig. A.42. Of all the trajectories striking at (x_1, y_1) , only trajectories with slopes greater than b can strike the edge g successively twice. For ε small enough the slope of the trajectory between (x_1, y_1) and $(0, 0)$ can be written

$$e = \frac{y_1}{x_1} = c + \frac{g''(0)\varepsilon}{2(c-a)} + o(\varepsilon), \quad (\text{A.51})$$

since equation (A.46) is still valid and $y = g(x_1)$. The slope of the tangent to the edge in (x_1, y_1) is given by

$$g'(x_1) = c + \frac{g''(0)\varepsilon}{c-a} + o(\varepsilon). \quad (\text{A.52})$$

As the system is time reflection invariant, we can use the same calculation as in lemma 2 to compute the slope b . Evaluating the correction of order $O(\varepsilon)$ we get

$$b = c + \frac{3}{2} \frac{g''(0)\varepsilon}{c-a} + o(\varepsilon) \quad (\text{A.53})$$

which clearly shows that $\lim_{\varepsilon \rightarrow 0}(b) = c$. Thus if $a < c$ it is possible to find an $\varepsilon_a \ll 1$ such that $b(\varepsilon) > a$ for $\varepsilon \in]0, \varepsilon_a[$. \square

Since we know that for very small ε the trajectory $y = ax + \varepsilon$ is striking alternatively both edges f_1 and f_2 , we are able to prove in the following lemma that this trajectory is not so different from the one striking d_1 and d_2 .

Lemma 4 Consider the incoming trajectory $y = ax + \varepsilon$ with $|\varepsilon| \ll 1$, and two functions $f_1(x)$ and $f_2(x)$ twice continuously differentiable such that $f_1'(0) = c_1$, $f_2'(0) = c_2$, $c_1 > a > c_2$ and crossing at the origin as in Fig. A.40. After k collisions with the boundary formed by f_1 and f_2 , the trajectory is given by $y = a_k x + \varepsilon_k$, where $a_k = s_k + O(\varepsilon)$ (with s_k from equation (A.50)) and $\varepsilon_k = O(\varepsilon)$.

Proof. We shall prove this lemma by induction on the number of collisions k . For $k = 1$ we must show that the result is true for the first reflection. This has already been done in lemma 2. For the second step of the induction, we have to show that if the result is true for the k^{th} reflection it will also be true for the $k + 1^{\text{th}}$.

We define the series x_k, y_k as the coordinates of the point where the k^{th} collision happens, and \bar{c}_k as the slope of the boundary $f_{i(k)}$ at this point. Assuming that the conclusion is valid for k , we have

$$a_k = s_k + O(\varepsilon) \text{ and } \varepsilon_k = O(\varepsilon). \quad (\text{A.54})$$

So we can compute

$$\begin{aligned} x_{k+1} &= \frac{\varepsilon_k}{c_{i(k)} - s_k + O(\varepsilon)} + o(\varepsilon_k) = O(\varepsilon) \\ y_{k+1} &= a_k x_{k+1} + \varepsilon_k = O(\varepsilon) \end{aligned} \quad (\text{A.55})$$

and

$$\bar{c}_{k+1} = c_{i(k+1)} + f''_{i(k+1)}(0)x_{k+1} + o(x_{k+1}) = c_{i(k+1)} + O(\varepsilon). \quad (\text{A.56})$$

Repeating the computations of lemma 2, we obtain

$$a_{k+1} = \frac{2\bar{c}_{k+1} - a_k + a_k \bar{c}_{k+1}^2}{1 - \bar{c}_{k+1}^2 + 2a_k \bar{c}_{k+1}} = s_{k+1} + O(\varepsilon) \quad (\text{A.57})$$

and

$$\varepsilon_{k+1} = y_{k+1} - a_{k+1}x_{k+1} = O(\varepsilon), \quad (\text{A.58})$$

which completes the induction proof of the lemma. \square

Notice that although the series x_k , y_k , \bar{c}_k , a_k and ε_k are computable $\forall k \in \mathbb{N}^*$, they only make sense for $k \leq n$. It should be clear to the reader that the sequence s_k takes different values according to the sign of ε , i.e. according to which side the particle first strikes. Thus we shall rewrite it as s_k^+ for $\varepsilon > 0$ and as s_k^- for $\varepsilon < 0$. Remember that when $\varepsilon = 0$ the collision is not defined yet, because the particle hits the top of the corner where the normal to the boundary is not uniquely defined.

The subject of the next lemma is to show that the collision of the trajectory $y = ax + \varepsilon$ with $\varepsilon = 0$ striking the corner on the top can be defined by equating the limiting trajectories with $\varepsilon \neq 0$ iff the angle β made by f_1 and f_2 at the origin is a divisor of π .

Lemma 5 *Consider the incoming trajectory $y = ax + \varepsilon$ with $|\varepsilon| \ll 1$ and two functions f_1, f_2 for which the assumption of lemma 4 holds. Iff in addition $\exists n \in \mathbb{N}^*$ such that $\beta = \pi/n$ then*

$$\lim_{\varepsilon \rightarrow 0^+} a_n = \lim_{\varepsilon \rightarrow 0^-} a_n. \quad (\text{A.59})$$

Thus the collision for $\varepsilon = 0$ can be defined by equating the limit from either side, since they are equal.

Proof. It is obvious from lemma 4 and from the definition of s_k^+ and s_k^- that

$$\lim_{\varepsilon \rightarrow 0^+} a_k = s_k^+ \text{ and } \lim_{\varepsilon \rightarrow 0^-} a_k = s_k^-. \quad (\text{A.60})$$

It has been proved in the the previous section that $s_k^+ = s_k^-$ iff $\exists n \in \mathbb{N}^*$ such that $\beta = \pi/n$. This n represents the number of collisions before the particle hits some

other part of the boundary. Thus the sequences s_k^+ and s_k^- are well defined for $k = n$ and the conclusion is immediate. \square

In the next proposition, we just rewrite the result of the last lemma in terms of the bouncing map P which is more conventional for billiards.

Proposition 1 Consider a corner of a Euclidean billiard in two dimensions with a piecewise twice continuously differentiable boundary. $\exists \sigma$ such that the map P^σ is continuous at the top of the corner iff the angle is a divisor of π . For $\beta = \pi/n$, $n \in \mathbb{N}^*$, P^{n+1} is continuous at the vertex.

Proof. This is a straight consequence of lemma 5. As this formulation refers to the map P , and not to the trajectories between two bounces, as above, it is necessary to consider $n + 1$ iterations of the map to get the conclusion. \square

A.1.2 Differentiability of P^σ for Euclidean Billiards

So we know how to define orbits colliding at the top of the corner when the angle is a divisor of π . But in the case of periodic orbits we cannot determine their stability, since we do not know whether the map P^σ is differentiable or not. In the next proposition we prove that P^σ is differentiable at the vertex when $\beta = \pi/n$ and n is even. For odd n 's, we show that P^σ is differentiable if the boundary satisfies an additional geometric condition.

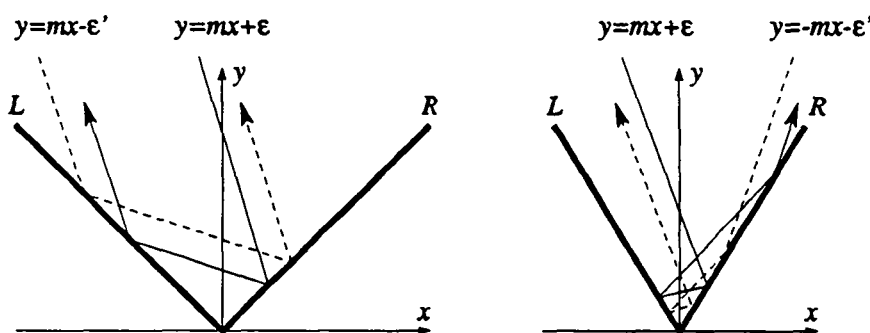


Fig. A.43. Symmetry with respect to time inversion for $\beta = \pi/2$ and $\beta = \pi/3$.

The difference between both cases can be understood with the help of Fig. A.43, in the limit $\epsilon \rightarrow 0$. For even n 's, the orbit $y = ax + \epsilon$ striking the edge R first is the time reversal of $y = ax - \epsilon'$ which strikes the edge L first, whereas for odd n 's, the orbit $y = ax + \epsilon$ is the time reversal of $y = -ax - \epsilon'$ which strikes the same edge.

To prove the proposition we need the next lemma about the linearization of the the map P^σ at the vertex of a corner.

Lemma 6 *Both linearizations (for $\varepsilon \rightarrow 0^\pm$) of P^σ at the vertex of a corner verifying the assumptions of proposition 1 equal their inverse.*

Proof. First we compute the linearization of P for one single collision as in Fig. A.41. The straight line trajectory $y = ax + \varepsilon$ before the collision is characterized by (a, ε) , and the one after the collision by $(\bar{a}, \bar{\varepsilon})$. In these coordinates, the linearization of P is given by the matrix $\partial(\bar{a}, \bar{\varepsilon})/\partial(a, \varepsilon)$. We keep the same notations as in lemma 2. In addition we define $d \equiv g''(0)$. Using equation (A.47), and evaluating the terms of order $O(\varepsilon)$ we get

$$\bar{a} = \frac{2g'(x_1) - a + ag'(x_1)^2}{1 - g'(x_1)^2 + 2ag'(x_1)} \quad (\text{A.61})$$

$$= \frac{2c - a + ac^2}{1 - c^2 + 2ac} + \frac{2(1 + a^2)(1 + c^2)d\varepsilon}{(c - a)(1 - c^2 + 2ac)^2} + o(\varepsilon) \quad (\text{A.62})$$

and

$$\bar{\varepsilon} = y_1 - \bar{a}x_1 = -\frac{(1 + c^2)\varepsilon}{(1 - c^2 + 2ac)} + o(\varepsilon). \quad (\text{A.63})$$

This determines the linearization of P when ε tends to zero

$$\left. \frac{\partial(\bar{a}, \bar{\varepsilon})}{\partial(a, \varepsilon)} \right|_{\varepsilon=0} = \begin{pmatrix} -s^2 & t \\ 0 & -s \end{pmatrix}. \quad (\text{A.64})$$

with

$$s = \frac{1 + c^2}{1 - c^2 + 2ac} \quad \text{and} \quad t = \frac{2d(1 + a^2)(1 + c^2)}{(c - a)(1 - c^2 + 2ac)^2}. \quad (\text{A.65})$$

We write the linearizations of P^σ at the vertex as $D_{\text{even/odd}}^\pm(a)$, where the signs \pm stand for the sign of ε before the limit is taken, a for the slope of the incoming trajectory and *even/odd* for the oddity of n . As products of σ matrices of the form (A.64), all $D_{\text{even/odd}}^\pm(a)$ keep this form. So we get the following relation between the partial derivatives

$$\left| \frac{\partial \hat{a}_{\text{even/odd}}^\pm}{\partial a} \right| = \left| \frac{\partial \hat{\varepsilon}_{\text{even/odd}}^\pm}{\partial \varepsilon} \right|^2 \quad (\text{A.66})$$

where this time \hat{a}^\pm means the slope after σ reflections at the vertex. If n is even the outgoing trajectory is reflected on itself, whereas if n is odd it is reflected according to the bisector of the angle β . Thus we have

$$\frac{\partial \hat{a}_{\text{even}}^\pm}{\partial a} = 1 \quad \text{and} \quad \frac{\partial \hat{a}_{\text{odd}}^\pm}{\partial a} = -1. \quad (\text{A.67})$$

As $\varepsilon_{\text{even}}$ and $\hat{\varepsilon}_{\text{even}}$ have opposite sign, and ε_{odd} and $\hat{\varepsilon}_{\text{odd}}$ have same sign, we obtain

$$\frac{\partial \hat{\varepsilon}_{\text{even}}^{\pm}}{\partial \varepsilon} = -1 \quad \text{and} \quad \frac{\partial \hat{\varepsilon}_{\text{odd}}^{\pm}}{\partial \varepsilon} = 1. \quad (\text{A.68})$$

Using (A.66), we get

$$D_{\text{even}}^{\pm}(a) = \begin{pmatrix} 1 & \partial \hat{a}^{\pm} / \partial \varepsilon \\ 0 & -1 \end{pmatrix} \quad \text{and} \quad D_{\text{odd}}^{\pm}(a) = \begin{pmatrix} -1 & \partial \hat{a}^{\pm} / \partial \varepsilon \\ 0 & +1 \end{pmatrix}, \quad (\text{A.69})$$

and we can see that $D_{\text{even/odd}}^{\pm}(a) = [D_{\text{even/odd}}^{\pm}(a)]^{-1}$. \square

Proposition 2 Consider a corner making an angle $\beta = \pi/n$ such that P^{n+1} is continuous at the vertex. We distinguish two cases :

- If n is even the map P^{n+1} is differentiable.
- If n is odd the map P^{n+1} is differentiable if the boundaries have same curvature at the vertex.

Proof. Using the symmetry under time inversion and lemma 6, the case n even is trivial :

$$D_{\text{even}}^{+}(a) = [D_{\text{even}}^{-}(a)]^{-1} = D_{\text{even}}^{-}(a). \quad (\text{A.70})$$

The case n odd requires some more attention. As mentioned before, the orbit $y = ax + \varepsilon$ is the time reversal of $y = -ax - \varepsilon'$ in the xy coordinates with the y axis on the bisector of β . Thus we have

$$D_{\text{odd}}^{+}(a) = [D_{\text{odd}}^{-}(-a)]^{-1}. \quad (\text{A.71})$$

This cannot lead to the determination of the derivative of P^{n+1} at the vertex since both trajectories are striking the same edge. But if the corner is symmetric with respect to the bisector of β , then the trajectory $y = -ax - \varepsilon'$ is the symmetric of $y = ax - \varepsilon'$. We require the same curvature of the edges at the vertex, which means accordance of the two first derivatives, for no higher derivatives of the boundaries appear in (A.64). Under this assumption

$$\frac{\partial \hat{a}_{\text{odd}}^{\pm}(a)}{\partial \varepsilon'} = -\frac{\partial \hat{a}_{\text{odd}}^{\pm}(-a)}{\partial \varepsilon'}, \quad (\text{A.72})$$

and hence

$$[D_{\text{odd}}^{-}(-a)]^{-1} = D_{\text{odd}}^{-}(a), \quad (\text{A.73})$$

which leads to the conclusion. \square

Proposition 3 Consider a corner making an angle $\beta = \pi/n$ such that P^{n+1} is continuous at the vertex. If the boundaries are symmetric with respect to the bisector of the angle, then the map P^{n+1} is differentiable.

Proof. This is a straight consequence of proposition 2, since in this case both boundaries have the same curvature. \square

Notice that when $\beta = \pi/2$, one can construct corners such that P^3 is m times differentiable at the vertex. Consider a boundary given by an even function $f(x)$, such that f is only C^{m+1} at $x = 0$ (see Fig. A.44).

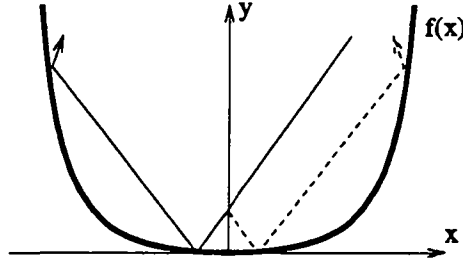


Fig. A.44. Corner with angle $\pi/2$ such that P^3 is more than C^1

The dynamics in the corner of the “half billiard” determined by the vertical axis and the right (or left) part of the boundary is completely equivalent to the one of the “entire billiard”. Moreover, it has been shown that the flow of Euclidean billiards in angles π/n formed by straight lines has no singularities at the vertex [ZK].

A.1.3 Generalization to the Wedge Billiard

The trajectories of the wedge billiard between two collisions are inverted parabola. To make use of the previous proofs, we will parameterize these parabola as

$$y = ax + \varepsilon - \frac{a^2 + 1}{4(1 - \varepsilon)} x^2 \quad (\text{A.74})$$

so that the straight line $y = ax + \varepsilon$ represents the tangent to the trajectory at its crossing with the vertical axis.

The first step is to check that the sequence of collisions with both boundaries near to the corner still alternates. As the trajectories are simple parabola, it is not hard to adapt the proof of lemma 4 to show that there exists a similar ε_a such that the trajectory does not strike successively twice the same edge.

Once this is done, the continuity of the power of the map P follows immediately. More difficult is to verify that the form (A.64) still holds for the derivative in this case. In order to render the proof more general, we suppose, as before, that each side is given by a function which is continuously twice differentiable around the corner. This is obviously the case for the wedge where $y = cx$. Furthermore, the second derivative d vanishes for straight edges. We will decompose the computation of the linearization of the map $(a, \varepsilon) \mapsto (\bar{a}, \bar{\varepsilon})$ in several steps (see Fig.A.45). First, given

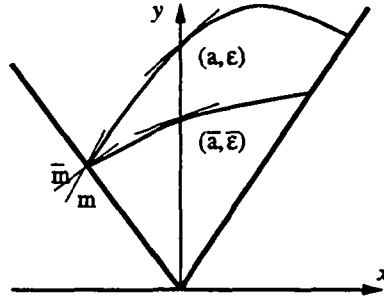


Fig. A.45. Parameterization of the trajectories for the Wedge Billiard

a trajectory parameterized by (a, ε) , we determine the slope m of the trajectory at the intersection with the boundary

$$m = a - \frac{a^2 + 1}{2(c - a)}\varepsilon + o(\varepsilon) \quad (\text{A.75})$$

using standard inversion of power series. Then we compute the slope \bar{m} of the trajectory after the elastic reflection

$$\bar{m} = \frac{2c - a - ac^2}{1 - c^2 + 2ac} + \frac{(1 + a^2)(1 + c^2)(1 + c^2 + 4d)}{2(c - a)(1 - c^2 + 2ac)^2}\varepsilon + o(\varepsilon). \quad (\text{A.76})$$

Finally we get the series for the functions $\bar{a}(a, \varepsilon)$ and $\bar{\varepsilon}(a, \varepsilon)$

$$\bar{a} = \frac{2c - a - ac^2}{1 - c^2 + 2ac} + \frac{(1 + a^2)(1 + c^2)(1 + c^2 + 2d)}{(c - a)(1 - c^2 + 2ac)^2}\varepsilon + o(\varepsilon) \quad (\text{A.77})$$

$$\bar{\varepsilon} = -\frac{c^2 + 1}{1 - c^2 + 2ac}\varepsilon + o(\varepsilon) \quad (\text{A.78})$$

which yield the same form of linearization (A.64) with this time

$$s = \frac{1 + c^2}{1 - c^2 + 2ac} \quad \text{and} \quad t = \frac{(1 + a^2)(1 + c^2)(1 + c^2 + 2d)}{(c - a)(1 - c^2 + 2ac)^2}. \quad (\text{A.79})$$

Thus the above proof applies and proposition 2 remains valid for the bouncing map of the wedge billiard.

A.2 Symmetries of the S Matrix

In this appendix, we show the consequences of invariance with respect to time inversion and reality of the potential on the structure of the scattering matrix. These relations may also be derived by combining other equations [ScS], but their origin lies in the above symmetry. They provide an easy proof of the symmetry of the full S matrix and are useful for verifying the accuracy of the numerical computations. As our computations are going to involve complex conjugation, it is convenient to introduce a new notation where open and closed modes are treated separately. We can decompose the solution of a scattering system into two sums over propagating and non-propagating mode, such as

$$\begin{aligned} \psi_n(x, y) = & \sum_{l=1}^{\Lambda} \frac{1}{\sqrt{\kappa_l}} [\delta_{nl} e^{i\kappa_l x} + S_{nl} e^{-i\kappa_l x}] \eta_l(y) \\ & + \sum_{l=\Lambda+1}^{\infty} \frac{1-i}{\sqrt{2\kappa_l}} [\delta_{nl} e^{-\kappa_l x} + S_{nl} e^{\kappa_l x}] \eta_l(y) \end{aligned} \quad (\text{A.80})$$

where $\kappa_l = \sqrt{|E - E_l|}$. We consider special wave functions Ψ which are linear combinations of the functions ψ_n with coefficients a_n

$$\Psi = \sum_{n=1}^{\infty} a_n \psi_n. \quad (\text{A.81})$$

We apply the symmetry on Ψ , or compute the conserved quantity, and look what it implies for the S matrix. Various settings of the coefficients a_n will give different relations.

A.2.1 Time Reversal Invariance

Changing the sign of time in the Schrödinger equation

$$i\hbar \frac{\partial \Psi(t)}{\partial t} = \hat{H} \Psi(t) \quad (\text{A.82})$$

and taking its complex conjugate, gives

$$i\hbar \frac{\partial \Psi^*(-t)}{\partial t} = \hat{H}^* \Psi^*(-t). \quad (\text{A.83})$$

As the potential is real and independent of t , $\Psi^*(-t)$ satisfies the same Schrödinger equation as $\Psi(t)$. Choosing a wave function Ψ as a linear combination involving no incoming closed modes, we obtain

$$\begin{aligned} \Psi = & \sum_{n=1}^{\Lambda} a_n \frac{1}{\sqrt{k_n}} e^{ik_n x} \eta_n(y) \\ & + \sum_{l=1}^{\Lambda} b_l \frac{1}{\sqrt{k_l}} e^{-ik_l x} \eta_l(y) + \sum_{l=\Lambda+1}^{\infty} b_l \frac{1-i}{\sqrt{2\kappa_l}} e^{\kappa_l x} \eta_l(y) \end{aligned} \quad (\text{A.84})$$

where

$$b_l = \sum_{n=1}^{\Lambda} a_n S_{nl}. \quad (\text{A.85})$$

In order to clarify the structure of Ψ , we will always write the expressions corresponding to incoming (resp. outgoing) modes on the first (resp. second) line of the equations. The complex conjugate of Ψ reads

$$\begin{aligned} \Psi^* &= \sum_{l=1}^{\Lambda} b_l^* \frac{1}{\sqrt{k_l}} e^{ik_l x} \eta_l(y) \\ &+ \sum_{n=1}^{\Lambda} a_n^* \frac{1}{\sqrt{k_n}} e^{-ik_n x} \eta_n(y) + \sum_{l=\Lambda+1}^{\infty} i b_l^* \frac{1-i}{\sqrt{2\kappa_l}} e^{\kappa_l x} \eta_l(y). \end{aligned} \quad (\text{A.86})$$

It is also a solution of the scattering system for which the coefficients of the outgoing modes may be related to the ingoing ones via the S matrix

$$a_n^* = \sum_{l=1}^{\Lambda} b_l^* S_{ln} \quad \text{for } n \leq \Lambda \quad (\text{A.87})$$

$$i b_l^* = \sum_{m=1}^{\Lambda} b_m^* S_{ml} \quad \text{for } l > \Lambda. \quad (\text{A.88})$$

Inserting the definition of b_l in the first relation gives

$$a_n^* = \sum_{l=1}^{\Lambda} b_l^* S_{ln} = \sum_{l=1}^{\Lambda} \left(\sum_{m=1}^{\Lambda} a_m S_{ml} \right)^* S_{ln} = \sum_{m=1}^{\Lambda} a_m^* \left(\sum_{l=1}^{\Lambda} S_{ml}^* S_{ln} \right) \quad (\text{A.89})$$

for any choice of the coefficient a_n^* . Hence we obtain

$$\sum_{l=1}^{\Lambda} S_{ml}^* S_{ln} = \delta_{mn} \quad \text{for } n, m \leq \Lambda. \quad (\text{A.90})$$

Using the same idea, the second relation leads to

$$i b_l^* = \sum_{n=1}^{\Lambda} i a_n^* S_{nl}^* = \sum_{m,n=1}^{\Lambda} (a_n S_{nm})^* S_{ml} = \sum_{n=1}^{\Lambda} a_n^* \left(\sum_{m=1}^{\Lambda} S_{nm}^* S_{ml} \right). \quad (\text{A.91})$$

Thus we get

$$i S_{nl}^* = \sum_{m=1}^{\Lambda} S_{nm}^* S_{ml} \quad \text{with } n \leq \Lambda \text{ and } l > \Lambda. \quad (\text{A.92})$$

Another choice of the coefficient a_n with no incoming open modes would give a wave function

$$\begin{aligned} \Psi &= \sum_{n=\Lambda+1}^{\infty} a_n \frac{1-i}{\sqrt{2\kappa_n}} e^{-\kappa_n x} \eta_n(y) \\ &+ \sum_{l=1}^{\Lambda} b_l \frac{1}{\sqrt{k_l}} e^{-ik_l x} \eta_l(y) + \sum_{l=\Lambda+1}^{\infty} b_l \frac{1-i}{\sqrt{2\kappa_l}} e^{\kappa_l x} \eta_l(y) \end{aligned} \quad (\text{A.93})$$

with this time $b_l = \sum_{n=\Lambda+1}^{\infty} a_n S_{nl}$. Its complex conjugate reads

$$\begin{aligned} \Psi^* &= \sum_{l=1}^{\Lambda} b_l^* \frac{1}{\sqrt{k_l}} e^{ik_l x} \eta_l(y) + \sum_{n=\Lambda+1}^{\infty} ia_n^* \frac{1-i}{\sqrt{2\kappa_n}} e^{-\kappa_n x} \eta_n(y) \\ &\quad + \sum_{l=\Lambda+1}^{\infty} ib_l^* \frac{1-i}{\sqrt{2\kappa_l}} e^{\kappa_l x} \eta_l(y) \end{aligned} \quad (\text{A.94})$$

and hence

$$ib_l^* = \sum_{m=1}^{\Lambda} b_m^* S_{ml} + \sum_{m=\Lambda+1}^{\infty} ia_m^* S_{ml} \quad \text{with } l > \Lambda. \quad (\text{A.95})$$

Inserting the new definition of b_l , we get

$$ib_l^* = \sum_{n=\Lambda+1}^{\infty} ia_n^* S_{nl} = \sum_{n=\Lambda+1}^{\infty} a_n^* \left(\sum_{m=1}^{\Lambda} S_{nm}^* S_{ml} \right) + \sum_{n=\Lambda+1}^{\infty} ia_n^* S_{nl} \quad (\text{A.96})$$

for any choice of the a_n^* . Thus we obtain

$$\sum_{m=1}^{\Lambda} S_{nm}^* S_{ml} = i(S_{nl}^* - S_{nl}) = 2\text{Im}[S_{nl}] \quad \text{with } n, l > \Lambda. \quad (\text{A.97})$$

A.2.2 Conservation of flux

The divergence of the current vanishes for stationary states of the Schrödinger equation with real potential. Thus the flux $F(x)$ through the surface delimited by the right (left) part of the system and the section Γ at $x = \text{const}$ must also vanish. The only part which contributes is the section Γ , so that

$$F(x) = \frac{1}{2i} \int_{-\infty}^{\infty} dy (\psi^* \nabla_x \psi - \psi \nabla_x \psi^*). \quad (\text{A.98})$$

Computation of the flux for the wave function (A.84) gives

$$F(x) = \sum_{n=1}^{\Lambda} a_n^* a_n - \sum_{l=1}^{\Lambda} b_l^* b_l = 0 \quad (\text{A.99})$$

where we have used the orthogonality of the $\eta_n(y)$. Replacing b_l with the corresponding definition, we get

$$\sum_{n=1}^{\Lambda} a_n^* a_n = \sum_{l=1}^{\Lambda} b_l^* b_l = \sum_{n,m=1}^{\Lambda} a_m^* \left(\sum_{l=1}^{\Lambda} S_{ml}^* S_{nl} \right) a_n \quad (\text{A.100})$$

for any choice of a_n and a_n^* . Thus we obtain

$$\sum_{l=1}^{\Lambda} S_{ml}^* S_{nl} = \sum_{l=1}^{\Lambda} S_{nl} S_{lm}^{\dagger} = \delta_{nm} \quad \text{with } n, m \leq \Lambda. \quad (\text{A.101})$$

Considering now the wave function (A.93), we get

$$F(x) = -\sum_{l=1}^{\Lambda} b_l^* b_l + i \sum_{n=\Lambda+1}^{\infty} (b_n^* a_n - a_n^* b_n) = 0. \quad (\text{A.102})$$

This leads to

$$\sum_{n,m=\Lambda+1}^{\infty} a_n^* a_m \left(\sum_{l=1}^{\Lambda} S_{nl}^* S_{ml} \right) = i \sum_{n,m=\Lambda+1}^{\infty} (a_m^* S_{mn}^* a_n - a_n^* a_m S_{mn}) \quad (\text{A.103})$$

where the sums can be rearranged to give

$$\sum_{n,m=\Lambda+1}^{\infty} a_n^* a_m \left(-\sum_{l=1}^{\Lambda} S_{nl}^* S_{ml} + i(S_{nm}^* - S_{mn}) \right) = 0 \quad (\text{A.104})$$

for any choice of a_n and a_n^* . Thus we get

$$\sum_{l=1}^{\Lambda} S_{nl}^* S_{ml} = \sum_{l=1}^{\Lambda} S_{ml} S_{ln}^\dagger = i(S_{nm}^* - S_{mn}) \quad \text{with } n, m > \Lambda. \quad (\text{A.105})$$

Finally, taking a wave function with both open and closed incoming channels, we obtain

$$F(x) = \sum_{n=1}^{\Lambda} a_n^* a_n - \sum_{l=1}^{\Lambda} b_l^* b_l + i \sum_{n=\Lambda+1}^{\infty} (b_n^* a_n - a_n^* b_n) = 0 \quad (\text{A.106})$$

where this time $b_l = \sum_{n=1}^{\infty} a_n S_{nl}$. Subtracting all the terms appearing in the previous relations and rearranging the sums, this gives

$$\begin{aligned} & \sum_{m=1}^{\Lambda} \sum_{n=\Lambda+1}^{\infty} i [a_m^* S_{mn}^* a_n - a_n^* S_{mn} a_m] = \\ & \sum_{m=1}^{\Lambda} \sum_{n=\Lambda+1}^{\infty} \left[a_n^* a_m \left(\sum_{l=1}^{\Lambda} S_{nl}^* S_{ml} \right) + a_m^* a_n \left(\sum_{l=1}^{\Lambda} S_{ml}^* S_{nl} \right) \right] \end{aligned} \quad (\text{A.107})$$

for any choice of a_n and a_n^* . Thus

$$\left. \begin{aligned} \sum_{l=1}^{\Lambda} S_{nl}^* S_{ml} &= \sum_{l=1}^{\Lambda} S_{ml} S_{ln}^\dagger = -i S_{mn} \\ \sum_{l=1}^{\Lambda} S_{ml}^* S_{nl} &= \sum_{l=1}^{\Lambda} S_{nl} S_{lm}^\dagger = i S_{mn}^* = i S_{nm}^\dagger \end{aligned} \right\} \text{with } m \leq \Lambda \text{ and } n > \Lambda \quad (\text{A.108})$$

which are equivalent.

A.2.3 Summary and Reformulation

To improve the formulation of the results, we will use the notation

$$S = \begin{pmatrix} S_{oo} & S_{oc} \\ S_{co} & S_{cc} \end{pmatrix} \quad (\text{A.109})$$

where the indexes o and c of the submatrices stand respectively for *open* and *closed* channels. This notation has to be taken with some care, since $(S^T)_{oc} = (S_{co})^T$.

Equations (A.90),(A.92) and (A.97), related with time invariance, can be rewritten in matrix form as

$$S_{oo} \cdot S_{oo}^* = S_{oo}^* \cdot S_{oo} = \mathbb{1} \quad (\text{A.110})$$

$$S_{oo} \cdot S_{oc}^* = -iS_{oc} \quad (\text{A.111})$$

$$S_{co} \cdot S_{oc}^* = i(S_{cc}^* - S_{cc}) = 2\text{Im}[S_{cc}] \quad (\text{A.112})$$

and similarly, equations (A.101),(A.108) and (A.105), related with conservation of flux, are rewritten

$$S_{oo} \cdot S_{oo}^\dagger = S_{oo}^\dagger \cdot S_{oo} = \mathbb{1} \quad (\text{A.113})$$

$$S_{oo} \cdot S_{oc}^\dagger = -iS_{oc} \quad (\text{A.114})$$

$$S_{co} \cdot S_{oc}^\dagger = i(S_{cc}^\dagger - S_{cc}). \quad (\text{A.115})$$

Comparing pairwise both sets of equations, we get

$$S = S^T. \quad (\text{A.116})$$

Thus the symmetry of the total S matrix is a consequence of the fact that the potential is time independent and real.

References

- [Ar] Arnold V I 1978 *Mathematical Methods of Classical Mechanics* (New York: Springer)
- [AS] Abramowitz M and Stegun I A 1964 *Handbook of mathematical functions* (New York: Dover)
- [BDJS] Blümel R, Dietz B, Jung C and Smilansky U 1992 On the Transition to Chaotic Scattering *J. Phys. A* **25** 1483
- [Be] Berry M V 1985 Semiclassical Theory of Spectral Rigidity *Proc. R. Soc. Lond. A* **400** 229
- [BG] Bohigas O and Giannoni J M 1984 Chaotic Motion and Random Matrix Theories *Lecture Notes in Physics* **209** 1
- [BGS] Bohigas O, Giannoni J M and Schmit C 1984 Characterization of Chaotic Quantum Spectra and Universality of Level Fluctuation Laws *Phys. Rev. Lett.* **52** 1
- [BH] Beenakker C W J and van Houtten H 1991 in *Solid States Physics: Advances in Research and Applications* **44** edited by Ehrenreich H and Turnbull D (New York: Academic)
- [Bog] Bogomonly E B 1992 Semiclassical Quantization of Multidimensional Systems *Nonlinearity* **5** 805
- [Boh] Bohigas O 1989 Random Matrices and Chaotic Dynamics *Chaos and Quantum Physics* edited by Giannoni M J (Amsterdam: North Holland)
- [Br] Brahic A 1971 Numerical Study of a Simple Dynamical System. I *Astron. and Astrophys.* **12** 98
- [BS] Blümel R and Smilansky U 1990 Random-Matrix Description of Chaotic Scattering: semiclassical approach *Phys. Rev. Lett.* **64** 241
- [BT1] Berry M V and Tabor M 1976 Closed Orbits and the Regular Bound Spectrum *Proc. R. Soc. Lond. A* **349** 101
- [BT2] Berry M V and Tabor M 1977 Level Clustering in the Regular Spectrum *Proc. R. Soc. Lond. A* **356** 375
- [Bu] Bunimovitch L A 1985 Decay of Correlations in Dynamical Systems with Chaotic Behavior *Sov. Phys. JETP* **62** 842
- [Cha] Chaplygin S A 1933 On a Paraboloid Pendulum *Izd. Akad. Nauk SSSR* **1** 194 (in Russian, quoted in [KT])
- [CFS] Cornfeld I P, Fomin S V and Sinai Ya G 1978 *Ergodic Theory* (New York: Springer)

- [CRL] Creagh S C, Robbins J M and Littlejohn R G 1990 Geometrical Properties of Maslov Indices in the Semiclassical Trace Formula for the Density of States *Phys. Rev. A* **42** 1907
- [DR] Dagaëff T and Rouvinez C 1993 On the Discontinuities of the Boundary in Billiards *Physica D* **67** 166.
- [DS1] Dietz B and Smilansky U 1993 A Scattering Approach to the Quantization of Billiards - the Inside/Outside Duality *Chaos* **3** 581
- [DS2] Dietz B and Smilansky U 1993 Scattering From a Square Obstacle *Preprint* Weizmann Institute
- [DoS] Doron E and Smilansky U 1992 Semiclassical Quantization of Chaotic Billiards: a Scattering Approach *Nonlinearity* **5** 1055
- [Du] Dullin H R private communication
- [Ei] Einstein A 1917 Zum Quantensatz von Sommerfeld und Epstein *Verhandl. Deutsch. Phys. Ges.* **19** 82
- [EP1] Eckmann J P and Pillet C A 1994 Spectral Duality for Planar Billiard *Preprint* University of Geneva
- [EP2] Eckmann J P and Pillet C A 1994 Scattering Phases and Density of States for Exterior Domains *Preprint* University of Geneva
- [ER] Eckmann J P and Ruelle D 1985 Ergodic theory of chaos and strange attractors *Rev. Mod. Phys.* **57** 617
- [Fe] Feynman R P 1948 Space-Time Approach to non-Relativistic Quantum Mechanics *Rev. Mod. Phys.* **20** 367
- [FH] Feynman R P and Hibbs A R 1965 *Quantum Mechanics and Path Integrals* (New York: McGraw Hill).
- [GRMN] Gaspard P, Rice S A, Mikesa H J and Nakamura K 1990 Parametric Motion of Energy Levels: Curvature Distribution *Phys. Rev. A* **42** 4015
- [Gu1] Gutzwiller M C 1967 Phase Integral Approximation in Momentum Space and the Bound State of an Atom *J. Math. Phys.* **8** 1979.
- [Gu2] Gutzwiller M C 1990 *Chaos in Classical and Quantum Mechanics* (New York: Springer)
- [Gu3] Gutzwiller M C 1993 Poincaré Surface of Section and Quantum Mechanics *Chaos* **3** 591
- [GW] Goldberger M L and Watson K M 1964 *Collision Theory* (New York: Wiley)
- [HW] Hénon M and Wisdom J 1983 The Benettin-Strelcyn Oval Billiard Revisited *Physica D* **8** 157
- [Ju] Jung C 1986 Poincaré Map for Scattering States *J. Phys. A* **19** 1345
- [KL] Korsh H J and Lang J 1991 A new Integrable Gravitational Billiard *J. Phys. A* **24** 45
- [Ko] Kosloff R 1988 Time-Dependent Quantum-Mechanical Methods for Molecular Dynamics *J. Phys. Chem.* **92** 2087
- [KT] Kozlov V V and Treshchëv D V 1991 *Translation of Mathematical Monographs: Billiards* Vol 89 (Rhode Island: American Mathematical Society)
- [LL1] Landau L D and Lifshitz E M 1958 *Mechanics* (London: Pergamon)

- [LL2] Landau L D and Lifshitz E M 1958 *Quantum mechanics : non-relativistic theory* (London: Pergamon)
- [LM] Lehtihet H E and Miller B N 1986 Numerical Study of a Billiard in a Gravitational Field *Physica D* **21** 93
- [Mi] Miller W H 1974 Classical-Limit Quantum Mechanics and the Theory of Molecular Collisions *Adv. Chem. Phys.* **25** 69
- [Mil] Milnor J 1985 On the Concept of Attractor *Commun. Math. Phys.* **99** 177
- [MR] Miller B N and Ravishankar K 1988 Stochastic Modeling of a Billiard in a Gravitational Field: Power Law Behaviour of Lyapunov Exponents *J. Stat. Phys.* **53** 1299
- [Op] von Oppen F 1994 Exact Distribution of Eigenvalue Curvature of Chaotic Quantum Systems *Phys. Rev. Lett.* **73** 798
- [Os] Oseledec V I 1968 A Multiplicative Ergodic Theorem. Lyapunov Characteristic Numbers for Dynamical Systems *Trudy Moscov. Mat. Obsc* **19** 179 [*Trans. Moscow Math. Soc.* **19** 197]
- [PC] Parker T S and Chua L O 1989 *Practical Numerical Algorithms for Chaotic Systems* (New York: Springer)
- [Pr] Prosen T 1994 Exact Quantum Surface of Section Method *J. Phys. A* **27** L709
- [RB] Richens P J and Berry M V 1981 Pseudointegrable Systems in Classical and Quantum Mechanics *Physica D* **2** 495.
- [Ro] Robnik M 1994 Chaos and Energy Level Statistics *J. Phys. Soc. Jpn.* **63** 131
- [RS] Rouvinez C and Smilansky U 1995 A Scattering Approach to the Quantization of Hamiltonians in 2 Dimensions - Application to the Wedge Billiard *J. Phys. A* **28** 77
- [RSW] Richter P H, Scholz H J and Wittek A 1990 A Breathing Chaos *Nonlinearity* **3** 45
- [ScS] Schanz H and Smilansky U 1993 Quantization of Sinai's Billiard - a Scattering Approach *Preprint* Weizmann Institute
- [SG1] Szeredi T and Goodings D A 1992 Periodic Orbits from the Quantum Energy Spectrum of the Wedge Billiard *Phys. Rev. Lett.* **69** 1640
- [SG2] Szeredi T and Goodings D A 1993 Classical and Quantum Chaos in the Wedge Billiard: Classical Mechanics *Phys. Rev. E* **48** 3518
- [SG3] Szeredi T and Goodings D A 1993 Classical and Quantum Chaos in the Wedge Billiard: Quantum Mechanics and Quantization Rules *Phys. Rev. E* **48** 3529
- [Si] Sinai Ya G 1970 Dynamical Systems with Elastic Reflections *Russ. Math. Surv.* **25** No 2 137
- [SS] Sieber M and Steiner F 1990 Generalized Periodic Orbit Sum Rules for Strongly Chaotic Systems *Phys. Lett. A* **144** 159
- [SLG] Szeredi T, Lefebvre J H and Goodings D A 1993 Application of Bogomonly Transfer Operator to Semiclassical Quantization of Chaotic Systems *Phys. Rev. Lett.* **71** 2891
- [Sm] Smilansky U 1992 Semiclassical Quantization of Chaotic Billiards *Chaos and Quantum Chaos* ed W. Dieter Heiss (Berlin: Springer)

- [SSCL] Sieber M, Smilansky U, Creagh S C and Littlejohn R G 1993 Non-Generic Spectral Statistics in the Quantized Stadium Billiard *J. Phys. A* **26** 6217
- [St] Strelcyn J M 1986 Plane Billiards as Smooth Dynamical Systems with Singularities *Lectures Notes in Math.* 1222
- [TaH] Takami T and Hasegawa H 1992 Curvature Distribution of Chaotic Quantum Systems: Universality and Nonuniversality *Phys. Rev. Lett.* **68** 419
- [ToH] Tomsovic S and Heller E 1993 Long-time Semiclassical Dynamics of Chaos: The Stadium Billiard *Phys. Rev. E* **47** 282
- [VCG] Vivaldi F, Casati G and Guarneri I 1983 Origin of the Long Time Tails in Strongly Chaotic Systems *Phys. Rev. Lett.* **51** 727
- [WGC] Whelan N D, Goodings D A and Cannizzo J K 1990 Two Balls in One Dimension with Gravity *Phys. Rev. A* **42** 742
- [Wi] Wittek A 1991 Die Quantenmechanik eines nichtintegrierbaren Systems *Ph.D. Thesis* Universität Bremen
- [Wo] Wojtkowski M P 1990 A System of one Dimensional Balls with Gravity *Commun. Math. Phys.* **126** 507
- [WM] Wright H L and Miller B N 1984 Gravity in One Dimension: a Dynamical and Statistical Study *Phys. Rev. A* **93** 1411
- [ZK] Zemlyakov A N and Katok A B 1975 Topological Transitivity of Billiards in Polygons *Matematicheskije Zametki* **18** No 2 291
- [ZD] Zakrzewski J and Delande D 1993 Parametric Motion of Energy Levels in Quantum Chaotic Systems. I. Curvature Distributions *Phys. Rev. E* **47** 1650

Curriculum Vitae

General information

Last Name: Rouvinez
First Name: Christophe
Date of birth: June 8, 1965
Citizenship: Swiss
Origin: Vissoie and Grimentz, Switzerland
Mother tongue: French
Office Adress: Institut de Physique Theorique, PHB Ecublens, CH-1015 Lausanne

Education

1980-1985: Lycée-Collège des Creusets in Sion, Maturity Certificate type C (sciences) in 1985.
1985-1990: Swiss Federal Institute of Technology in Zurich, Physics Department, Diploma thesis on Gauge Invariant Normal Ordering in 1990 under supervision of Prof. C. Schmid.
1990-1995: Swiss Federal Institute of Technology in Lausanne, Theoretical Physics Institute, Preparation of Ph. D. thesis on Hamiltonian Chaos under supervision of Prof. Ph. Choquard.

Publications

1993 Dagaëff T and Rouvinez C 1993 On the Discontinuities of the Boundary in Billiards *Physica D* **67** 166
1995 Rouvinez C and Smilansky U 1995 A Scattering Approach to the Quantization of Hamiltonians in 2 Dimensions - Application to the Wedge Billiard *J. Phys. A* **28** 77

Presentations

1992 Rencontre de Physique Statistique de Paris, Paris, January 1992, Communication: Influence of Singularities in Billiards, T. Dagaëff and C. Rouvinez.

- 1993 Integrability and Chaotic Behaviour, Torun, July 1993, Poster: On the Discontinuities of the Boundary in Billiards, T. Dagaëff and C. Rouvinez.
- 1994 Symposium on Classical and Quantum Billiards, Ascona, July 1994, Poster: A Scattering Approach to the Wedge Billiard, C. Rouvinez and U. Smilansky.
Third International Conference on Computational Physics, Copenhagen, August 1994, Poster: A Scattering Approach to the Wedge Billiard, C. Rouvinez and U. Smilansky.